UNIVERSITY OF CALIFORNIA, SAN DIEGO

Development of sensors and techniques to assess earthquake hazards and submarine slope stability

A dissertation submitted in partial satisfaction of the
requirements for the degree
Doctor of Philosophy

in

Earth Sciences

by

John Blum

Committee in charge:

Mark Zumberge, Chair
Dave Chadwell
Neal Driscoll
Myrl Hendershott
Michael Sailor
Brad Werner

2010

The dissertation of John Blum is approved, and it is acceptable in quality and form for publication on microfilm and electronically:

_____

_____

_____

_____

_____

_____
Chair

University of California, San Diego

2010

DEDICATION

To those who listen to the natural world not as a metaphor, but for how it really is.

EPIGRAPH

"The surface of the Earth is the shore of the cosmic ocean. From it we have learned most of what we know. Recently, we have waded a little out to sea, enough to dampen our toes or, at most, wet our ankles. The water seems inviting. The ocean calls"

—*Carl Sagan*

"The love of wilderness is more than a hunger for what is always beyond reach; it is also an expression of loyalty to the earth ... the only home we shall ever know, the only paradise we ever need – if only we had the eyes to see."

—*Edward Abbey*

TABLE OF CONTENTS

LIST OF FIGURES

LIST OF TABLES

ACKNOWLEDGEMENTS

Completion of this dissertation would not have been possible without the support of numerous individuals who mentored me and advocated for its success. Foremost is my chief adviser, Mark Zumberge, whose professional guidance and tutelage has imbued in me a breadth and depth of skills, experience, and opportunity. David Chadwell also deserves recognition for his role in mentoring me and this project, along with Neal Driscoll and other members of my committee.

Much of this dissertation is owed to mentors not at Scripps Institution of Oceanography, in particular Joe Dellinger at BP, who advocated for me behind the scenes to receive proprietary industrial data for research purposes. He also served as an excellent teacher and adviser on numerous geophysical issues. Also at BP, I would like to thank Herlinde Mannaerrts-Drew, Hugh Banon, Eric Litdke, and Philippe JeanJean, who managed portions of the optical fiber seafloor strainmeter project and supplied funds for my research in the Gulf of Mexico. Without their leadership and advocacy, none of this work would have been completed.

The biggest accolades go to those behind the scenes – my family and friends – for they are the ones that provide the most ardent memories, the nostalgia, and sometimes, even the regret. I would like to thank my parents, James and Ruth Blum, for their love, devotion, and support, as well as my brother and sister, Vince and Amy. Traveling to this place took me through three different universities, and I owe them more than gratitude. From Butler: Mark and Sarah Wuellner, and Brian and Kate Roberts, for providing a longstanding friendship. From Michigan: Ryan Foley, Jimmy Degs, Soo Heyong-Lee, and Geoff, thanks for making my transition memorable and meaningful. In California: Prasad, Fred, and Steph, thanks. To Danny, Brendan, Andy, Ann, and the IGPP Men's Club, thanks for not condoning cetacean abuse. To Vi Ngo, for showing me the meaning of friendship, love, and your unending support, and to everyone else in San Diego who made this America's finest city.

Portions of this dissertation are published, being considered for publication, or are intended to be submitted for publication in various journals.

Chapter 2 Most of Chapter 2 has been previously published in: Blum, J., Nooner, S., and Zumberge, M., 2008: Recording Earth strain with optical fibers. *IEEE Sensors Journal*, **8**(7), 1152-1160.

Chapter 3 Material from Chapter 3 has been previously published in: Blum, J., Nooner, S., and Zumberge, M., 2008: Recording Earth strain with optical fibers. *IEEE Sensors Journal*, **8**(7), 1152-1160.

Chapter 4 Most of Chapter 4 has been accepted for publication in: Blum, J., Igel, H., and Zumberge, M., 2010: Observations of Rayleigh wave phase velocity and coseismic deformation using an optical fiber, interferometric vertical strainmeter at the SAFOD borehole, California. *Bulletin of the Seismological Society of America*, **100**(5A), In Press.

Chapter 5 Material from the first portion of Chapter 5 (through section 5.4) has been accepted for publication in: Blum, J.A., Chadwell, C., Driscoll, N., and Zumberge, M., 2010: Assessing slope stability in the Santa Barbara Basin using seafloor geodesy and CHIRP seismic data. *Geophysical Research Letters*, In Press.

Chapter 6 We are currently preparing Chapter 6 for publication as: Blum, J., 2010: The M_s 5.3 Green Canyon (northern Gulf of Mexico) earthquake of 10 February 2010: a landslide or fault source? *Geophysics Journal International*, In Preparation.

VITA

2003	B.S. in Honors Physics *with honors*, University of Michigan, Ann Arbor
2010	Ph.D. in Earth Sciences, University of California, San Diego

PUBLICATIONS

Blum, J., Igel, H., and Zumberge, M., 2010: Observations of Rayleigh wave phase velocity and coseismic deformation using an optical fiber, interferometric vertical strainmeter at the SAFOD borehole, California. *Bulletin of the Seismological Society of America*, **100**(5A), In Press.

Blum, J., Chadwell, C., Driscoll, N., and Zumberge, M., 2010: Assessing slope stability in the Santa Barbara Basin using seafloor geodesy and CHIRP seismic data. *Geophysical Research Letters*, In Press.

Blum, J., and Dellinger, J., 2010: The M_s 5.3 Green Canyon (northern Gulf of Mexico) earthquake of 10 February 2010: a landslide or fault source? *Geophysics Journal International*, In Preparation.

Dellinger, J.,**Blum, J.**, and Nettles, M., 2009: The 10 February 2006 "Green Canyon" earthquake: a case history of an unusual seismic event. *SEG Expanded Abstracts*, **28**, 572, DOI:10.1190/1.3255822.

Blum, J., Nooner, S., and Zumberge, M.A., 2008: Recording earth strain with optical fibers. *IEEE Sensors Journal*, **8**, 1152-1160.

Zumberge, M., Bacock, J., Banon, H.H., **Blum, J**., Chadwell, C.D., Dingler, J., Driscoll, N., DSpain, G., Jeanjean, P., Kent, G., Openshaw, G., and Orcutt, J., 2006: Studies of the Gaviota Slide Offshore Southern California. In *Geohazards*, Farrokh Nadim, Rudolf Pttler, Herbert Einstein, Herbert Klapperich, and Steven Kramer Eds, ECI Symposium Series, Volume P07, `http://services.bepress.com/eci/geohazards/26.`

Bokuniewicz, H., Pollock, M., **Blum, J.**, and Wilson, R. 2005: Submarine groundwater discharge and salt penetration across the sea floor. *Groundwater*, **42**, 983-989.

Blum, J., and Shen, Y, 2004: Thermal, hydrous, and mechanical states of the mantle transition zone beneath southern Africa. *Earth and Planet. Sci. Lett.*, **217**, 367-378.

Shen, Y., and **Blum, J.**, 2003: Seismic evidence for accumulated oceanic crust above the 660-km discontinuity beneath southern Africa. *Geophys. Res. Lett.*, **30**(18),1925.

ABSTRACT OF THE DISSERTATION

Development of sensors and techniques to assess earthquake hazards and submarine slope stability

by

John Blum
Doctor of Philosophy in Earth Sciences
University of California San Diego, 2010
Mark Zumberge, Chair

Reducing vulnerability from geohazards such as submarine landslides and earthquakes requires identifying susceptible regions and modeling the consequences. We introduce innovative instruments and techniques that have the potential to advance preparedness and mitigation efforts.

We develop optical fiber strainmeters to monitor deformation along unstable slopes and in a vertical borehole at the SAFOD observatory. With this latter strainmeter, we record coseismic strain-steps from local microearthquakes in addition to teleseismic events, which we compare to accelerations from a nearby seismometer to derive local phase velocities.

We also study a seafloor crack within the Santa Barbara Basin that might be the beginning of an imminent submarine landslide. We deployed a new seafloor acoustic ranging system which detected no motion across the crack above a 99% confidence level of $\pm$ 7 mm/yr over two years of monitoring. Combined with sub-bottom CHIRP profiles with $<$ 1 m accuracy exhibiting no evidence of internal deformation, we conclude that the elongated scarp-like crack is most likely a relict feature from a previous failure. Probabilistic seismic hazard analysis suggests that an $\approx M \geq 7$ earthquake is required within the basin to explain a previous landslide, arguing against a recent relocation of the 21 Dec. 1812 earthquake (M7.1) to the San Andreas Fault.

Finally, we study the anomalous M_s 5.3 earthquake of 10 Feb. 2006 in the Gulf of Mexico. Surface wave full-waveform inversion suggested a source of either a shallow landslide translating on a near sub-horizontal surface, or sub-horizontal or vertical faulting within shallow, low velocity sediments. We integrated the results of two industrial seismic exploration surveys to relocate the epicenter. The geology around the relocation is consistent with the sliding source model, and geotechnical modeling suggests that the sharp relief is capable of producing a large landslide. To test the landslide hypothesis, we surveyed the region acquiring multibeam, sidescan, and sub- bottom seismic profiles. The results of that survey indicate no evidence of a large debris flow. This suggests a source mechanism within the shallow sedimentary section on either a near sub- horizontal or near vertical plane.

Chapter 1

Introduction

1.1 Significance of natural hazards

Each year in the United States, natural disasters such as earthquakes, landslides, tsunamis, floods, hurricanes, volcanoes, and wildfires cause hundreds of deaths and billions of dollars of damage, from disruption of commerce and destruction of infrastructure to disaster aid (USGS, 2007). Worldwide, those numbers can reach hundreds of thousands of lives to trillions of dollars. From 1947-1980, 450,048 people lost their lives from earthquakes, 4,519 from tsunami, and 10,841 from landslides (Abbott, 2006): an average of 14,103 fatalities per year from those events. If we additionally account for volcanoes, floods, hurricanes, tornados, and other severe weather events such as drought, the average number of annual fatalities is 37,107.

Exposure to natural hazards may be increasing due to a growing population and infrastructure. Compare those roughly 37,000 annual deaths from 1947-1980 to an estimated 58,000 annual deaths from 1994-2003 (Guha-Sapir et al., 2004). More than 200,000 people lost their lives in the tragic 26 December, 2004 tsunami (Gisler, 2008). The 2010 Haiti earthquake potentially resulted in 230,000 deaths (BBC News, 2010). While those events themselves may be anomalous in their geophysical character, it is the ability to mitigate the damages that is under increased threat. The annual economic costs of these geologic hazards ranged from US$28-230 billion from 1994-2003, with a per year average of US$67 billion; these cost have increased

14-fold since the 1950s (Guha-Sapir et al., 2004) and the consequences are expected to continue with increased population growth and urbanization, particularly in the developing world.

Carefully constructed policies and planning may significantly lessen the impacts of these events. Geoscience plays a critical role in identifying and assessing these threats. By developing new sensors and studying the geomorphology and subsurface structure of potential hazards, we can constrain the parameters responsible for their failure, their prevalence, and their physical impact. Such understanding is critical in planning for future events and implementing policies to mitigate their impacts.

Similarly, natural resource extraction such as oil, gas, and minerals, as well as geothermal heat mining, require greater knowledge of the subsurface as well as greater monitoring of potential consequences such as oil spills, subsidence, and other forms of pollution and damages. Innovative instrumentation and modeling are two ways to more safely identify, extract, and limit the consequences of their production.

The focus of this dissertation is on developing technologies and techniques to assess and abate geohazards and to facilitate resource extraction more safely. In particular, this dissertation focuses on two areas: (1) developing optical fiber strain sensors to measure deformation on potentially unstable submarine slopes and in boreholes; and (2) assessing submarine landslide and earthquake hazards offshore Santa Barbara, California and in the Gulf of Mexico.

1.2 Submarine Slope Stability

Submarine landslides occur along many continental margins. In addition to their hazard potential for seafloor infrastructure and populated coastlines, they are also one of the main mechanisms of organic sediment and carbon transfer from the inner shelf – where sediments derived from rivers and beach erosion reign – to the outer shelf and deep ocean basins. A submarine mass movement (or mass wasting) can occur in a variety of forms, such as a rotational slump, translational

slide, debris flow, turbidity current, or other term, but for the purposes of this dissertation, we generally define a submarine landslide as the movement of a semi-coherent mass of sediment down a slope. The causes of landslides vary, including: over-steepening of slopes due to sediment deposition; overpressure due to rapid sediment deposition; earthquake shaking; changes in pore pressure within a weaker structural or stratigraphic layer; and possibly gas hydrate disassociation, among other causes. These causes may coexist, ore the existence of one may heighten the potential for failure, such as an over-steepened slope failing during an earthquake: the sum of the downslope gravitational stress and seismic ground shaking exceeding the resistive strength of the sediment.

On land, the capacity to predict, or at least delineate, future and near imminent landslides exists. We can monitor volcanic tremors, rain fall, water levels, as well as use seismometers and GPS to detect movements. In contrast, the prediction of landslides offshore is problematic. This dissertation presents technologies and techniques to assess and abate possible submarine events. We identify areas where landslides might be imminent, model the consequences, and monitor critical areas. These techniques are important so that appropriate mitigation strategies can be developed.

In Chapter 2, we introduce the concept of an optical fiber seafloor strainmeter that uses an electronic distance meter (EDM) to interrogate the length of an optical fiber on the seafloor. This technology was conceptualized and constructed to monitor areas where slope failure might be imminent. Chapter 3 contains the details of this sensor's development and our attempts to deploy it in the Santa Barbara Basin, an area with a potentially unstable slope (see Chapter 5.)

Chapter 5 deals with the Santa Barbara Basin in detail, where acoustic ranging instruments and seismic sub-bottom profiles to monitor deformation across a suspected future landslide were successfully deployed. In this chapter we also exploit probabilistic seismic hazard analysis to identify historical earthquakes thought to be responsible for landslides in the region.

In Chapter 6, we shift attention to the Gulf of Mexico, where several unusual seismic events (atypical in size, frequency, and source) occurred in 2006. At least

one of these events was thought to be the result of a large submarine landslide. In this chapter, we model and discuss the causes and consequences of such an event and present the results from a geophysical survey seeking to test for the existence of a large landslide.

1.3 Borehole Instruments

Submarine landslides are a prominent arc of this dissertation, however, they are not the only geohazard we study. Earthquakes are often the most deadly and difficult of disasters for which we can prepare due to the difficulty in forecasting and warning populations. One technique used to study earthquakes and the tectonic forces which drive them is through borehole strainmeters.

A borehole is a hole drilled into the ground. Examples would include oil and gas wells, which are often instrumented in order to make observations about the Earth within or around the hole. As an outgrowth of extensive optical fiber work, we developed a vertical strainmeter that relies on interferometry to monitor changes in length of a fiber encased within deep boreholes.

Engineering details are discussed in Chapter 2. We are capable of treating the strainmeter similar to a conventional seismometer, and we observe both large teleseismic earthquakes from across the globe as well as small microearthquakes from nearby faulting. The information about the Earth that we extract from these events is discussed in Chapter 4. This information, including the rock velocity and possibly orientation of faulting, has the potential to be advanced for hazard analysis.

One of the drivers of this technology is oil, gas, and geothermal fields, which often are in areas with higher temperatures which affect downhole electronics. Hydrofracturing of rock, or fraccing, is becoming increasingly common to extract oil and gas from impermeable shales as well as to increase the surface area for water contact with hot rock in geothermal applications. Fracture models are typically created based on incomplete knowledge of the subsurface, but if those models are incorrect, our ability to extract these resources is diminished and we also enhance

the possibility of contaminating potable water supplies. Our sensor is significant in that it has the potential to operate in these extreme environments better than electronic instruments, and it can detect small amounts of ground deformation that can potentially be used to recover the actual fracture networks.

1.4 Conclusions

Managing geohazard risks is essential to identifying new opportunities or adaptation strategies for public policy, health, and business. Sustaining our long term growth as a society requires transferring the latest scientific knowledge and tools to stakeholders. This dissertation contains not only new knowledge, but also outlines new tools that can be used in academic, government, and industry to understand our risks and develop resilient communities in a hazardous world.

REFERENCES

Abbott, P. L., 2006: *Natural Disasters*. McGraw-Hill, New York, 5 edition.

BBC News, 2010: Haiti quake death toll rises to 230,000. *http://news.bbc.co.uk/2/hi/americas/8507531.stm*.

Gisler, G., 2008: Tsunami simulations. *Annu. Rev. Fluid. Mech.*, **40**, 71–90.

Guha-Sapir, D., Hargiitt, D., and Hoyois, P., 2004: *Thirty years of natural disasters 1974-2003: the numbers*. Presses universitaires de Louvain, Belgium.

The New York Times, 2010: Obama to open offshore areas to oil drilling for first time. *http://www.nytimes.com/2010/03/31/science/earth/31energy.html*.

USGS, 2007: Natural hazards – a national threat. *U.S. Geological Survey*, **Fact Sheet 3009**.

Chapter 2

Development of optical fiber strain sensors

2.1 Abstract

Optical fibers are well suited to measure Earth strain because they can be stretched over long distances, thereby averaging strain over a large interval. This long baseline is advantageous in that it reduces disturbances due to local effects. We have installed optical fibers ranging in length from a few tens of meters to 2 km in a variety of settings, including vertical boreholes on land and in an icesheet, and horizontally along the seafloor. Due to the high sensitivity of optical fibers to temperature change, an environment of stable temperatures is important. Temperature stability is often available in boreholes or on the seafloor. Longevity of fiber cables and the means to protect the glass fibers from environmental effects and the rigors of deployment are critical issues. These experiments cover a broad range of success in dealing with these issues, with some deployments lasting for nearly six years but others failing immediately.

2.2 Introduction: strain using optical fibers

Measurements of Earth strain provide insights into a variety of geophysical phenomena, including pre and post-seismic deformation associated with earthquakes, volcanic activity, and the tectonics of ocean ridge spreading and slab subduction. Strain measurements could also be well suited to monitor the flow of glacial ice and in geotechnical areas such as hydrocarbon, geothermal, and groundwater reservoir management, as well as slope stability on the seafloor.

Strain ε is defined as $\Delta l/l$, where Δl is the change in initial length l. A long strainmeter is advantageous because strain noise is inversely proportional to the length of the sensor. In geophysical applications, the noise in Δl often results from imperfect coupling to the ground (Langbein et al., 1995). Optical fibers are advantageous for strain measurements: they are capable of having a sensing interval l up to several kilometers in length and optical methods can detect extremely small displacements Δl. The main drawback to optical fiber strain sensors is that the index of refraction has a temperature dependence of about 10^{-5} $^{\circ}\mathrm{C}^{-1}$ (Butter and Hocker, 1978). Thus, fluctuations in temperature can create apparent, but not real, strains. This effect can sometimes be removed with simultaneous measurement of temperature (examples are discussed in Chapter 3), and its limitation is largely dependent on the desired application and environment.

We have developed strain sensors that utilize the advantages of optical fibers. The sensors use two different methods to measure the change in length of the fiber; the choice of method depends on the environment and geophysical signal of interest. The first method uses interferometry. Interferometry is extremely precise, but it requires significant electrical power and must operate continuously to track fringes. Alternatively, we have also developed a low-power, relatively inexpensive strain sensor that utilizes an Electronic Distance Meter (EDM). In the following sections, we describe both of these sensors, how they operate, and their advantages and disadvantages, along with their deployment and practical uses.

2.3 Optical fibers coupled to the Earth

2.3.1 Deployment

Each type of strainmeter we describe consists of a single-mode optical fiber (SMF28) stretched between two fixed positions on or within the Earth. Examples include a borehole or anchors on the seafloor. If deformation of the Earth occurs over the interval spanned by the stretched optical fiber, the length of the optical fiber will change accordingly, since the fibers behave elastically within a specified limit. Monitoring the optical length of the fiber therefore provides a measure of strain integrated along the fiber's path. This is equivalent to the displacement of one endpoint with respect to another.

In all of our sensors, the optical fiber is enveloped within a 1-mm diameter stainless steel tube. The fiber is actually free to slide within the tube, but is fixed to the steel protective member at its endpoints. We typically surround the stainless steel tube with a polyurethane jacket, thereby forming a 4-mm-diameter optical fiber cable (Figure 2.1). During installation, we tension the cable to provide an initial stretch of around a few tenths of 1%. This allows the sensor to accumulate negative strain as well as positive strain. If strain is positively accumulating, the fiber will accommodate it until it reaches its elastic limit.

In practice, we usually design the cable to contain two optical fibers that run the length of the cable. We then splice the optical fibers together at the remote end. This forms a loop, in which light will travel roundtrip through the cable, allowing us to place both the source and receiving optics, such as those that measure changes in length, at one end of the cable. For example, at the lower (deep) end of a borehole, the two fibers will be spliced together within a pressure case. The remaining optical equipment is installed near the well-head, accessible for repairs or alterations. In all cases, we epoxy the fibers to the inner cable wall at both ends, either in a sealed splice housing or in an external clamp fixture (as shown in Figure 2.1). We fix these points to the Earth (e.g., bolted to seafloor anchors, clamped and cemented to the well-casing of a borehole, or frozen in an ice sheet). Strain is then measured over the interval spanning those fixed points.

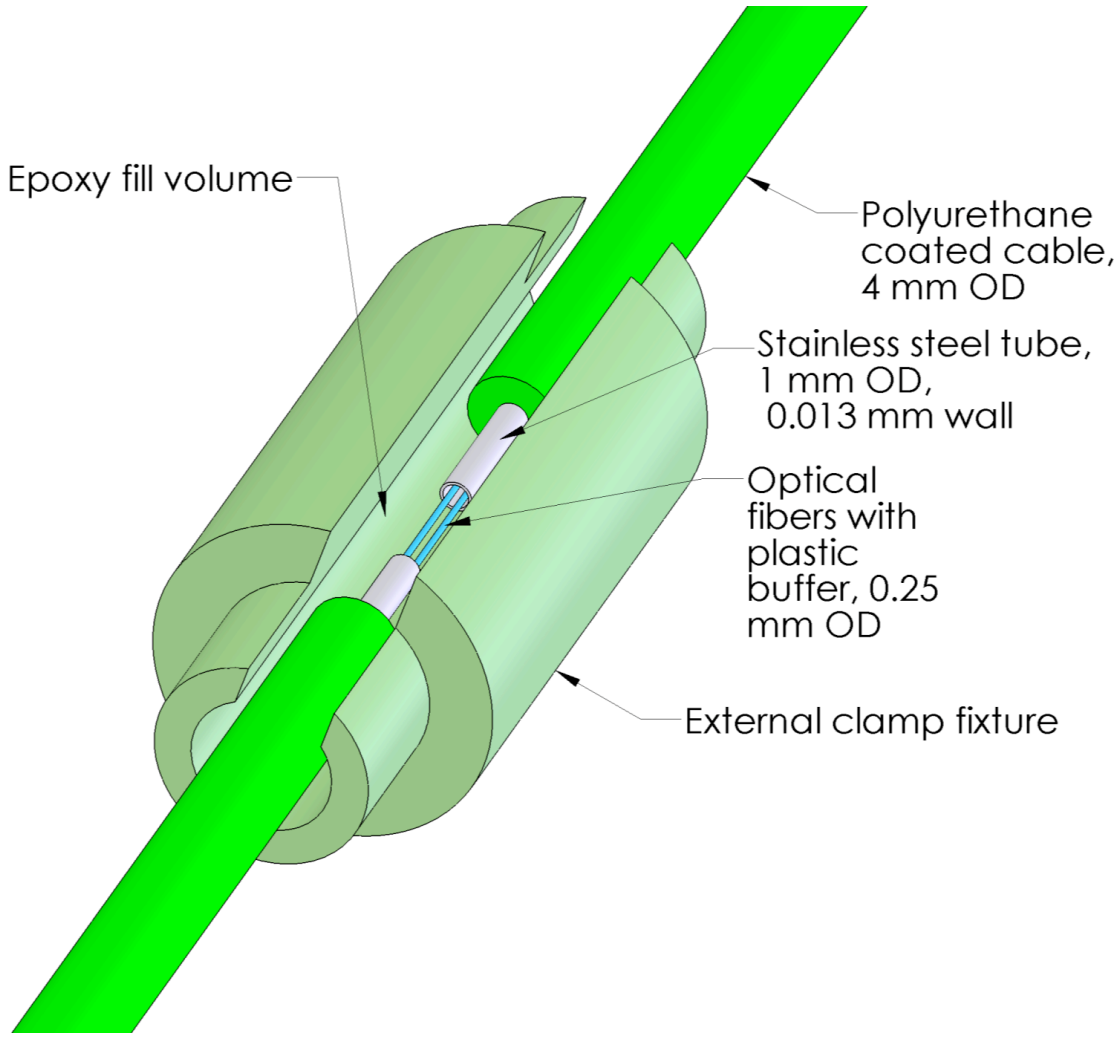

Figure 2.1: Our optical fiber cables usually follow the above design: a 1mm stainless steel tube houses two separate optical fibers. The tube is sheathed in a 4 mm diameter polyurethane outer jacket. At locations where we desire the fiber cable to be mechanically coupled to the Earth, we open the stainless steel tube and epoxy the fibers and the tube to an external clamp fixture, which is in turn attached to an anchor or borehole well-casing. In some cases, we establish the epoxy link at the entrance to a sealed housing where the two fibers are spliced together or otherwise terminated (i.e., silvered ends).

Any friction between the otherwise loose fibers within the non fixed portions of the cable is inconsequential as long as the fibers remain under tension along the entire length, meaning the tension need not be uniform over that interval, but must be nonzero everywhere.

Two aspects of the cable design conflict with one another. A priority is that the cable must protect the optical fibers from damage during deployment and over the lifetime of the sensor. The thick walled, stiff stainless steel jacket and polyurethane buffer accomplishes this goal. Second, the cable and fibers contained within must behave elastically to accommodate both positive and negative strains. Stretching of the cable, however, must also occur without great effort, as we must manually pre-tension the fibers during deployment. This second requirement suggests the use of a thin-walled, elastic jacket. For our applications, the 1 mm diameter, 0.13 mm wall thickness stainless steel tube is a compromise between these two criteria that provides adequate protection. This setup can withstand hydrostatic pressures equivalent to a water depth of 4000 m. It also has an elongation constant of approximately 0.0013%/N, or 0.006%/pound, and an elastic limit around 450 N, or 100 pounds of tension. In practice, we attempt to tension the cables between 90 and 130 N, or 20-30 pounds.

In most cases, we additionally require that the optical fiber cable penetrate a pressure case. The pressure case will typically contain a splice fusing together the two fibers, a pair of 2x2 couplers to create an interferometer, or electronics for optical length metrology. Epoxy provides a good seal for this purpose and we are unaware of failures associated with these penetrations when appropriately rated (for temperature and corrosive fluids) epoxy is used.

Other requirements include a means to tension the cable while it is being installed, and a method to fix the ends of the sensor cable to the span of ground under study. The first of these requirements is well accomplished by having an electric motor provide backtension on spools containing the cable. As the cable comes off the spool and into the borehole or other environment, this ensures there is continuous, nonzero tension on the cable. Fixing the cable to the Earth is a more complex problem that depends on the geophysical application. For example,

a previous experiment by the Zumberge Gravity Laboratory at Scripps Institution of Oceanography measured strain over a 1000-m thick ice sheet at Sipole Dome, Antarctica (Zumberge et al., 2002). In that application, a hot-water rig drilled a borehole in the ice, creating liquid-water filled holes that lasted several hours before refreezing. During the liquid water period, they spooled an optical fiber cable with a weight on the pressure housing containing the spliced, lower end into the hole. The weight held the fiber over nonzero tension until the borehole froze. Once the cable was frozen in place, subsequent changes in length corresponded to strain in the ice sheet.

Boreholes on land (or hypothetically, at sea) present other difficulties. We have established sensors at two deep boreholes: at LVEW (Long Valley Exploratory Well, for volcano research), and at SAFOD (San Andreas Fault Observatory at Depth, for earthquake research). At both of these observatories, a drill rig drilled the boreholes and lined them with a steel well-casing prior to our arrival. During installation of the strainmeter, a second pipe, or inner well-casing, was lowered into the outer well-casing. At LVEW, this involved a 6-cm-diameter grout pipe and at SAFOD, we used a 24-cm-diameter steel well-casing. As the pipe was assembled at the surface and lowered into the well, we attached the optical fiber cable to the exterior of this inner casing using a custom designed fixture (Figure 2.2). The fiber cable was then strapped to the exterior of these pipes as subsequent sections were lowered into the well (Figure 2.3). As described earlier, nonzero backtension was supplied to the cables by motorized supply spools. When the entire inner casing had been assembled and lowered to the desired sensor depth, cement was pumped into the annular region between the inner and outer casings. This results in the optical fiber cable being stretched and well coupled to the Earth over its entire interval (Figure 2.4).

We have not limited ourselves to measurements of strain in boreholes. Establishing a seafloor strainmeter, either across a spreading center or slope considered at risk for failure and resulting submarine landslides, remains an important goal. Seafloor installations, however, are more involved. They require cognizance of geotechnical considerations and more importantly, there are unique challenges

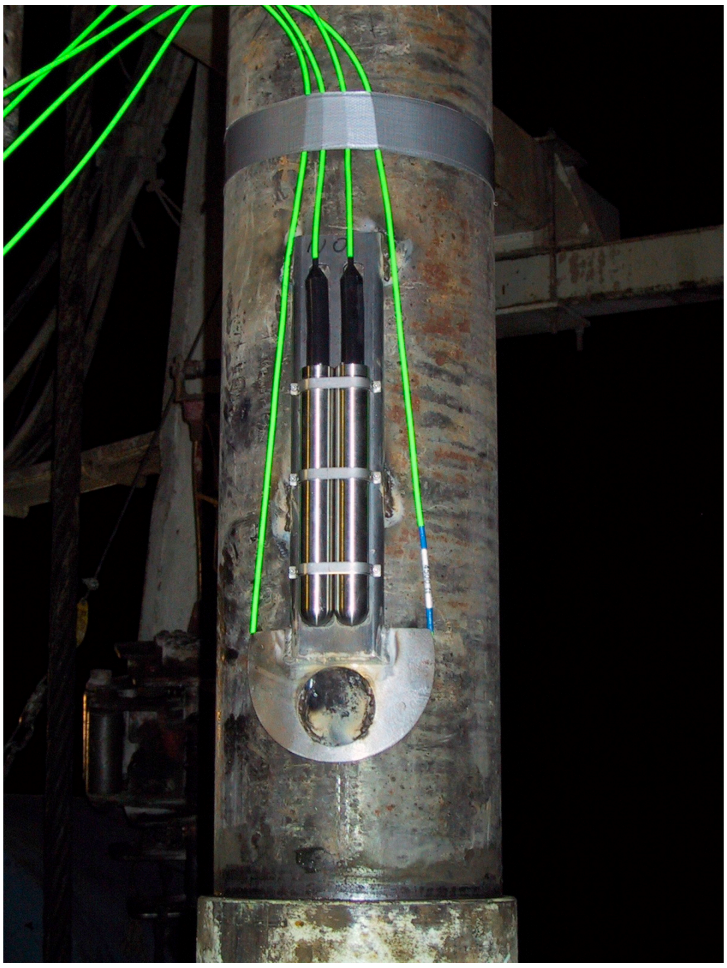

Figure 2.2: A photograph displaying two pressure housings containing spliced fibers during the installation at SAFOD. The pressure housings are fixed to the 24-cm-diameter inner casing. The housings are simply an o-ring sealed bottle. Within the bottle, the two fibers in the cable are fused together, thereby forming a loop. We designed our installation to include an additional loop of unspliced fiber for redundancy.

Figure 2.3: As the inner casing was lowered into the well, the fiber cables were strapped to the exterior of the inner casing to hold form and tension until cement was pumped into the annular region. In this photo, we display a lower splice housing for a shallower strain sensor and two fiber cables going to deeper strain sensors. Also visible is a casing "centralizer". These devices were periodically attached along the casing, typically every 2-3 pipe segments, to keep the cables from pinching between the walls of the inner and outer casings. Not shown are overhead sheaves through which the cables are routed upward and then to the motorized spools that provide nonzero backtension throughout the deployment.

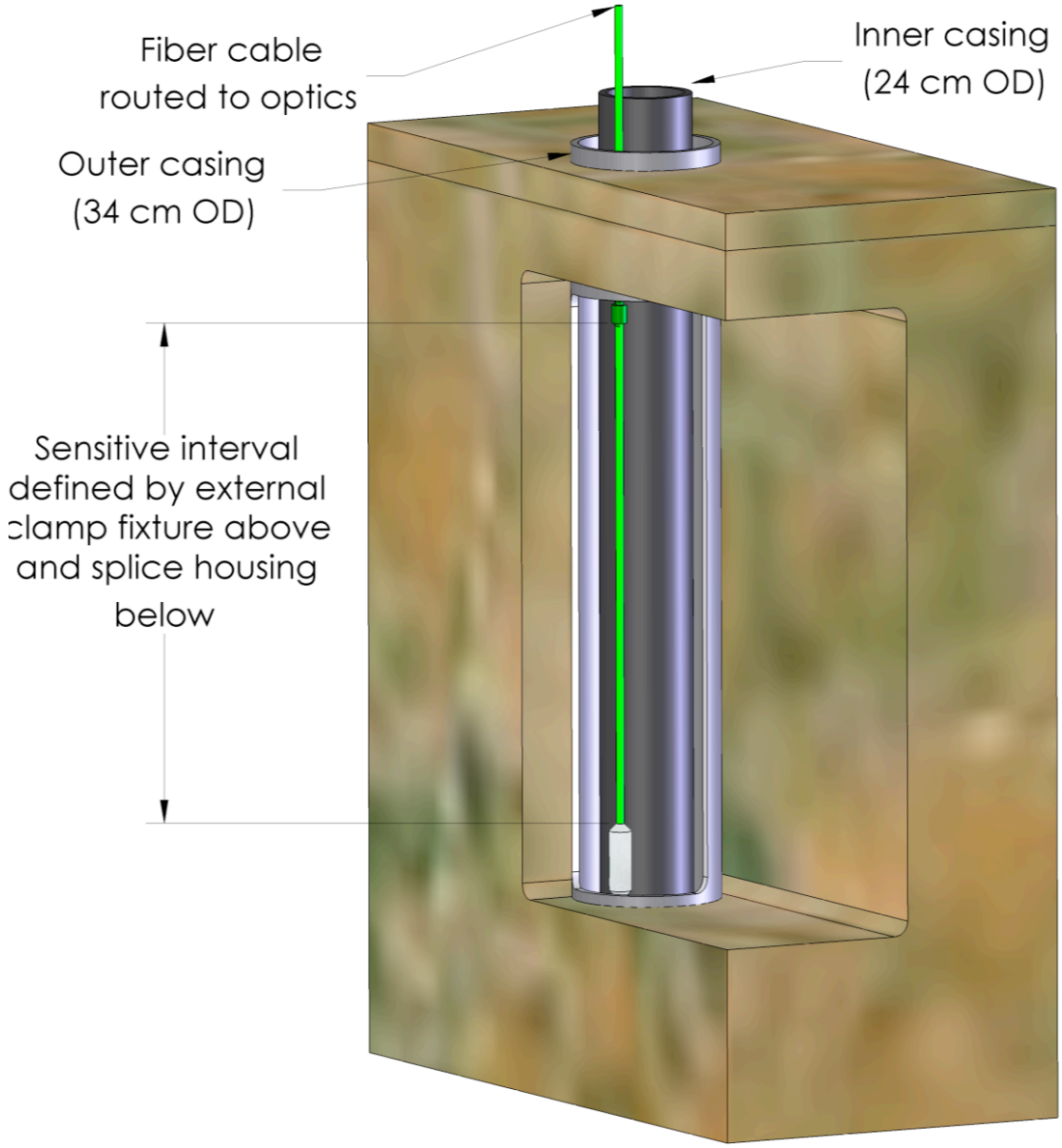

Figure 2.4: This schematic view shows the Earth cut around a borehole to reveal the strainmeter. The outer casing was cemented to the ground prior to sensor installation. The optical fiber strain sensor was attached to the inner casing and was supplied with back-tension as it was lowered into the well. After the sensor is lowered to the desired depth, cement fills the annular region between the inner and outer casings to complete the installation. Note: not shown are valves and other surface fixtures giving access to the borehole. The scale is also severely exaggerated.

to ocean deployments that require a detailed description. For the moment, we save most of that description for Chapter 3.

2.3.2 Longevity

Longevity of the sensor is important due to the high cost of construction. In most geophysical environments, the optical fiber cables are subjected to significant hydrostatic pressures. Deep borehole deployments are also subjected to high ambient temperatures, often exceeding 100°C, in the presence of highly corrosive fluids. Our cable design has experienced a good but not perfect performance in these environments.

Table 2.1 summarizes the deployments we have carried out and the longevity of the fibers in the three environments in which we have worked (land boreholes, ice boreholes, and horizontally along the seafloor.)

Of all our installation environments, the Antarctic boreholes of Zumberge et al. (2002) were the most benign, despite the extreme cold. They armed ten boreholes, each containing two fiber cables. Ice temperatures typically ranged from −20°C at the surface of the ice sheet, warming to about 0°C at the lowest point, just above the bedrock. After the drilling transient temperature dissipated the temperature in the ice was stable to millidegrees. Repeated optical time-domain reflectometer (OTDR) measurements revealed no changes in the optical fiber properties other than the lengths due to strain. Strain rates measured 229 $\mu\varepsilon$/year[1].

Just as deployment of our strain sensors in land boreholes was more complicated than in ice, there are also greater problems to longevity. At SAFOD, we installed two loop strain sensors, one to a depth of 864 m, and another to 782 m. Each of these cables terminates at its lower end in a pressure case containing the two fibers fusion spliced together. This creates a loop. Since the splices were done on site atop the drill rig, they are relatively high in loss compared to typical results in the laboratory. These pressure cases were then bolted to fixtures which

[1]Strain is unitless, but is typically given a unit such as a $\mu\varepsilon$, or microstrain, meaning $\Delta l/l = 10^{-6}$; similarly, a nanostrain of 1 $n\varepsilon$ corresponds to $\Delta l/l = 10^{-9}$.

Table 2.1: Optical fiber strainmeter installations

Location	Coordinates & Installation Date	Type	Max Depth (m)	Interval (m)	Temp (ºC)	Longevity (Years)	Failure	Comments
LVEW (Long Valley Exploratory Well), vertical borehole on land	37º 40.8' N 118º 54.5' W Aug. 2003	Interferometer	2125	50	103	0.25	2x2 coupler failed	Coupler at 2125 m depth
		EDM loop	2125	2125	103	4.0 +	None	Anomalous attenuation
SAFOD (San Andreas Fault Obsevatory at Depth), vertical borehole on land	35º 58.0' N 120º 33.1' W Oct. 2004	Interferometer	1320	50	64	0.3	2x2 coupler failed	Coupler at 1320 m depth
		Interferometer	864	856	51	2.88	Splice failed	Failure accompanied by additional borehole activity
		Interferometer	782	773	46	5.0 +	None	2x2 coupler at surface
Sipole Dome, Antarctica, vertical boreholes in ice sheet	81º 39.3' S 148º 49.3 W Dec. 1997	EDM loop	985	985	-20	4.0 +	None	20 cables of various lengths were installed
Pacific Ocean offshore San Diego, horizontal seafloor deployment	32º 42.1' N 117º 36.2' W Jul. 2000	EDM loop	1119	503	4	0.2	Electronic failure	No indication of fiber failure

we welded to the exterior of the inner well-casing. Once the inner casing and strain sensor were lowered to their target depths, we opened the upper ends of the cables and we epoxied the fibers to the stainless steel tube at a point destined to rest at about 10 m below the ground surface.

OTDR measurements made on the SAFOD strain cables at different times showed no significant degradation to the cables or splices for the first 2.8 years following installation. The 864 m optical fiber cable ultimately did fail during subsequent drilling and installation of other sensors within the 24-cm-diameter inner casing. The mode of failure was degradation of the splice at the lower end at 864 m depth. The 782 m sensor remains operative.

We employed an identical deployment scheme at LVEW; rather than use a splice at the lower end of a single cable, however, we formed a loop of cable on two separate spools and attached the loop to the lower termination point. This circumvented the need for a splice housing at the bottom depth of 2125 m. Despite eliminating the deep splice, Figure 2.5 demonstrates some degradation to this cable. Prior to deployment, we checked the cable with the OTDR and found what we consider normal attenuation of a few tenths of a dB/km. Twelve hours following installation, a visible fault-finder test – which simply involves directing visible light from a laser into the cable and witnessing it return through the far end – revealed the installation was without fault. We accessed the cable three months following installation in order to attach the length measuring optics; at this time, we discovered attenuation of around 2.5 dB between the top and the bottom of the sensor, or 5 dB round trip. This attenuation, however, does not appear to increase over time. Figure 2.5 shows OTDR results from 2.5 years following the initial measurement, and the attenuation curve appears the same[2].

In both the LVEW and SAFOD installations, we added optical fibers other than whose OTDR results are shown in these tables and figures. We configured these fibers as Mach-Zender interferometers. In this configuration, a 2x2 coupler split the light from the down going fiber into two arms. A second 2x2 coupler subsequently recombined the light in the same pressure case. One of the two arms

[2]The offsets in this figure between November 2004 and July 2007 are arbitrary, added for clarity. There is no increase in relative loss over time.

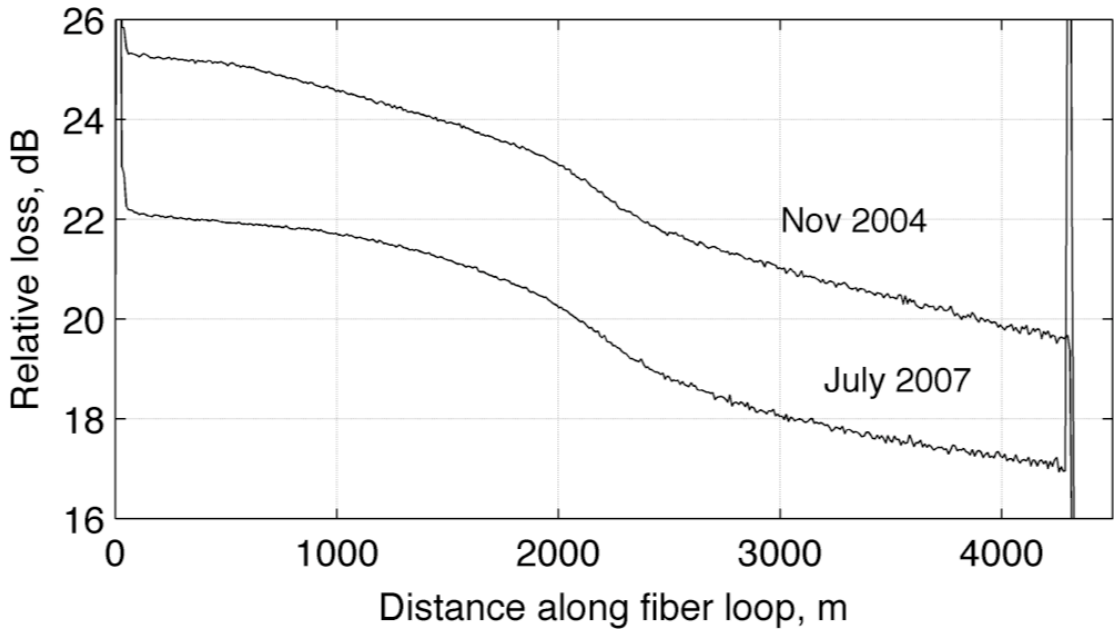

Figure 2.5: OTDR records from the "loop" cable at 2125 m depth at the LVEW observatory. Attenuation exists over the depth of the sensor. Attenuation does not worsen with time. Note: the offsets between the November 2004 and July 2007 measurements are arbitrary and were added for clarity.

made a loop farther down the borehole, thereby forming a deep, short strain sensor. Our intended advantage in this configuration was to isolate a strain sensor far below the surface, which would lessen surface temperature contamination. Neither of the Mach-Zender configurations survived. OTDR measurements indicated that both 2x2 couplers within the pressure housing failed within a few months of deployment. Optical epoxy was relied upon to bond the fibers to the 2x2 couplers, and we believe that epoxy likely could not withstand the harsh thermal environment. The temperature at the failure point in the LVEW borehole is 103°C (2125 m depth). At SAFOD, the temperature at the failure point is 64°C (1320 m depth).

2.3.3 Optical length measurement techniques

The strain sensor is not complete without an optical system capable of measuring changes in length. We have developed two types of optical methods to sense variations in the optical lengths of our optical fiber strainmeters. The first used in-

terferometry. This results in extremely high strain resolution. The second method, that used by an EDM, employs a time-based measurement to determine length. This second method has advantages to the interferometric method depending on application, but its resolution is limited.

Interferometry

We have developed several geophysical instruments that rely upon interferometry to track small displacements. Our requirements are the ability to resolve displacements on the order of picometers while observing displacements that may actually span several centimeters. To fulfill these requirements, we use a digital signal processor (DSP) based optical fringe resolver (Zumberge et al., 2004).

We form an optical fiber Mach-Zehnder interferometer in our borehole at SAFOD. One arm of the interferometer is the borehole loop fiber, and the other is a short reference arm at the surface. We modulate the optical path difference to obtain a second fringe signal in quadrature with the direct fringe signal. We then input the two fringe signals into a fast A/D converter. A custom algorithm in the DSP samples the quadrature signals and continuously updates the parameters of an ellipse that characterizes the fringe pattern. At the same time, the algorithm instantaneously computes the optical phase.

Advantages of this method include extremely high resolution – picometers – along with linearity and wide dynamic range. There are also some limitations. This system requires continuous electrical power of several tens of watts to operate the laser, analog electronics, DSP, and the computer for logging, as well as sending the data to our offices via telemetry. If the data stream is interrupted for any reason, such as the laser light briefly dropping out, there is no way to bridge the gap other than interpolation. It becomes a purely relative measurement. In locations where such constraints are trivial, interferometry would be the preferred method, as it allows observations of dynamic strains sampled at many Hertz.

Electronic Distance Meter

EDMs are surveying tools designed to measure distances to remote reflectors. They work by timing the round-trip travel time of light through the atmosphere. Most EDMs emit intensity modulated infrared light and can collect returns from reflectors placed several kilometers distant. The most accurate EDMs can determine the distance to a reflector a few kilometers away to within $\pm$ 1 or 2 mm (Rüeger, 1990).

These instruments are designed to measure distances through the atmosphere. They can be modified, however, to measure the length of an optical fiber by focusing the emitted beam into the fiber's core and then coupling the light emerging from the fiber's return end into the EDM receiving optics. The difference in index of refraction between the atmosphere and the optical fiber and its effect on length, as well as its dependence on strain and temperature, must be taken into account (see, e.g., Zumberge, 1997). We cover these issues in greater detail in Chapter 3.

Whereas interferometric strain sensors are sensitive to strains on the order of $n\varepsilon$, EDM methods are sensistive to at best 1 $\mu\varepsilon$. This limit is adequate for some applications. Furthermore, several experiments examining optical fibers at long periods reveal that the inherent stability of an optical fiber's index of refraction is around one part per million per year (Zumberge and Wyatt, 1988). The EDM precision is on par with that specification.

The modest precision and lower sampling rates of EDMs are their main disadvantages for being the length measuring element of an optical fiber strainmeter. Their advantages are low power and the ability to provide absolute length measurements, as opposed to simply changes in length. EDMs require a few seconds and electrical power on the order of 3 watts to determine the length of an optical fiber. Since they make absolute measurements, EDMs can be turned off, thereby conserving power, or completely removed from the sensor for an indefinite time period without losing the absolute strain record. In choosing to use an EDM, however, it is important to consider what types of signals are desired to be observed, as it is unlikely to be useful for high frequency signals.

Much of previous work using EDMs by the Zumberge Gravity Laboratory utilized a Leica DI2002, which is no longer manufactured. We have since developed systems that use a Dimetix DLS-A 15, particularly for use in a seafloor strainmeter system (see Chapter 3.) Data from each EDM are presented in the following sections. The choice of EDM does not necessarily matter; however, it is best to use the same EDM over the longevity of a strain sensor in case there is bias in the absolute accuracy.

For over ten years, the Zumberge Gravity Laboratory has tested the length stability of a sample optical fiber in their laboratory. They wound 500 m of optical fiber onto a 15-cm-diameter brass mandrel, which was isolated in storage in 1997. We frequently measure the length of this fiber with an EDM (and the temperature of the mandrel using thermistors) to track the stability of this metrologic technique. The results of this ongoing experiment are plotted in Figure 2.6. We consistently observe a stability of slightly better than 1 ppm per year.

2.4 Results from interferometric borehole sensors

We next present initial results from our deep borehole installation at the SAFOD borehole. SAFOD is adjacent to a major fault zone near Parkfield, California, that is of high interest to the earthquake hazards community. Greater details regarding hazards at Parkfield and SAFOD are in Chapter 4. In this section, we focus on initial results that demonstrate the operation of the sensor.

Installation of the strainmeter occurred on October 2 and 3, 2004. Several cables immediately broke due to an unexpected protrusion in the "blowout preventer" at the surface of the borehole. We required on-site splices of several severed cables, complete with fusion splices of the fibers and epoxy-based penetrations of the cables into the splice pressure cases. Our target strain depth was initially 1320 m; because of cable breaks and the earlier failure of the 2x2 couplers, however, we only preserved two fiber loops: one to a depth of 864 m, and another to 782 m. Data here is from the deeper loop installation, although most of the data in

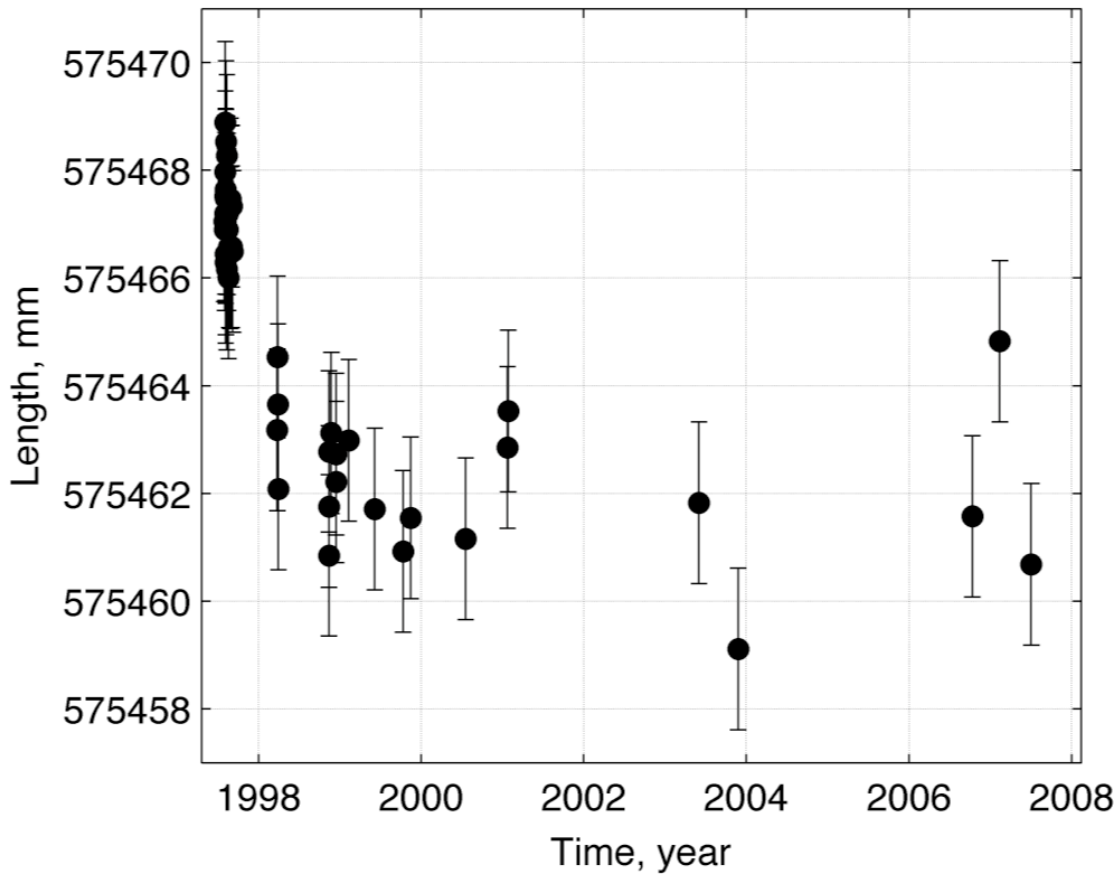

Figure 2.6: EDM measured lengths of a reference fiber wrapped on a mandrel in our laboratory. Following assembly of the mandrel, there was initial relaxation in the fiber's length, but the cable has been stable to 1 ppm/year over the following decade.

Chapter 4 is from the 782 m deep assembly.

A small trailer near the well-head contains the interferometer laser and electronics. Conduit housing optical fibers run from the trailer to the wellhead. Mounted to the wellhead is a junction box where a pair of 2x2 couplers and a PZT modulator form the Mach-Zehnder interferometer. One arm of the interferometer travels down the 782 m deep cable and back up the loop. The borehole fiber is tensioned between the deep turnaround and a point 9 m below the surface, where it is fixed to the well casing. The short, roughly meter in length reference arm of the Mach-Zehnder interferometer is coiled within the junction box. This arm is fully exposed to surface temperatures which may require compensation due to the aforementioned temperature dependence on the index of refraction.

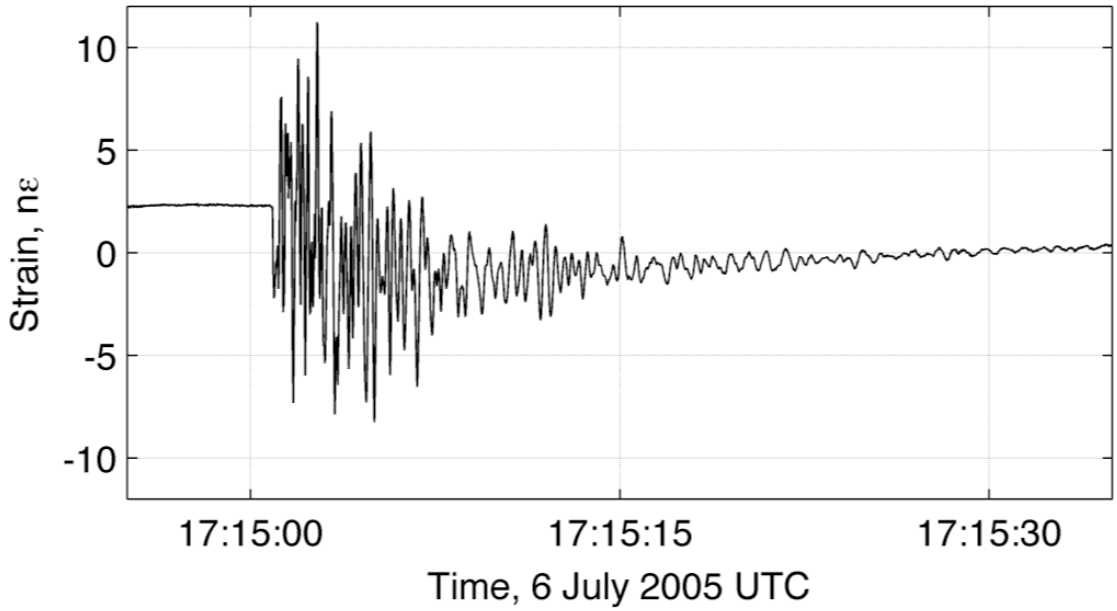

Figure 2.7: A strain record from the 864 m deep interferometer at SAFOD during a nearby (5.3 km) magnitude 2.8 earthquake.

Figure 2.7 shows the observation of dynamic strains from a magnitude 2.8 earthquake located 5.3 km away from SAFOD. This record is interesting. Note the low noise in the record before the arrival of seismic energy. The power spectral density of the noise at 1 Hz is less than 0.01 $n\varepsilon \mathrm{Hz}^{-1/2}$. There is an apparent offset, or permanent strain induced by the local earthquake dislocation, of about 3-4 $n\varepsilon$ in the record. Observations of this offset and more for other events are discussed

in Chapter 4.

Surface temperature variations become problematic at longer time scales. Figure 2.8 shows a one week record of strain. Surface air temperatures at the site varied with a peak-to-peak amplitude of 23°C over this interval. Variations in laser wavelength are responsible for much of the daily noise; since this effect is experienced in both the reference and borehole arms of the interferometer, we can subtract the laser influence from the reference arm to correct the signal. The impact of temperature on the fiber itself, however, remains problematic. As of this date, we do not have a simple way of correcting for these temperature effects. The event late in day 149 occurs when 1000 psi of pressure was released from the borehole and is likely the result of both strain release and temperature change. One of our goals is to record strain tides whose amplitudes are a few tens of $n\varepsilon$. Further work on the system is intended to reduce noise by adding appropriate thermal insulation and improving the laser system.

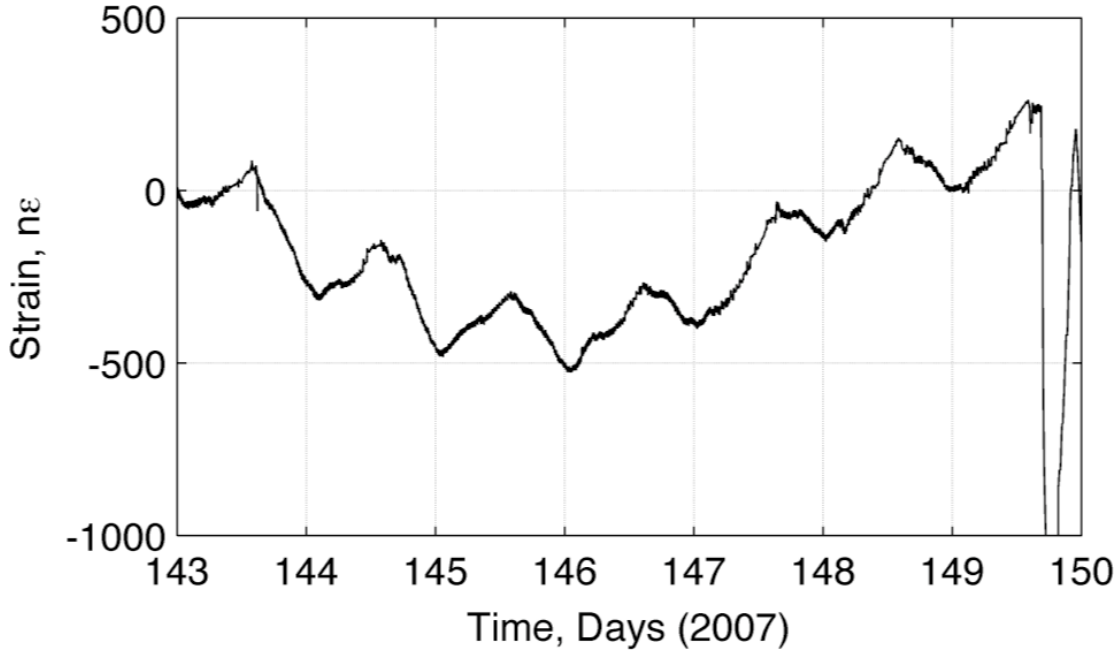

Figure 2.8: The strain record from the 864 m deep SAFOD interferometric instrument over a once week period. Noise is primarily associated with temperature change.

2.5 Results from EDM based borehole sensors

The Zumberge Gravity Laboratory has used EDMs to monitor strain in both the Antarctic and LVEW boreholes. In the Anarctic ice sheet, 20 fibers extending to a maximum depth of 985 m were installed in the hot-water drilled boreholes in the ice (Zumberge et al., 2002). Annual EDM surveys of the fibers occurred over a four year period. They observed strain rates as high as 229 $\mu\varepsilon$/year. RMS length residuals of the fiber lengths were 2.4 mm.

The LVEW installation is at an active volcanic region near Mammoth Lakes, California. As mentioned earlier, the LVEW setup utilizes a loop cable extending from the surface to 2125 m depth. There are no splices in the cable and its loss attenuation with depth was shown in Figure 2.5. In November 2004, we installed a Leica DI2002 EDM and data logger that sampled the cable length every three hours. We continued this operation for eight months. Significant noise occurred in the record during the final 1.5 months of continuous EDM operation. We made no further measurements until July 2007, when we made a manual, campaign style measurement with the EDM. This record is shown in Figure 2.9. The noise data in mid 2005 are anomalous; the 2007 data point would align with the trend of the quiet data (from late 2004 to early 2005) preceding the noise. An important consideration is that small changes in the alignment of the optics could result in tens of mm of variation. Zumberge (1997) previously observed the phenomena in the laboratory, although to a much lesser extent. In addition, the attenuation of the cable with depth likely exacerbates this effect. The intensity of the return light is barely adequate for the DI2002 EDM to make a length measurement. The record suggests a shortening of the cable of three parts in 10^5 over the three year interval. To determine if this shortening is real, we would need to make a temperature correction. A temperature profile of the borehole was obtained in May 2000. A second profile would be necessary to observe any large temperature differences so we could correct the record.

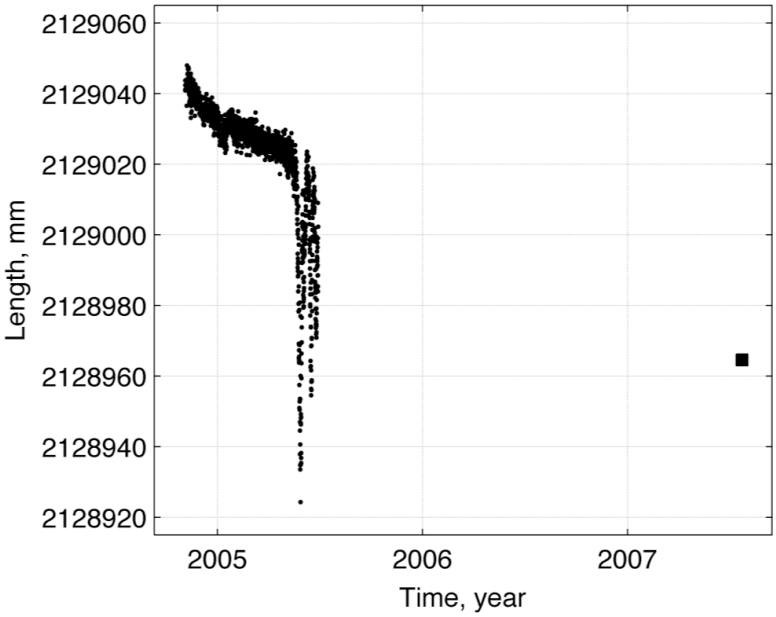

Figure 2.9: An EDM record from the 2125 m deep loop cable at LVEW.

2.6 Results from EDM based seafloor sensors

2.6.1 Overview

Many desirable locations to monitor deformation lie beneath the ocean surface. Most of the world's plate boundaries are underwater, including ocean ridge spreading centers and slab subduction. The seafloor is also littered with landslides and mudflows on continental slopes that in some cases possess the potential to generate tsunami. Monitoring regions of potential failure are an important part of tsunami mitigation efforts. Additionally, there are growing geotechnical applications related to hydrocarbon production, where monitoring seafloor movements may be useful for both hazard assessment and reservoir management. To address these applications, we have developed an optical fiber seafloor strainmeter that utilizes an EDM. Our success towards this goal has been limited. We have attempted to deploy seafloor strainmeters offshore La Jolla, California as well as in the Santa Barbara Basin, California. As an introduction, in this section, we describe general aspects of sensor development and some of the challenges we have faced. Details regarding the specifics of the Santa Barbara deployment are in Chapter 3.

The Zumberge Gravity Laboratory previously developed a prototype sensor consisting of a 503-m-long optical fiber cable stretched between two concrete weights places on the seafloor, at a water depth of 1100 m off the coast of San Diego, California. They used a dynamically positioned ship to hold positions while we lowered the two concrete weights to the seafloor. One anchor held a spool of cable. Attached to the other anchor was the EDM and recording electronics in a custom designed pressure case. The fiber ran between both anchors, penetrating the EDM pressure case. Both anchors were initially set on the seafloor. The anchor hosting the active electronics was then moved laterally, thereby pulling the cable out from the spool. Drag on the spool provided our required back-tension. Careful and slow maneuvering of the ship enabled a 1/2 m stretch to be applied over the 503-m length of cable before the second anchor was set in the sediment. This maneuver resulted in a taut optical fiber cable laying between the two anchors. This particular location was a flat, featureless, sediment-draped surface, chosen specifically for its suitability for a test.

The EDM sampled the length of the cable every three hours. After two months, they uploaded the data to the surface using an acoustic modem. Figure 2.10 shows the record from this experiment. They observed an initial settling of the fiber into the sediment over the first couple weeks, but over time, the length of fiber was reproducibly observed. They expected no geophysical strain to accumulate at this test site and EDM measurements made before and after deployment demonstrated that the fiber was appropriately tensioned. They observed an 8 mm shortening with an exponential relaxation with roughly a 20 day time constant. This was most likely from the relaxation of the cable in the sediment. Scatter around the exponential fit is less than 1 mm. After 100 days, the slope of relaxation was projected to be less than 1 mm per year. The success of this prototype sensor is the basis for a more advanced system that we developed in the next chapter.

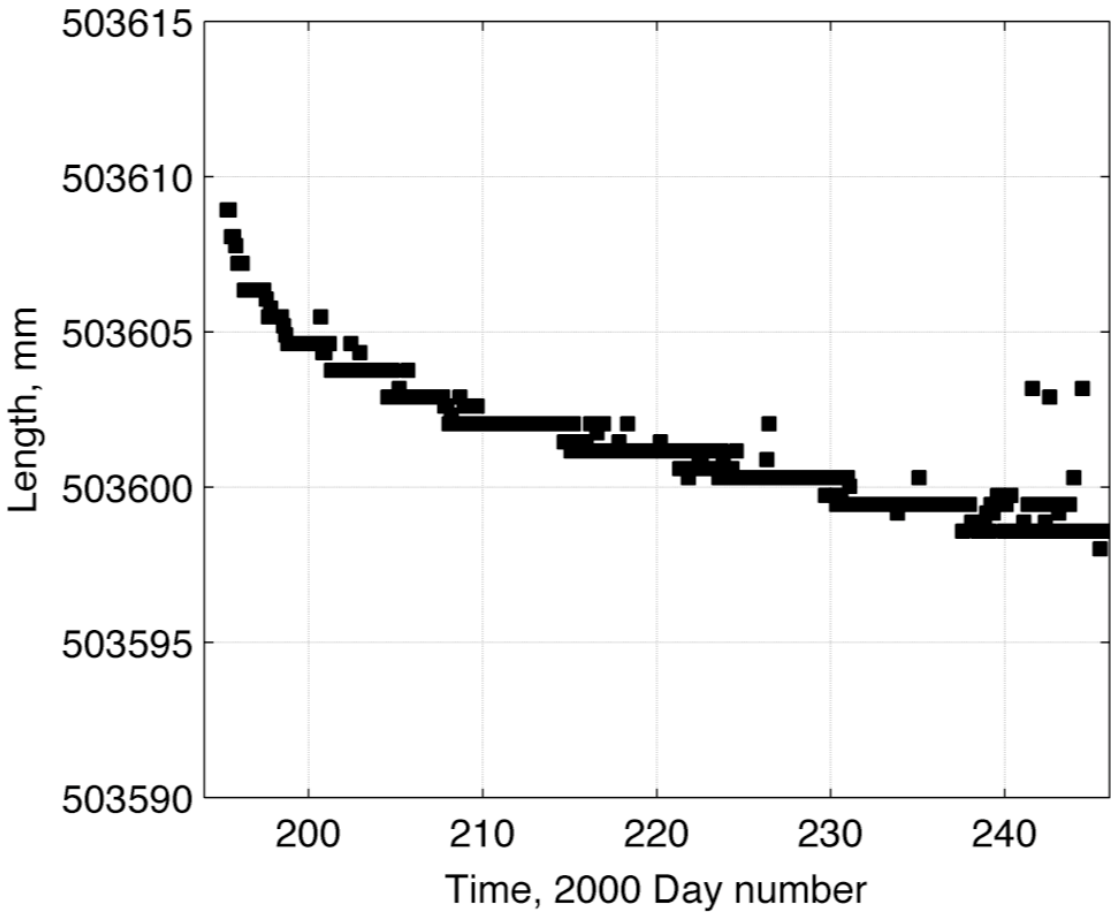

Figure 2.10: The EDM record from a 503 m long optical fiber cable positioned on the seafloor offshore San Diego, California.

2.7 Conclusions

Optical fibers are useful as strain sensors in geophysical applications and are a viable alternative to other methods such as laser-vacuum strainmeters or volumetric-fluid or capacitance strain sensors (Agnew, 1986; Linde and Sacks, 1995). Optical fibers can be deployed at lengths up to several kilometers in a variety of harsh environments such as ice, sea water, and the high temperatures, pressures, and corrosive fluids in deep boreholes. Limitations to precision at long periods are mainly due to the large temperature coefficient of the optical fiber's index of refraction and potentially, aging and degradation of the fiber. These factors are unavoidable in any sensor without resorting to an evacuated path (Agnew, 1986). At short periods, however, strain noise in an optical fiber may be significantly lower than a tenth of a nanostrain. Fibers survive for periods of several years in the extreme environment of a borehole and have shown no signs of continuing degradation. In the following chapters, we discuss applications of our optical fiber strain sensors to specific studies of geohazards: slope stability in the Santa Barbara Basin (Chapter 3), and earthquake hazards at SAFOD (Chapter 4).

2.8 Acknowledgements

We would like to thank the large numbers of scientists, engineers, and technicians who have helped advance this research. We are indebted to G. Austin, P. Durdevic, W. Ellsworth, S. Hickman, R. Horn, E. Husmann, M. Kirk, J. Lemire, P. Malin, E. McGrath, M. Norenberg, G. Openshaw, S. Sacks, K. Walker, P. Walsh, and M. Zoback.

Some of the text and figures in this chapter were previously published in: **Blum, J., Nooner, S., and Zumberge, M., 2008: Recording Earth strain with optical fibers.** ***IEEE Sensors Journal*****, 8(7), 1152-1160.** The author's contributions to this chapter were writing the published manuscript, as well as helping to design, develop, and deploy the optical components at the SAFOD and LVEW boreholes and for seafloor applications. The Zumberge Gravity Laboratory at Scripps Institution of Oceanography was responsible for the Antarctica and

prototype seafloor strainmeter experiments; those studies were performed prior to this dissertation.

REFERENCES

Agnew, D., 1986: Strainmeters and tiltmeters. *Rev. Geophys.*, **24**, 579–624.

Butter, C., and Hocker, G., 1978: Fiber optics strain gauge. *Applied Optics*, **17**, 2867–2869.

Langbein, J., Wyatt, F., Johnson, H., Hamann, D., and Zimmer, P., 1995: Improved stability of a deeply anchored geodetic monument for deformation monitoring. *Geophys. Res. Lett.*, **22**, 3533–3536.

Linde, A., and Sacks, I., 1995: Continuous monitoring of volcanoes with borehole strainmeters, Mauna Loa revealed: structure, composition, history, and hazards. *Geophysical Monograph*, **92**, 171–185.

Rüeger, J., 1990: *Electronic distance measurement.* Springer-Verlag, Berlin, Germany.

Zumberge, M., 1997: Precise optical path length measurement through an optical fiber: application to seafloor strain monitoring. *Ocean Eng.*, **24**, 531–542.

Zumberge, M., Berger, J., Dzieciuch, M., and Parker, R., 2004: Resolving quadrature fringes in real time. *Applied Optics*, **43**, 771–775.

Zumberge, M., Husmann, E., Elsberg, D., Harrison, W., Morack, J., Pettit, E., and Waddington, E., 2002: Measurement of vertical strain and velocity at Siple Dome with optical sensors. *J. Glaciology*, **48**, 217–225.

Zumberge, M., and Wyatt, F., 1988: Optical fiber interferometers for referencing surface benchmarks to depth. *Pure Appl. Geophys.*, **152**, 221–246.

Chapter 3

FOSS: A fiber optic seafloor strainmeter

3.1 Abstract

We develop a Fiber Optic Seafloor Strainmeter (FOSS) to monitor deformation across a potentially active (via downslope creep) headscarp of a future submarine landslide in the Santa Barbara Basin (for geologic details of this region, see Chapter 5.) The strainmeter uses an electronic distance meter – or EDM – to interrogate the length of the optical fiber, which is stretched between two steel anchors on the seafloor. The system is capable of detecting changes in length of a fiber to less than 1.5 mm. We designed a method to bury the fiber cable in the seafloor sediments to protect it from environmental influences using a towed sled with mechanical releases of the steel anchors. The system includes an acoustic modem for periodic data offload. In this chapter, we discuss in detail the physics of optical fibers, the influence of temperature on length measurement, possible pitfalls (and solutions) of the EDM, and the details of the deployment design. We were unsuccessful in deploying a working sensor but were able to diagnose the problems with the deployment system. Several working sensors remain in our laboratory and we hope to revisit the problem in the future.

3.2 Introduction

Monitoring deformation of the Earth is possible using a variety of techniques. Satellite methods such as laser altimetry, InSar, and the Global Positioning System (Rees, 2001; Blewitt et al., 1992), surveyor tools including electronic distance meters and total stations (Langbein, 1989), and even continuously recorded laser strainmeters (Wyatt et al., 1994) are all used to monitor centimeter or less movements on the Earth's surface over baselines from meters in length to several hundred kilometers. These techniques are well developed on land, but many tectonically interesting provinces and environmentally sensitive areas of economic activity, such as hydrocarbon production, are located offshore. With ocean covering nearly 71% of the Earth's surface, there are large gaps in deformation coverage. Electromagnetic energy, the basis of EDM and satellite technologies, attenuates in seawater. Other monitoring methods are therefore required. One successful technique is to use acoustic methods (see, e.g, Chapter 5), which can measure seafloor displacements to the precision of a few cm over kilometer baselines (Chadwick et al., 1995; Spiess et al., 1998).

The field of fiber optics presented in Chapter 2 is yet another technique that has the potential to measure geophysical deformation on the seafloor to near millimeter absolute accuracy. Seafloor spreading, movement across faults, and monitoring of seafloor cracks that might represent actively forming headscarps of imminent submarine landslides are all seafloor phenomena to which optical fiber strain sensors could be applied within the oceans.

In this chapter, we describe the development and attempt to deploy a Fiber Optic Seafloor Strainmeter (FOSS) that monitors the length of an optical fiber on the ocean bottom. FOSS is an outgrowth of the EDM sensor described in Chapter 2, an earlier attempt to develop a seafloor strain sensor.

3.3 Physics of optical fibers

An optical fiber is small, flexible, requires no electrical power, and can transmit large quantities of information along its path with little attenuation.

These features, along with certain physical properties, allow an optical fiber to be used as an environmental sensor. Temperature, pressure, strain, and other parameters can all be measured using optical fibers (Butter and Hocker, 1978; Hocker, 1979; Zumberge et al., 1988; Zumberge and Wyatt, 1998; Zumberge et al., 2002).

An optical fiber is comprised of a core (glass which carries an impulse of light,) cladding (glass which reflects light back into the core, forming a wave guide,) and a protective buffer coating. Due to the index of refraction of the glass core, the physical length of a fiber (L) will appear optically (L_{op}) as

$$L_{op} = nL, \tag{3.1}$$

where n is the refractive index. If the fiber is strained, it will undergo a physical (and thus optical) change in length but the refractive index also changes. The change in optical length will go as

$$\Delta L_{op} = n\Delta L + L\Delta n. \tag{3.2}$$

The change in refractive index Δn depends on the material properties as well as the amount of strain. According to Butter and Hocker (1978),

$$\Delta n = -\frac{1}{2}n^3 \left[\frac{\Delta L}{L}(1-\mu)p_{12} - \mu\frac{\Delta L}{L}p_{11} \right], \tag{3.3}$$

where μ is the Poisson ratio for the fiber and p_{ij} are elements of the strain-optic tensor. Substituting into the expression for ΔL_{op} we have

$$\begin{aligned} \Delta L_{op} &= n\Delta L - \frac{1}{2}n^3 \left[(1-\mu)p_{12} - \mu p_{11}\right]\Delta L & (3.4)\\ &= (n-k)\Delta L & (3.5)\\ &= \nu\Delta L, & (3.6) \end{aligned}$$

where $k = \frac{1}{2}n^3 \left[(1-\mu)p_{12} - \mu p_{11}\right]$ and $\nu = n - k$. For typical values of $n = 1.48$, $p_{11} = 0.113$, $p_{12} = 0.252$, and $\mu = 0.16$ (Bertholds and Dändliker, 1988), we are left with $k \cong 0.31$ and $\nu \cong 1.17$.

A fiber's optical length also changes as a function of temperature (T). The material properties of n make it temperature dependent and the fiber core will

undergo a slight thermal expansion. If the fiber is anchored to the Earth, only the optical length is temperature dependent, as the physical length can only change as the Earth changes. It therefore follows that $dL/dT = 0$. Taking the derivative with respect to temperature of $L_{op} = nL$, we have

$$\frac{dL_{op}}{dT} = n\frac{dL}{dT} + L\frac{dn}{dT}. \tag{3.7}$$

Since $dL/dT = 0$, we can write

$$\alpha = \frac{1}{L}\frac{dL_{op}}{dT} = \frac{dn}{dT}. \tag{3.8}$$

This results in

$$\Delta L_{op}(\Delta T) = \alpha L \Delta T. \tag{3.9}$$

Zumberge et al. (1988) empirically determined that $\alpha = 1.2 \times 10^{-5\circ} C^{-1}$. In the above expressions, ΔT is the change in temperature, and L is the original fiber length (measured at some reference temperature).

As a demonstration of temperature's effect on apparent length, we examine temperature variations in the Santa Barbara Basin, where we desired to deploy three FOSS cables of lengths 250, 500, and 750 m. Using a decades worth (1993-2002) of conductivity, temperature, and depth data (CTD) within the Basin, we bin temperatures in 20 m depth intervals. The mean and standard deviation of these bins is in Figure 3.1. We use the standard deviation as an average measure of reasonable, long period annual temperature fluctuations as a function of depth. This allows us to evaluate the theoretical temperature effect on optical fiber length for each cable. For cable lengths of 250, 500, and 750 meters, we expect 1-3 mm variation to occur in the fibers' lengths due to seasonal changes in temperatures. These results are in Figure 3.2. By simultaneously recording seabottom temperature, we can correct these apparent length changes to obtain the true physical length.

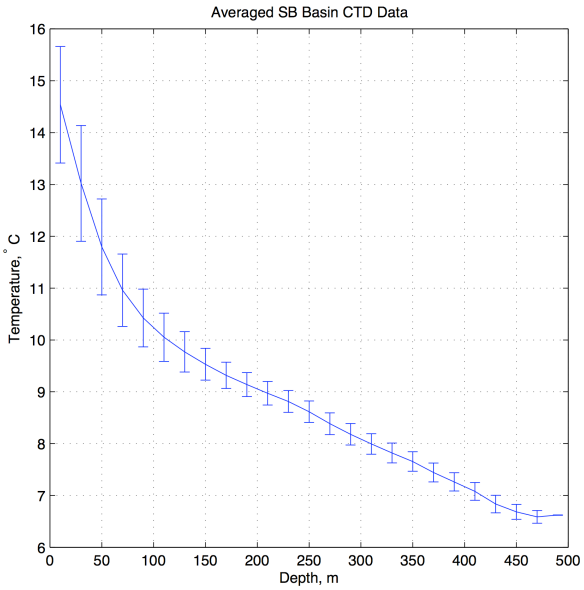

Figure 3.1: CTD data for the Santa Barbara Basin, from the Center for Coastal Studies at SIO. We placed temperature data in bins corresponding to 20 m depth and averaged the values. The standard deviation of temperature value in each bin is the uncertainty.

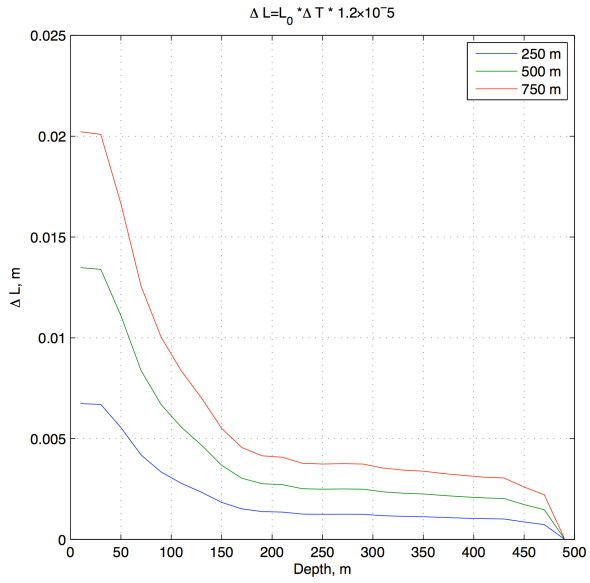

Figure 3.2: Theoretical optical length change due to temperature perturbations at depth in the Santa Barbara Basin.

3.4 Sensor components

3.4.1 Optical Fibers

Straining the fiber, as previously noted, will alter the refractive properties of the core and cladding. Recall that

$$\Delta L_{op} = \nu \Delta L,$$

where $\nu \approx 1.17$. We desired to experimentally verify this relationship for our choice of fiber and EDM. First, we stripped the polyeurethane away from the steel jacket and applied a nicropress crimp to the steel, before scoring the jacket and removing a section from the underlying fibers. We next we applied epoxy to the fibers as they exited the steel. We repeated this process for the other end of the cable.

Once the epoxy cured, we spliced temporary connectors to the ends of the fiber and attached ratchet straps to the crimps. We then stretched the fiber horizontally using the ratchet straps and recorded the applied tension, physical length change, and optical lengths using the EDM. This procedure resulted in an empirical value of $\nu = 1.1792$ (Figure 3.3.) One problem with this experiment was the horizontal stretching of the cable, as the cable itself possessed a non-negligible weight and formed a catenary in this orientation.

We took another section of cable and completely removed the fibers from the steel jacket. The weight per unit length of the fibers themselves is much less than the accompanying steel jacket and polyeurathene buffer. We wrapped a fiber around a circular post so that we had two equal lengths and applied epoxy to the fibers and a translation stage capable of 0.001 inch displacements. We then systematically deformed the fiber in 0.001 inch increments and measured the optical length using the EDM. Using this setup, we both stretched and relaxed the fibers to determine ν. Stretching produced $\nu = 1.1776$ and relaxation $\nu = 1.1811$ (Figure 3.4.) These experimental results verify the earlier relationship, and we can thus express physical length change as

$$\Delta L = \frac{\Delta L_{op}}{1.1776}. \tag{3.10}$$

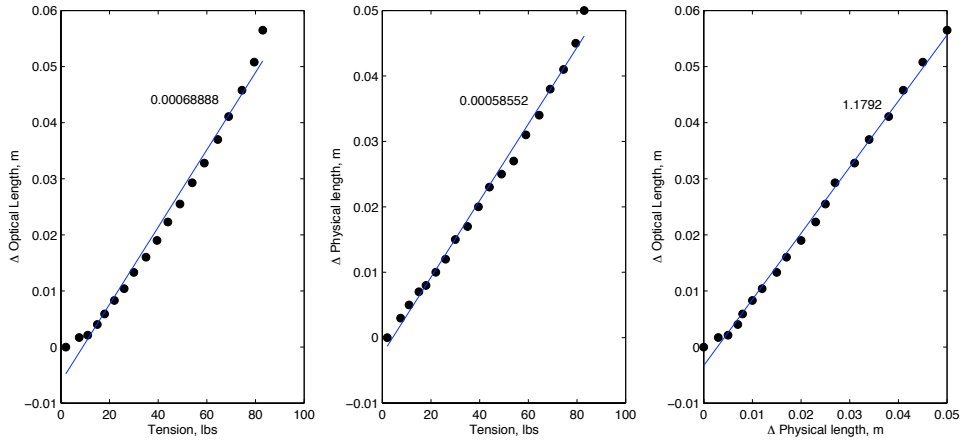

Figure 3.3: Results of tensioning an entire FOSS cable. There is a clear linear relationship between optical length change and physical length change; any observed optical length change can therefore be converted into physical length change and geophysical deformation on the seafloor

Similar experiments need not be performed on every cable, but they should be performed on each type of fiber from each vendor to ensure the correct coefficient will be used in a strain experiment.

3.4.2 Electronic Distance Meters

An electronic distance meter – or EDM – is a surveying tool used to measure distance between benchmarks. Most EDMs transmit an amplitude (or intensity) modulated optical beam. The beam reflects off some distant target and then returns to the EDM. The EDM takes the return signal and determines the relative phase of modulation in the returned light with respect to the incident beam. Essentially, the distance is calculated from the round trip travel time of the optical signal and the speed of light.

Although EDMs are designed for use in the atmosphere, through modification, they can be coupled to a fiber optic cable and can therefore measure the optical path length of the fiber (which can be converted to physical length via the above discussion.) The surveying market has driven the development of the EDM and as a result they are commercially available and typically possess high precision,

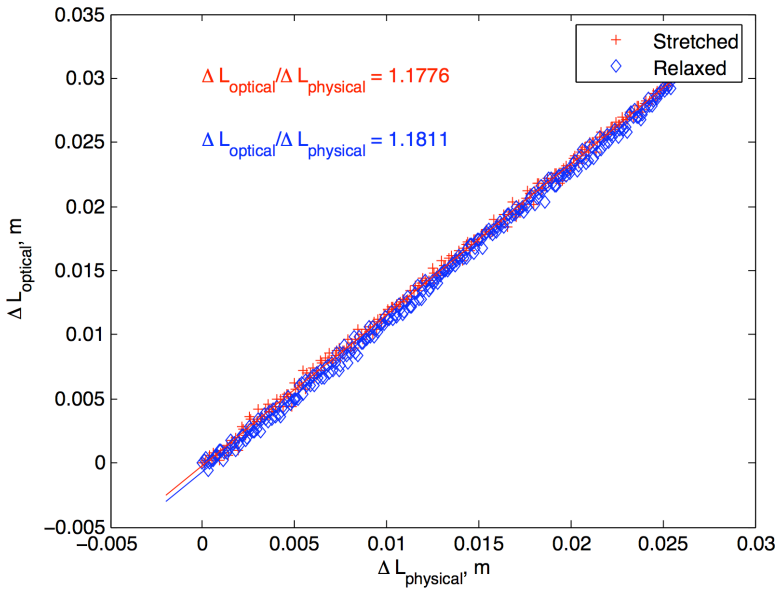

Figure 3.4: More systematic and accurate results for the relationship between physical and optical length change.

small size, and low power requirements (Rueger, 1990). In previous experiments, the Zumberge Gravity Lab used the WILD DI2002 EDM for seafloor and ice-sheet fiber strain measurements. The Wild DI2002 had a precision of 1-2 mm up to baselines of several kilometers.

Unfortunately, the DI2002 was discontinued by the manufacturer and we had to discover a comparable performing EDM. After examining several products, we chose an EDM from Dimetix instruments that operates in the visible spectrum, the DLS-A. The DLS-A has an accuracy of ± 1.5 mm (in air) and a precision of 0.1 mm. The laser diode is 620-690 nm (red) and is a class II ($<$0.95 mW) instrument. Commands and data can be transmit and received over an RS232 serial interface. The instrument can measure length, temperature, and signal strength of the return light (Dimetix, 2004).

Figure 3.5 shows how we coupled the output of the EDM to an optical fiber using a non-contact style laser-to-fiber coupler from OZ optics (with APC connectors.) The coupler has a small lens that focuses incoming light into the core of a fiber with an APC connecter. The return light similarly exits the same style

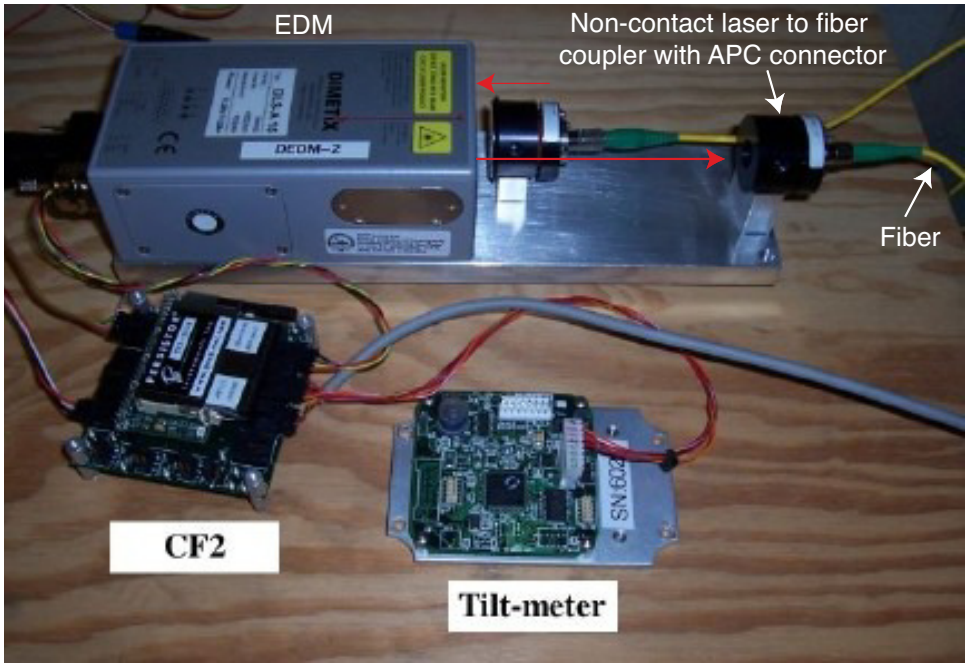

Figure 3.5: Electronic distance meter, CF2, and tiltmeter. Light from the EDM is coupled into the optical fibers using a non-contact style laser-to-fiber coupler and returned through a similar device.

coupler and is focused into the receiving optics of the EDM.

Diagnostics

There are some peculiarities to the Dimetix EDM that impact the overall system design and performance. These include how to optimize the return light, the effects of temperature, and the phase of the returning light.

For example, the instrument is sensitive to the signal strength of the returning light. Too high of an intensity, and the EDM generates an error; too little, and it cannot operate. Tests indicate that relative signal strength values of 1000-10000 mV are generally stable and produce repeatable length measurements. While the EDM will produce reliable length measurements for signal strength values higher than 10000 mV, the sensor saturates and produces errors with small perturbations in alignment once that region is reached. Signal strengths less than roughly 1000 mV (to a low of around 10-20) will produce length measurements, but the apparent

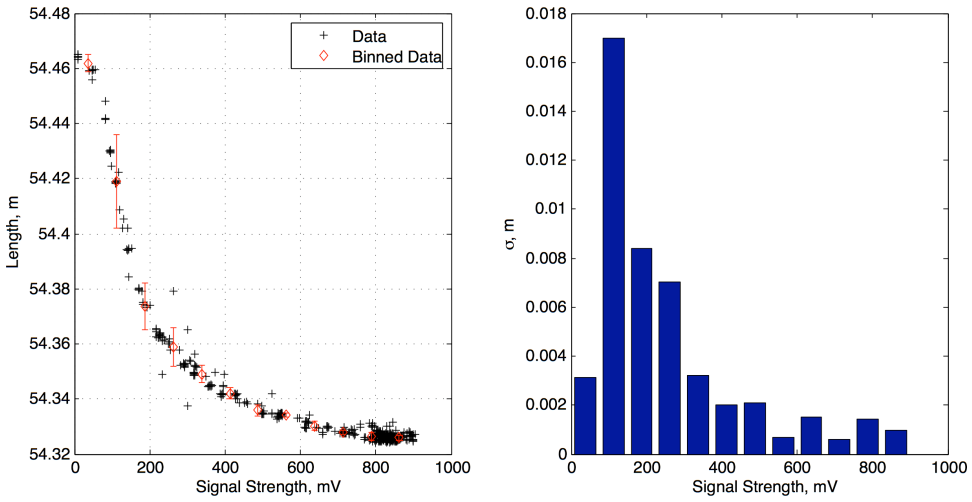

Figure 3.6: Varying the EDM signal strength results in a large variation in apparent length for signal strengths < 1000.

distances in this region have poor repeatability.

We demonstrate this effect in Figure 3.6 for signal strengths < 1000. We varied the signal strength by turning the adjustment screws on the return laser-fiber coupler, thereby de-tuning the optics. Signal strengths greater than 1000 mV produced RMS variations in length measurements of less than 2 mm, whereas a signal strength less than 1000 mV resulted in repeatability on the order of 4 mm to 1 cm. At first, we thought this might have something to do with the polarization of the outgoing EDM light being returned with a narrow focus. We attempted to use a polarizer to decrease the return signal strength, but polarizers possess a small "wedge angle" which slightly deflected the beam and prevented it from efficiently coupling light into the small diameter fiber core. The mounting design did not allow for the placement of the polarizer between the EDM and the return coupler.

Because both too much and too little light produces errors, it is important to tune the optics in such a way as to avoid these possibilities. First, we maximized the outgoing light coupled into the fiber by turning the adjustment screws until the light from the return fiber, which we attached to an external signal strength detector, was maximized. Next, we attached the return connector and tuned its optics until the EDM signal strength saturated at the highest value and produced

an enumerated error through its RS232 connection. We then removed one of the fiber connectors and coupled it to various inline attenuators with APC connectors (i.e., 2 dB, 5 dB, etc), which we then reconnected to the optical mounts. For each attenuator, we would retune the optics such that the return light was maximized. We repeated this process adding a different valued attenuator or a combination in series until the return light optics were optimized, but the signal strength was in a stable regime (typically 2000 - 8000 mV).

Another potential problem with the Dimetix EDM is a "wrapping" effect. Roughly every 250 m of physical length, the length measurement returns to zero (Figure 3.7.) The EDM uses phase modulation to determine time of flight delay and thus length, and when the phase reaches 360° it returns to zero, and therefore zero distance. For lengths greater than integer multiples of 250 m, the EDM does work, but the returned length measurements are only relative to something approximating $L_{\text{true}} \approx 250n + L_{\text{returned}}$, where n is an integer from 0, 1, 2, etc. Changes in length, however, are absolute, since $dn/dt = 0$. We can accurately observe strain, but in choosing the cable length for the seafloor, we must make sure that the initial length is not near the boundaries of this wrapping effect. We find empirically that 5-10 m greater and 50 m less is generally sufficient.

An additional test included examining the effect of temperature on the EDM. As noted, temperature changes the refractive properties of a fiber and therefore the optical length. The EDM electronics may also suffer a temperature effect. To explore this possibility, we surrounded the EDM with heater tape (attached to a timer) and enclosed both the EDM and tape in an insulated box. The EDM was connected to a fiber wrapped around a mandrel also in an enclosed, insulated box. A thermistor recorded the temperature of the mandrel which was subject only to room temperature fluctuations.

We recorded EDM temperature using its built in temperature sensor, along with the fiber length and fiber temperature over several forcing cycles. The results are displayed in Figure 3.8. We first correct the observed fiber length for fiber temperature using the earlier analysis, and then determine the relationship between the corrected fiber length and the EDM temperature. The results suggest

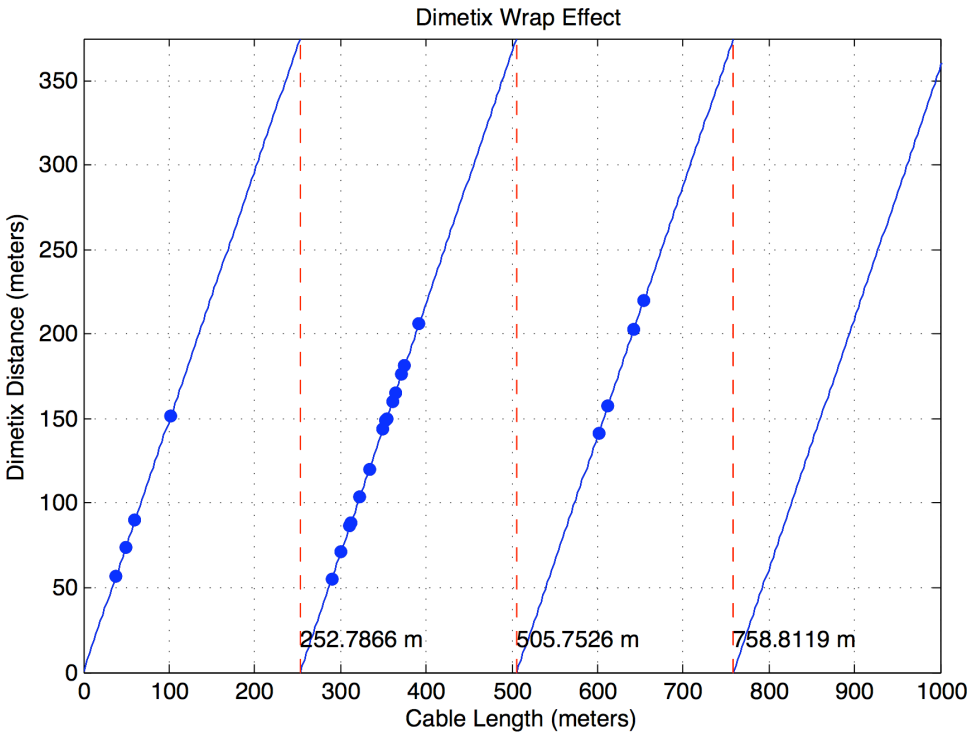

Figure 3.7: The Dimetix EDM has an interesting wrapping feature. Due to phase modulation approaching 360° and returning to zero, length measurements also return to zero around integer multiples of 250 m. Measured lengths for distances greater than 250 m are therefore relative, but length changes are absolute.

a linear relationship. We can then perform another correction to the observed fiber length to obtain the total corrected length (which removed both EDM and fiber thermal effects). The EDM-temperature correction coefficient is dependent on the fiber's actual physical length and will change from fiber to fiber, but the correction is straightforward as long as we have accurate indicators of fiber and EDM temperature and there are not physically induced length changes. It should be straightforward to apply similar corrections on the seafloor where temperature variations are significantly less and forcing occurs on the order of months as opposed to hours.

3.4.3 Computer Hardware

We desired a low power computer that will interrogate the EDM and store data. Our choice of a Persistor CF2, an off the shelf single board computer specifically designed for low power applications along with occupying a small volume, best fit our needs. The CF2 uses removable compactflash card with up to 4GB space for data storage. It measures only 2.5" by 2.0" by 0.7" in size, draws only $10\mu A$ of current in suspended mode and $250\mu A$ in online mode. Additionally, it attaches to stackable mating boards.

3.4.4 Communications

The CF2 persistor can theoretically record data as long as the flash card has available memory and the battery supplies sufficient power. Retrieving the data, however, requires a physical connection to the CF2, physically removing the flash card, or interrogating the persistor using an acoustic modem. We intended to use FOSS for geodetic monitoring for periods greater than one year and desired data retrieval at periods of several months to assess and respond to any deformation and to observe the instrument's reliability. Our best option was therefore an acoustic modem.

Computers process information represented in a digital format of 1's and 0's, corresponding to the presence or absence of an electronic signal. This flow of digital

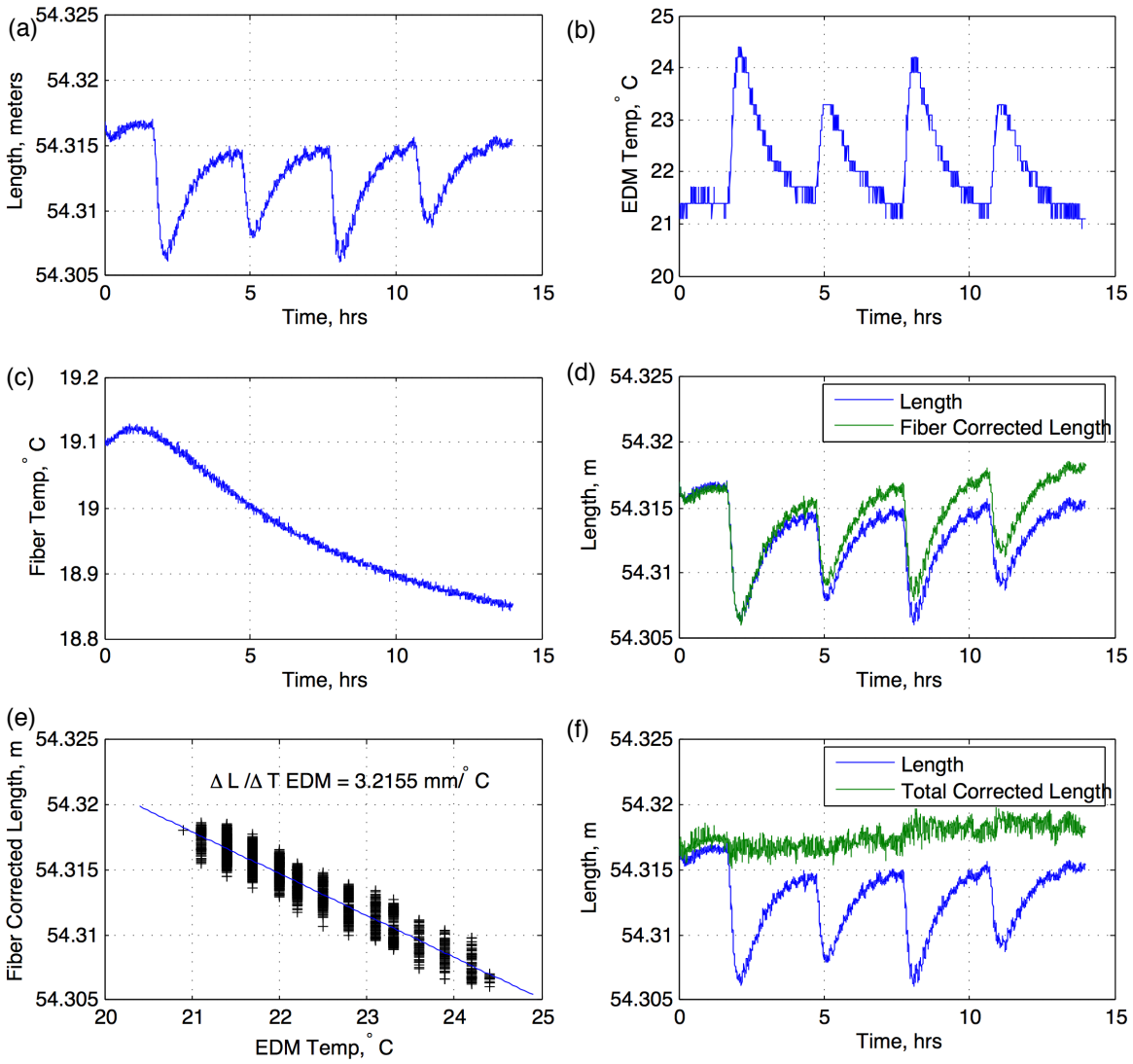

Figure 3.8: Results of an experiment to determine the affect of temperature on the EDM. The EDM was placed in an insulating box with a forced temperature and the fiber was isolated subject to room temperature. We recorded: (a) fiber length; (b) EDM temperature; and (c) fiber temperature. Corrections can be made for (d) fiber temperature effects so we can determine (e) the effect of temperature change on the EDM. (f) shows the total corrected length, accounting for both of these effects.

information, or telemetry, is converted into sound using a modem, which stands for modulation/demodulation. The modem modulates the digital signal of 0's and 1's into an analog format of different frequencies within a defined bandwidth. The frequency format can then be transmitted as electrical signals over telephone lines, a well defined microwave, or, in our example, acoustically through water.

Using water as an acoustic transmission medium is a significant departure from the benign medium of a shielded wire. Electrical signals transmitting on a phone line travel at the speed of light, whereas sound propagates through water at a speed of roughly 1500 meters per second. This distinction directly impacts the baud rate – the number of bits per second the modem can generate and receive – and the proximity in which signals can be sent and understood at the receiving end of transmission. Temperature and salinity changes in the ocean environment can also affect transmission. Signals deteriorate over distance. On land signals are strengthened at network facilities along a cable's path, but no such facilities exist in the ocean and the signal deteriorates over a shorter baseline, effectively requiring the receiver to be within a range of only a few kilometers depending on the frequencies transmitted.

More importantly, the ocean is an open channel vertically bounded on the bottom and surface, but essentially infinite in the other directions. Sources of noise contaminate the channel, some anthropogenic such as commercial activity or the operating research vessel. An open medium allows for multiple paths from the transmitter to the receiver. Acoustic reflections off the bottom, surface, or the hull of the ship: all are echoes that will partially arrive during the primary signals reception. These multipath signals must be removed from the incident signal to ensure proper interpretation. We chose a commercial acoustic telemetry modem from Teledyne Benthos, a company specializing in subsea acoustics and applications.

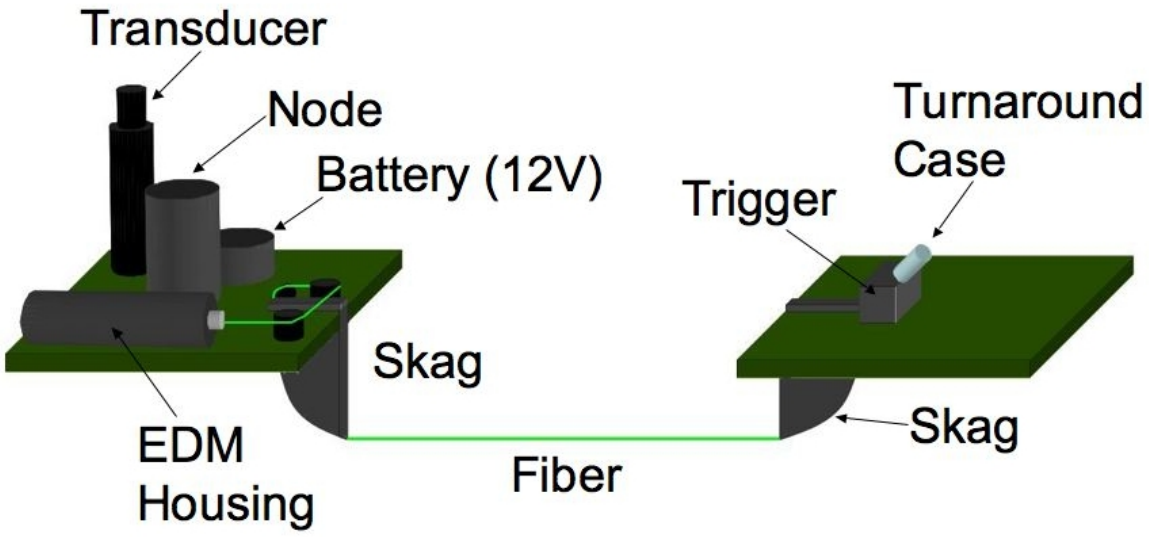

Figure 3.9: FOSS components. A fiber is stretched between two anchors. Attached to the rear anchor are the Node (Node components shown in Figure 3.13), EDM, modem transducer, and battery. The front anchor hosts the turnaround pressure case, where the fiber is spliced together (Figure 3.10).

3.5 Assembly of components

FOSS monitors the length of a fiber stretched between two anchors. Figure 3.9 shows an illustrative layout of the components. Attached to the one anchor (known as the front anchor) is a small stainless steel pressure case (turnaround case). The fiber enters the pressure case through a bulkhead penetrator. Figure 3.10 shows how the fiber enters the bulkhead penetrator which is screwed into the pressure case. The cable is threaded through the penetrator. The polyeurethane buffer is then removed and a compression sleeve is crimped onto the steel jacket so that the cable cannot be pulled backwards out of the penetrator. The forward exposed part of the steel jacket is also removed exposing the two fibers. We then stripped an $\approx 1/4$ inch section of the fibers that were within the penetrator cavity of the 250 m acrylate buffer to expose the bare glass fiber. The entire cavity of the penetrator was then filled with epoxy capable of withstanding the expected ocean bottom pressures to seal the entire cable from seawater penetration. The remote ends of the buffered fibers were then spliced together to form the continuous loop.

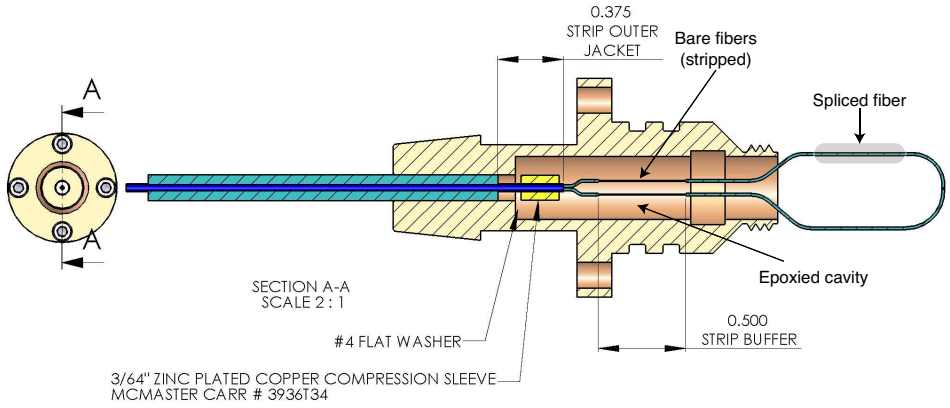

Figure 3.10: The remote end of the fiber is epoxied to a penetrator and the two fibers within the stainless steel jacket are spliced together. The spliced fiber is then put into a small stainless steel pressure case, known as the turnaround case, and the penetrator is screwed onto its end.

Mounted on the other anchor (rear anchor) are pressure cases containing the optical components, logging system and acoustic modem board, modem transducer, and battery. The EDM is housed in an anondized aluminum pressure case capable of withstanding 3000 m depth (Figure 3.11.) The fiber enters the pressure case using a similar bulkhead penetrator and epoxy method as the remote stainless steel case. The CF2, modem board (and battery), and tilt sensor are housed in another pressure case (Figure 3.12) called the node. An underwater cable runs from the EDM pressure housing to the node, and the node has additional cables going to the modem transducer and battery pack. How the components are connected is shown as a block diagram in Figure 3.13.

3.6 Geotechnical considerations

In Chapter 2, we presented results from an earlier seafloor strainmeter deployed off of La Jolla, California. In that experiment, the cable was deposited on top of the seafloor sediments in an area with no expected motion or other influences such as fishing activity. To use this sensor in a location such as the Santa Barbara

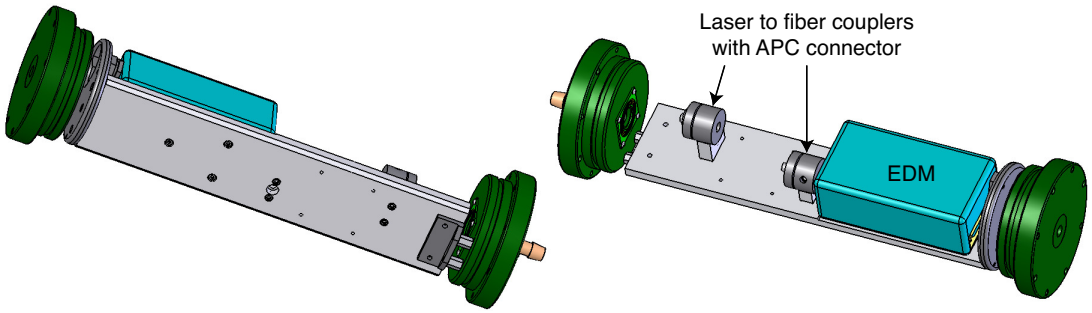

Figure 3.11: Interior of the pressure case housing the EDM. A commercial EDM is mounted to a plate specifically designed to couple its light into a laser-fiber coupler within a pressure case. O-ring lined endcaps are fixed to the ends of the plate, and the entire fixture is embedded in a cylindrical pressure case. Connectors penetrate the endcaps for the optical fiber, data, and power

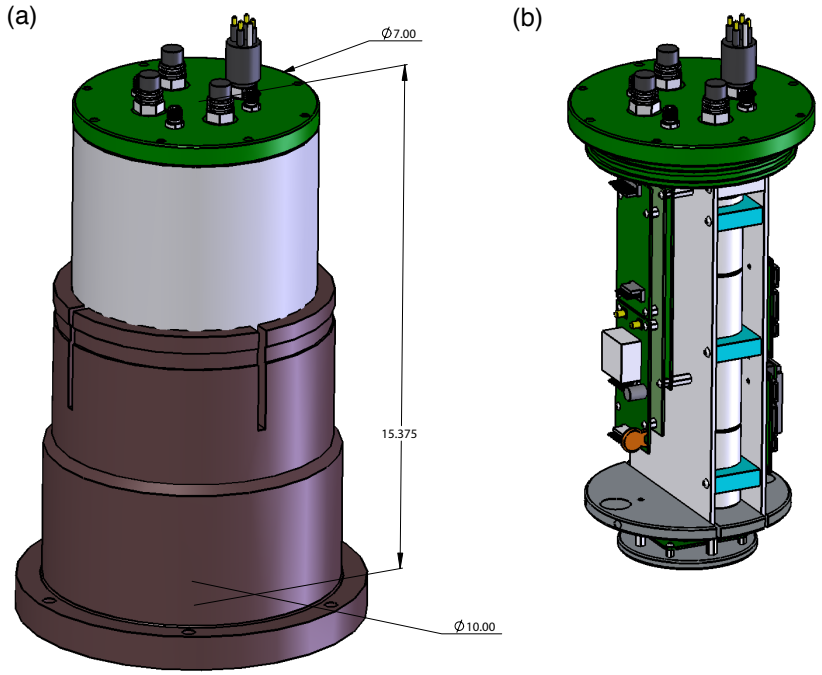

Figure 3.12: (a) Pressure case (and mount to the seafloor anchor) of the Node. Penetrating connectors breach the end cap, connecting the EDM case, battery, and modem transducer. (b) The interior of the Node houses the modem board, CF2-persistor, auxiliary sensor board, and tilt sensor.

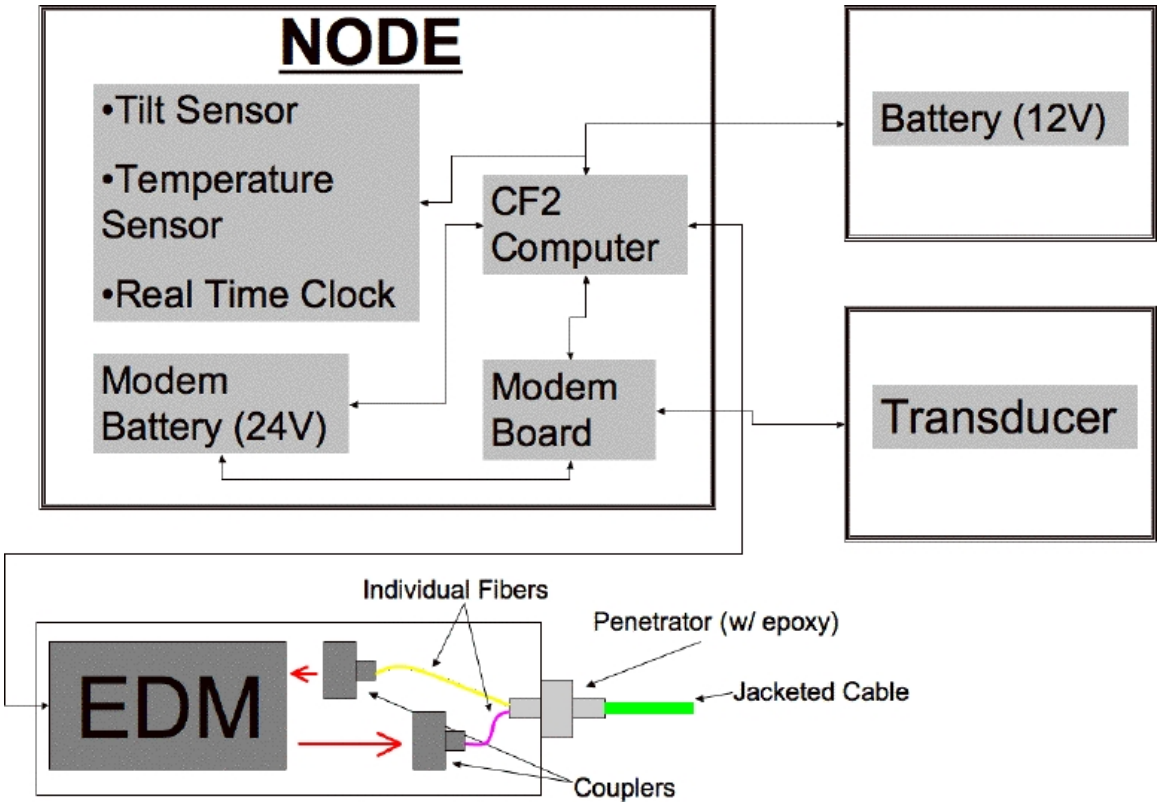

Figure 3.13: Flow chart showing how the components on the front anchor (Figure 3.9) are connected.

Basin, further work is required to protect the cable from damage and degradation such as wildlife and fish trawling and to insulate it from water column temperature changes. To mitigating these risks, we proposed to bury the cable.

Communications companies and oil and gas companies have buried seafloor cables for many years, but at extraordinary expense. Burial is often performed using the capabilities of a commercial remotely operated vehicle (ROV.) An appropriate ROV could quite easily bury our cable in the sediment and at first glance would seem like the logical choice, but there are limits to this approach (geotechnical, and possibly financial given the additional expense of operating an ROV.)

An important geotechnical consideration is the cable's trajectory. A curved, tensioned table between two stable, anchored ends would tend to straighten if it were able to move through sediment with low resistance. In doing so, this would contaminate length measurements with an apparent, but not real, change in length. Changes in distance between the two anchors are inferred from changes in the optical path length of the cable; this inference is flawed if the cable path is time variable. This effect may be responsible, for example, for the 8 mm exponential relaxation witnessed in Figure 2.10. In order to abate this problem when burying a cable, care must be made to limit the amplitude and wavelengths of any curves in the cable's path based on the resistive properties of the sediment.

To explore this complication, we define a coordinate system where the x-axis is defined by the line between the two end anchors. That cable's trajectory is then described by a shape function $y(x)$, where y is the displacement of the cable from the x-axis. Following the derivation for the wave equation on a string under tension T (see, e.g. Stein and Wysession, 2003), the perpendicular force per unit length $f_\perp$ on the cable at position x is given as

$$f_\perp(x) = T\frac{\partial^2 y}{\partial x^2}. \tag{3.11}$$

For a given tension in the cable, we desired $f_\perp$ to be everywhere less than some critical value f_c that is a characteristic of the sediment and the diameter of the cable.

We determined f_c experimentally. We designed a laboratory apparatus that measured the resistant force on a rod having the same diameter as the fiber cable

as it was forced laterally through sediment samples collected from our intended deployment site offshore Santa Barbara, California (Chapter 5.) Figure 3.14 shows photographs of this apparatus. We placed a 4-mm-diameter rod in the sediment and attached it to an overhead camshaft. Small weights applied a rotation to the camshaft and we observed how much weight was required for the rod to begin moving laterally through the sediment. We discovered a force per unit length of 11.4 N/m (2.57 lb/m) was required to initiate creeping of the rod through the sediment.

To examine the effect this critical force on the buried cable path, we consider an initial sinusoidal trajectory with amplitude A and wavelength λ:

$$y(x) = A \sin\left(\frac{2\pi}{\lambda}\right). \tag{3.12}$$

The maximum force per unit length on such a cable is

$$f_{\perp}^{max} = TA\left(\frac{2\pi}{\lambda}\right)^2. \tag{3.13}$$

The requirement that $f_{\perp} < f_c$ everywhere results in a critical contour given as

$$A < \frac{f_c \lambda^2}{4\pi^2 T}. \tag{3.14}$$

This critical contour is displayed in Figure 3.15 for values of $f_c = 11.4$ N/m (2.57 lb/m) and $T = 89$ N (20 pounds). This result indicates, for example, that a cable possessing curves with an amplitude of 2 m and a wavelength of 30 m is stable, but it will creep through the sediment causing apparent strains if the wavelength is only 20 m.

These results suggest that burying the cable to the specifications required to accurately sense strain is non-trivial. Any chosen method of deployment must lay the cable with sufficient straightness. An ROV may or may not be capable of delivering these specifications given problems such as maneuverability when other systems are engaged in power, or deep water currents or other issues that could affect laying the cable's path. To abate these issues, we designed a sled that could be towed across the seafloor to remotely deploy the anchors and bury the fiber.

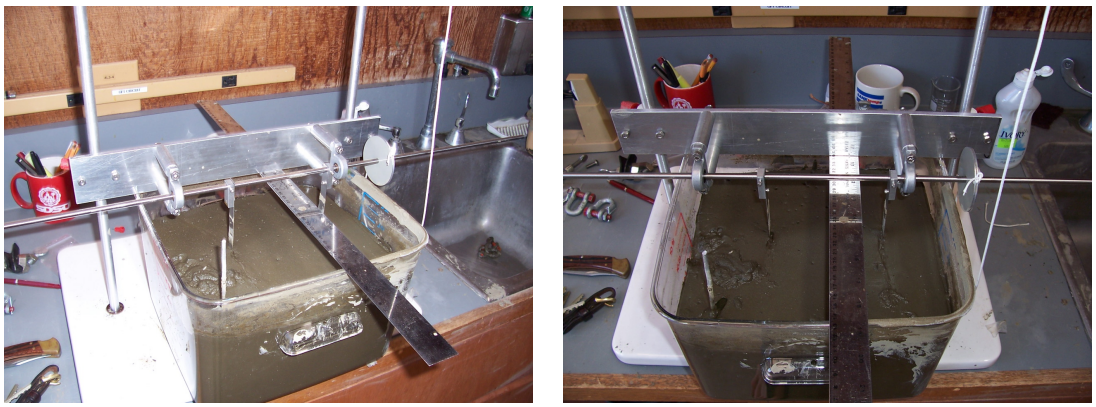

(a) (b)

Figure 3.14: Subfigures (a) and (b) are photographs of the laboratory apparatus we designed to measure the critical resistive force per unit length of sediment on a 4-mm-diameter cable. A 4-mm-diameter rod was place in sediment from the Santa Barbara basin and attached to an overhead camshaft. Small weights applied a rotation to the camshaft and we observed how much weight was required for the rod to begin moving laterally through the sediment.

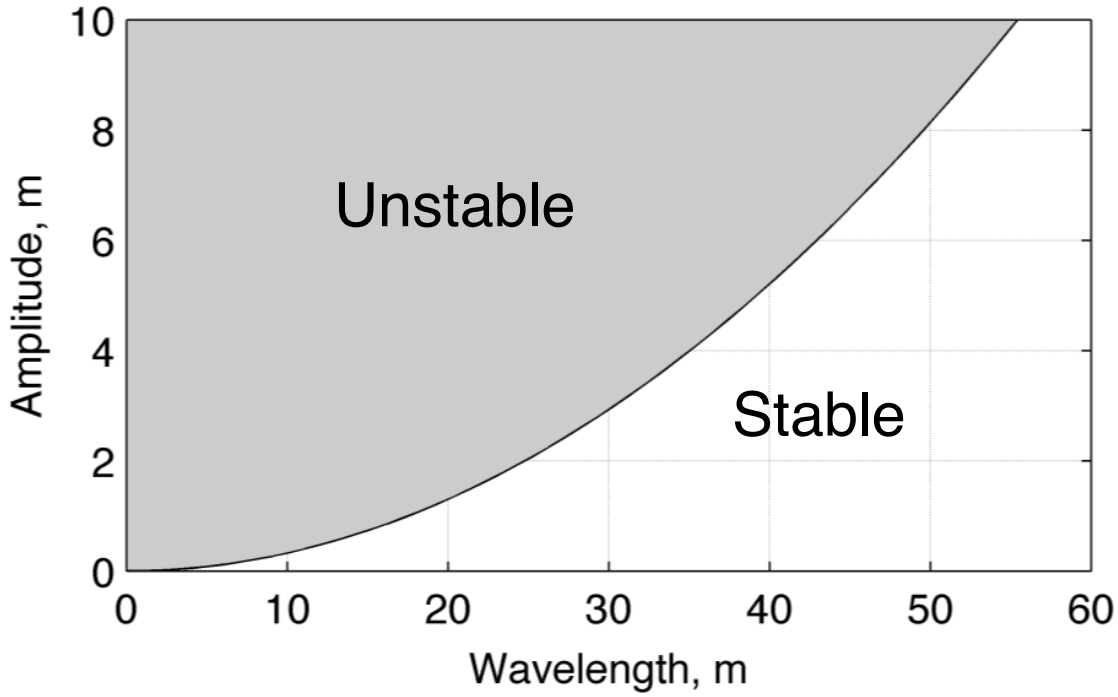

Figure 3.15: Amplitudes of the fiber path undulations that fall in the shaded region are too large and might causes the optical fiber cable to undergo creep. The boundary is $A = (f_c\lambda^2)/(4\pi^2 T)$, with $f_c = 11.4$ N/m and $T = 89$ N.

3.7 Deployment using a towed sled

In water depths exceeding a few hundred meters, the path of the sled on the seafloor is a filtered version of the ship's track. Ship motions such as heave are attenuated, and a straight path is achievable at long wavelengths. All components of the strain sensor initially ride along with the sled, which is displayed in Figure 3.16. Shoulder bolts and retractable pins hold two anchors (115 kg steel plates) to the bottom of the sled. The rear anchor holds the electronics, optics, batteries, and acoustic modem. The fiber cable is routed from a pressure case containing the EDM and optics through a curved skag at the front of the rear anchor that positions it 16 cm beneath the seafloor. The fiber continues to a similarly shaped skag on the front anchor, curves back to the anchor surface, and passes through a spring-loaded trigger to a spool that is attached to the front of the sled.

When the sled, under way on the seafloor, arrives at one endpoint of the targeted strain site, a command from the ship releases the rear anchor. The sled continues on its forward path leaving the rear anchor at the point of release due to friction between the anchor and the ocean bottom. The fiber cable is then pulled off the spool (a magnetic brake applies $\approx$ 20 lbs of back-tension on the cable) and the fiber is laid in a furrow carved by the skag on the forward anchor.

At the spool end of the fiber cable, there is a small pressure case that houses the splice to form an optical round trip between the two fibers in the cable. As this pressure case comes off the spool, it enters the trigger on the forward anchor and activates a spring-loaded mechanism releasing the front anchor (Figure 3.16D), leaving the fiber tensioned over its length between the two anchors at a depth of 16 cm below the sediment surface.

We conducted extensive tests of the anchor releases and fiber deployment on land – first on a beach – and then, in order to mimic the seafloor, we constructed a 40 foot long trough and filled it with a mixture of beach sand and bentonite clay (Figure 3.17.) In a half-dozen tests, both anchors disengaged from the sled as designed and we observed no problems.

The fiber remained buried in the trough of sand and mud for a period of four weeks where we monitored its length (Figure 3.18.) Removing the trend due

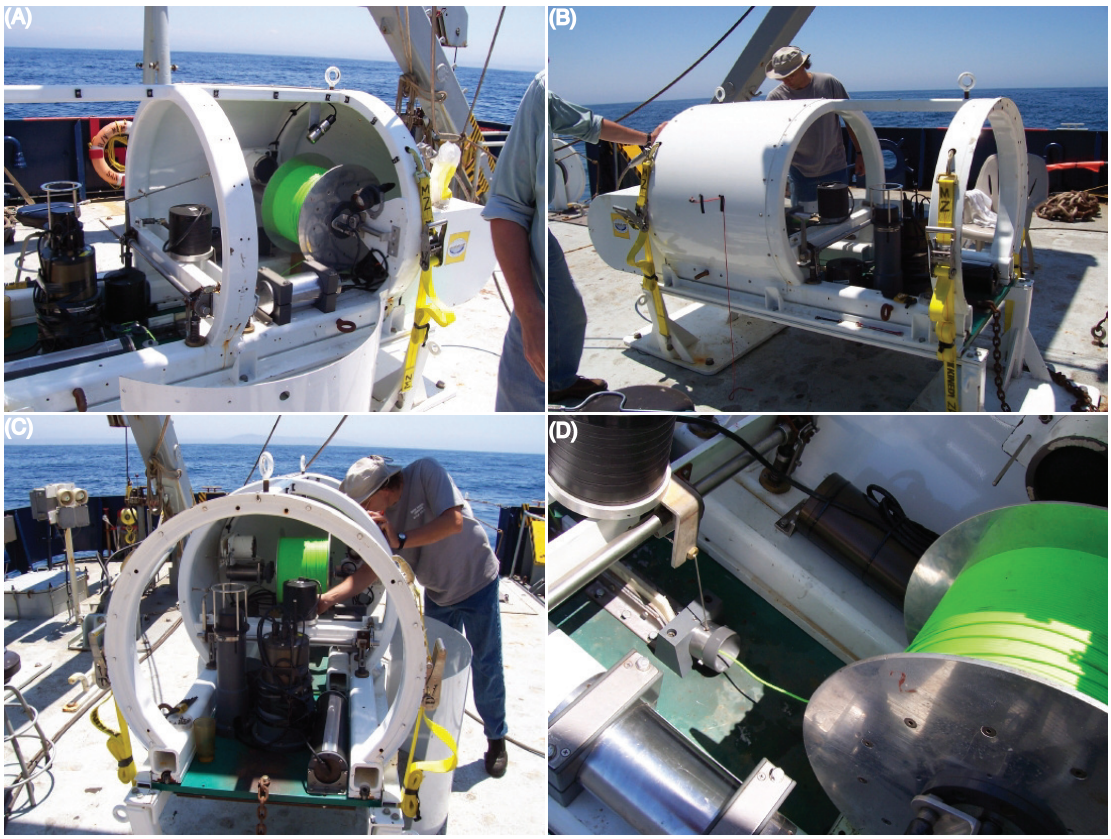

Figure 3.16: Photographs of the sled. (A): sideview showing the front of the, the spool, and the fiber. (B): sideview showing the entire length of the sled and the rear anchor components. (C): view from the rear, showing the rear anchor and the acoustic modem, node containing the computer and modem board, and pressure case containing the electronic distance meter and optics. (D): close-up of the front anchor release and spool.

to temperature, the RMS variability is ≈ 1 mm. As a conservative estimate, we therefore believe we can confidently observe changes in length to less than 1.5 mm (which is the specification for measurements in the atmosphere.) We tested this by attaching hydraulic jacks to one of the anchors and physically displacing it a known distance. The fiber must displace an equal amount, which we confirmed using the EDM.

The motivation for this sensor was to lay the cable across a seafloor crack that might represent an actively forming future headscarp of a submarine landslide in the Santa Barbara Basin. This crack is located between two hazardous landslide complexes. Details of that study area are in Chapter 5. One hypothesis was that the crack was the result of downslope creep of sediments. The FOSS sensor was designed to monitor creep across the crack over a period of three years.

We embarked to the Santa Barbara Basin in November 2006 on the dynamically positioned ship, the R/V Roger Revelle. We equipped the sled with an inertial navigation system measuring heave, pitch, roll, and three component accelerations. A magnetic rotation sensor counted the revolutions of the spool to indicate when the rear anchor released, which we issued by an electric command. We also included a video camera positioned to watch the anchors release and spool rotate. The sled, however, significantly disturbed the sediments when under way, making it difficult to diagnosis the release mechanisms. We therefore included a second magnetic proximity sensor on the front anchor as an additional indicator of release.

In spite of previous successful tests on the beach and in the mud pit, we were unsuccessful in several attempts at deploying the sensor with this sled. We diagnosed all failures as due to the anchor release mechanisms becoming delayed from forces on the anchors larger than encountered in our tests. When the front anchor delays in its release, the result is a broken fiber cable because the forward anchor continues to move with the sled.

We observed this in our final deployment. Using the dynamic positioning capability of the ship, we repositioned the sled at 5 m increments and then maintained position, allowing the sediments to clear and to permit observations of the

Figure 3.17: Mudpit where we tested the sled. Shown is the rear anchor (foreground), the front anchor (background), and the path of the sled including the trenched fiber.

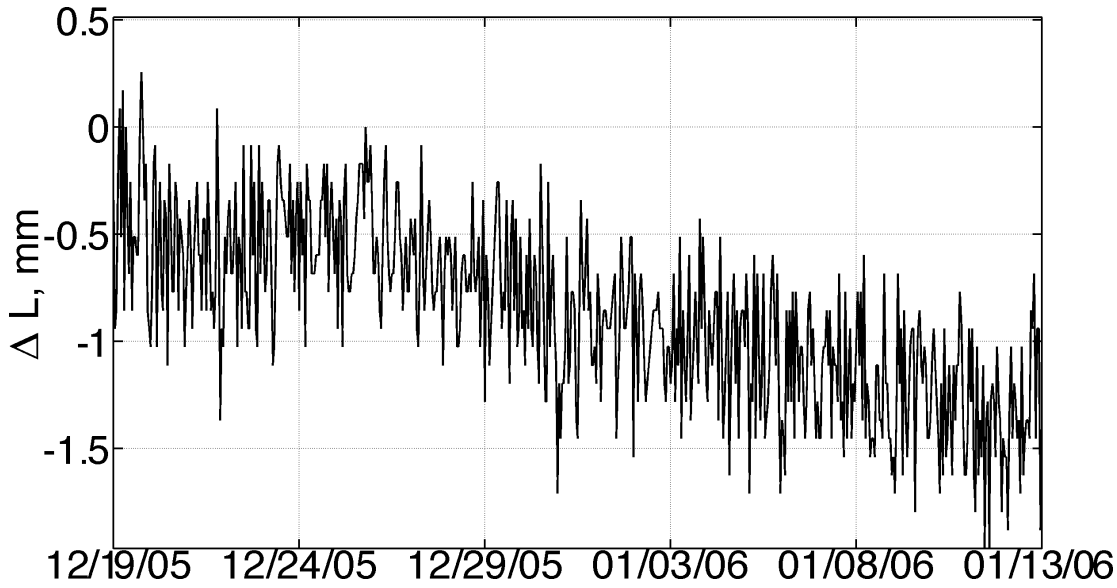

Figure 3.18: Four week fiber record in the mudpit. The RMS variability is ≈ 1 mm.

spool and anchors. The failure was recorded on video. It appeared that the front anchor would delay from its release when the pressure case engaged the spring loaded trigger. During a previous deployment attempt, the front anchor returned with the sled and the fiber was broken at the beginning of the plate. We suspect that the slight delay in anchor released caused the tension to build beyond the failure limit of the steel jacket. We have developed plans to correct this problem in the future and several working sensors remain in our lab.

3.8 Conclusions

We have developed a fiber optic seafloor strainmeter that is capable of measuring displacement of an optical fiber between two points anchored to the Earth to less than 1.5 mm. The system can remain on the seafloor for a period of years if the data is periodically offloaded using an acoustic modem. Burying the fiber is desirable and feasible via a towed sled. Due to the particulars of our mechanical release systems, however, our sled was unable to deploy a working instrument.

Despite our inability to deploy a working instrument on the ocean bottom, the potential for this type of instrument remains great. Several working sensors remain in our laboratory and we hope to revisit deployment in the future. Given our experiences, we recommend the assistance of an ROV in conjunction with the towed sled to ensure deployment of a working sensor.

3.9 Acknowledgements

Numerous individuals contributed to these engineering efforts, including G. Austin, D. Rimmington, D. Price, R. Zimmerman, G. Openshaw, P. Jeanjean, D. Chadwell, the captains and crews of the R/V Roger Revelle, R/V Gordon Sproul, and the R/V New Horizon, as well as the MPL machine shop.

Portions of this work covering the geotechnical considerations, the mudpit, and deployment were previously published in: **Blum, J., Nooner, S., and Zumberge, M., 2008: Recording Earth strain with optical fibers. *IEEE Sensors Journal*, 8(7), 1152-1160.** The author's contribution to this study was to write published portions of the manuscript, as well as the design, development, and deployment of the fiber optic seafloor strainmeter. The author conducted all of the engineering tests in this chapter. Design of the sled is attributed to Gary Austin and individuals at the Marine Physical Laboratory. The author assisted in testing all mechanical components of the sled and its assembly. Construction of the mudpit was done by the author in conjunction with Gary Austin and Matt Norenberg; the author designed and conducted all sediment tests to examine fiber stability.

REFERENCES

Bertholds, A., and Dändliker, R., 1988: Determination of the individual strain-optic coefficients in single-mode optical fibers. *Journal of Lightwave Technology*, **6**(1), 17–20.

Blewitt, G., Heflin, M., Webb, F., Lindqwister, U., and Malla, R., 1992: Global coordinates with centimeter accuracy in the international terrestrial reference frame using GPS. *Geophysical Research Letters*, **19**, 853–856.

Butter, C., and Hocker, G., 1978: Fiber optics strain gauge. *Applied Optics*, **17**(18), 2867–2869.

Chadwick, W., Milburn, H., and Embley, R., 1995: Acoustic extensometer: measuring mid-ocean spreading. *Sea Technology*, 33–38.

Dimetix, 2004: *Distance Laser Sensor DLS-A 15 Technical Reference Manual*. Dimetix AG, Switzerland, 1.06 edition.

Hocker, G., 1979: Fiber-optic sensing of pressure and temperature. *Applied Optics*, **18**(9), 1445–1448.

Langbein, J., 1989: Deformation of the Long Valley Caldera, eastern California from mid-1983 to mid-1988. *Geophysical Research*, **94**, 3833–3849.

Rees, W., 2001: *Physical Principles of Remote Sensing*. Cambridge University Press.

Rueger, J., 1990: *Electronic Distance Measurement*. Springer-Verlag, Berlin, 3 edition.

Spiess, F., Chadwell, C., Hildebrand, J., Young, L., Purcell, G., and Dragert, H., 1998: Precise GPS/Acoustic positioning of seafloor reference points for tectonic studies. *Physics of the Earth and Planetary Interiors*, **108**, 101–112.

Stein, S., and Wysession, M., 2003: *An introduction to seismology, earthquakes, and Earth structure*. Blackwell, Oxford, U.K.

Wyatt, F., Agnew, D., and Gladwin, M., 1994: Continuous measurements of crustal deformation for the 1992 Landers earthquake sequence. *Bulletin of the Seismological Society of America*, **84**, 768–779.

Zumberge, M., Elsberg, D., Harrison, W., Husmann, E., Morack, J., Pettit, E., and Waddington, E., 2002: Measurement of vertical strain and velocity at siple dome, antartica, with optical sensors. *Journal of Glaciology*, **48**(161), 217–225.

Zumberge, M., and Wyatt, F., 1998: Optical fiber interferometers for referencing surface benchmarks to depth. *Pure and Applied Geophysics*, **152**, 221–246.

Zumberge, M., Wyatt, F., Yu, D., and Hanada, H., 1988: Optical fibers for measurement of Earth strain. *Applied Optics*, **27**(19), 4131–4138.

Chapter 4

Observations of local phase velocity and earthquake induced deformation at the SAFOD borehole, California

4.1 Abstract

We present observations from a vertical, optical fiber interferometric strainmeter in the SAFOD borehole near Parkfield, California. The sensor detects both teleseismic earthquakes and local events, along with coseismic strain-steps consistent with theoretical dislocation models. For teleseismic events, we investigate the possibility of determining local Rayleigh wave phase velocities beneath the borehole by comparing the ratio of vertical ground acceleration from a nearby seismometer to vertical strain. While similar studies have used horizontal components and rotations, this is the first such attempt utilizing vertical measurements. We show that at periods from around 16 to 40 seconds, we can recover general dispersion characteristics that are within a few percent of models of realistic local structure.

4.2 Introduction

The San Andreas Fault Zone is the predominant fault zone accommodating motion between the Pacific and North American plates. Near Parkfield, in central California (Figure 4.1), the fault undergoes a transition. At Parkfield and continuing to the Northwest, the fault exhibits creep – averaging 25-30 mm/yr of right-lateral slip (Burford and Harsh, 1980; Lisowski and Prescott, 1981; Titus et al., 2005) – whereas southeast of Parkfield, the fault is locked, last rupturing in the M7.9 Fort Tejon earthquake in 1857 (Sieh, 1978). Parkfield itself has witnessed ruptures of similar size ($\approx M6$) and location in 1881, 1901, 1922, 1934, and 1966 (Bakun and McEvilly, 1984). The characteristics and frequency of these events led to a prediction that the next event would occur between 1985 and 1993, initiating the development of the Parkfield Prediction Experiment (Bakun and Lindh, 1985), an attempt to highly arm the region with geophysical instruments to observe the inter-seismic period leading up to the earthquake, the event itself, and the post-seismic response. The next earthquake in the sequence did not actually occur until 28 September, 2004 (Langbein et al., 2005). While the earthquake differed in both character and date of the 1985 prediction (Jackson and Kagan, 2006), the long-term experiment illuminated never-before-seen facets of the earthquake processes and directions for future earthquake monitoring and warning systems (Bakun et al., 2005).

In addition to the recurrent magnitude 6 earthquakes, Parkfield also exhibits frequent microearthquakes (around magnitude 2 or less), recurrent in size and location (Nadeau et al., 1994, 1995). Larger events that exhibit this recursive behavior are commonly referred to as characteristic earthquakes (Schwartz and Coppersmith, 1984). Determining the drivers of these characteristic events and their appropriateness as models for earthquake forecasting and hazard mitigation remains elusive, but ultimately critical (Kagan, 1993; McCloskey and Bean, 1994; Grandori et al., 2008). At Parkfield, the hypocenters of the characteristic microearthquakes were distributed in a sparse number of clusters. This clustering suggested that Parkfield would be an ideal location for deep drilling and in situ fault-zone measurements (Hickman et al., 1994; Nadeau and McEvilly, 1997).

The SAFOD project – or San Andreas Fault Observatory at Depth – began in 2002 to augment the earlier Parkfield Prediction Experiment and to investigate the physical and chemical processes and properties responsible for earthquake generation and crustal deformation near Parkfield. SAFOD was designed to actively drill down and across the fault trace at seismogenic depth. Through rock and fluid samples and down-hole instruments, the goals were to examine the composition and constitutive laws of materials within the fault zone; to monitor propagation of stresses initiating earthquakes and directing their rupture; to explore the roles of chemical reactions in the presence of hot, high pore fluid pressures on fault strength and earthquake frequency; and to observe changes in stress and strain from near field microearthquakes. The SAFOD borehole was placed about 1.8 km southwest of the San Andreas fault trace and slightly northwest of the $M6$, 1966 Parkfield earthquake (Hickman et al., 2004).

The first component of the SAFOD project was a pilot hole study conducted to a depth of 2.2 km before the primary borehole and equipment were installed. Using a 3-component seismic array installed within the pilot hole, Imanishi and Ellsworth (2006) discovered that the static stress drops and apparent stresses of the nearby microearthquakes suggested moment-independent scaling, similar to the scaling laws expected for moderate and large earthquakes. This result suggested that the properties and processes governing the microearthquakes may be macroscopically similar to those of larger tectonic earthquakes. Thus, observations of preseismic and postseismic responses to earthquakes with magnitudes 2 or less – which occur frequently along the Parkfield – may reveal what physical behavior emerges onset to the more sparse, magnitude 6 events.

In Chapter 2, we described the development of an optical fiber, interferometric strainmeter that we installed outside the well casing of the upper one kilometer, vertical portion of the SAFOD borehole (see also, Blum et al., 2008). In this chapter, we present greater details and results from that instrument. Our goals are to observe strain before, during, and after earthquakes in the region to explore the behavior driving and accompanying the earthquake cycle. While the long awaited 28 September 2004 event occurred shortly prior to our installation,

we are able to observe ground motions from local microearthquakes and teleseismic events. This chapter describes the functionality and benefits of our sensor, presents results of local deformation, and investigates the possibility of determining local Rayleigh wave phase velocities by comparing collocated measurements of vertical strain and acceleration.

4.3 Description of the Instrument

4.3.1 Design

Optical fiber strain sensors have been developed to measure a variety of geophysical process, including the flow of glacial ice (Zumberge et al., 2002), seafloor deformation (Zumberge, 1997; Blum et al., 2008), and atmospheric pressure signals (Zumberge et al., 2003). Chapter 2 and Blum et al. (2008) describe two ways to interrogate optical fibers: with an electronic distance meter, or utilizing interferometry. Optical fiber interferometers can measure picometer displacements of the fiber; Zumberge and Wyatt (1998) have used this technique to monitor displacements of end monuments of longer baseline strainmeters and tiltmeters in shallow boreholes. Interferometric methods have an advantage in that they can be sampled at intervals and dynamic ranges equivalent to conventional seismometers [using a similar interferometric technique, an optical fiber seismometer can rival the performance of observatory class seismometers (Otero, 2009; Zumberge et al., 2010)]. A borehole sensor of this type can therefore be treated similar to a broadband seismometer at short periods but can also capture long period strain.

Installation details of the optical fiber, interferometric strainmeter are in Chapter 2 and Blum et al. (2008). The instrument consists of a single mode optical fiber stretched vertically along the outside of several hundred meters of borehole casing cemented into the Earth. The fiber, slightly elongated during installation, and fixed to the casing at its upper and lower ends, elastically complies with Earth strain. We monitor the strain-induced length change interferometrically. Figure 4.2 is a schematic illustration of the installation. Several optical fiber cables were installed from October 2-3, 2004, however only two survived due to an unexpected

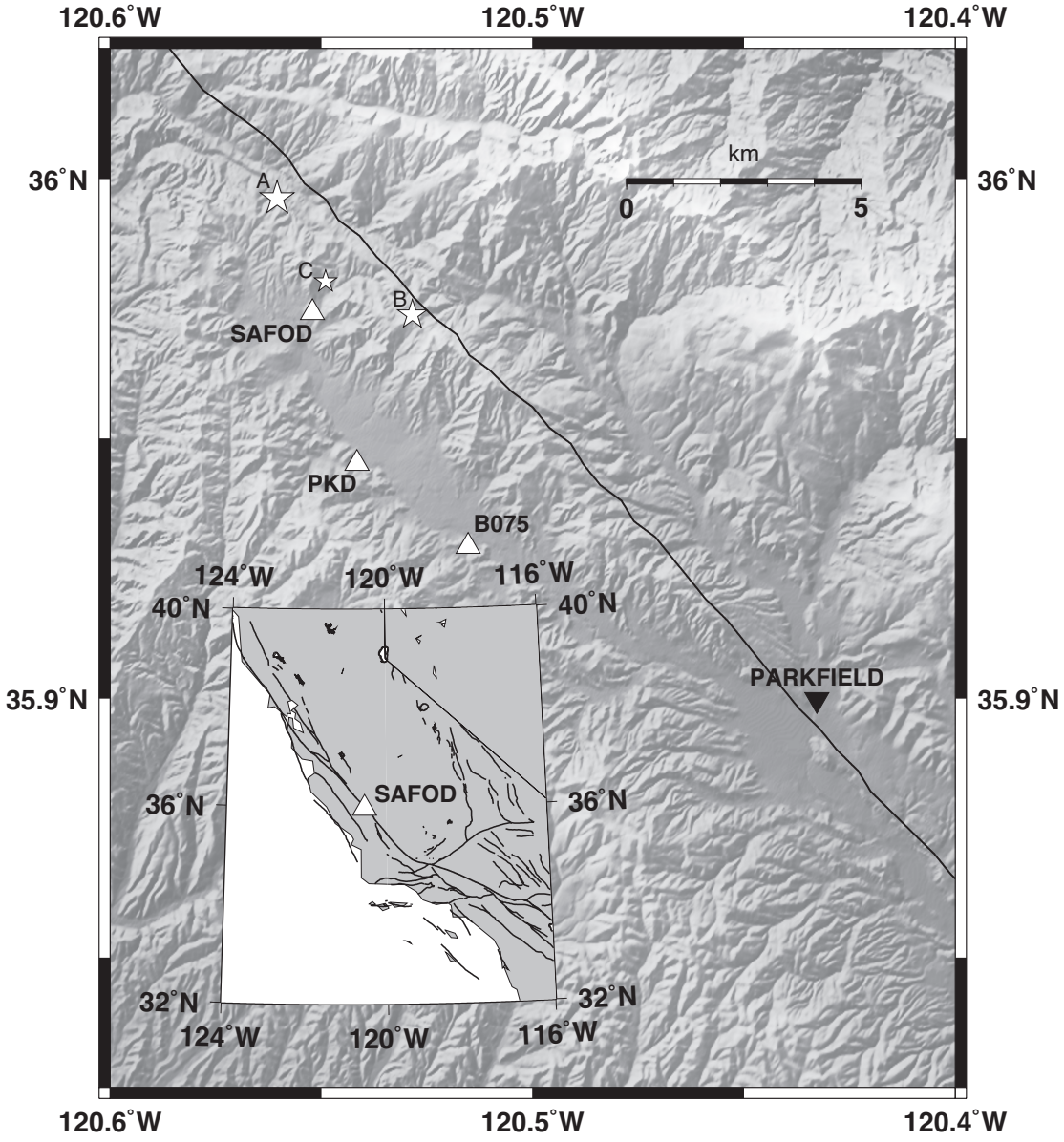

Figure 4.1: Map showing the location of SAFOD, seismic station PKD, and PBO station B075 used in this study, along with the local San Andreas Fault trace and the location of the microearthquakes (lettered stars) in Table 4.1.

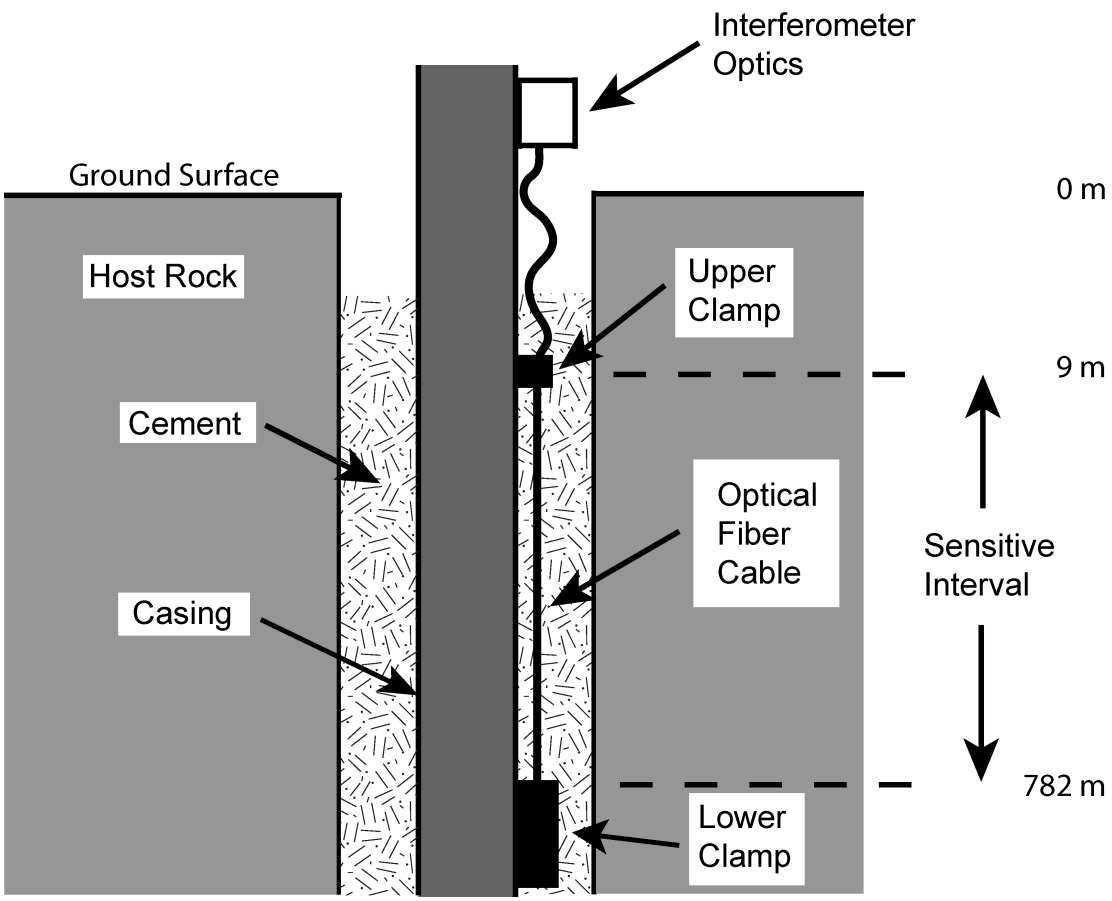

Figure 4.2: Schematic diagram of our interferometric, borehole strainmeter at SAFOD. Two sensors were installed simultaneously, ending at depths of 864 and 782 meters where a housing attached to the lower clamp holds the two spliced fibers in each cable.

obstruction in the blowout preventer.

The strain sensing cables were attached to the outer surface of the 9 & 5/8 inch inner casing (244.5 mm outer diameter, 220.5 mm inner diameter) of the SAFOD borehole as the casing was lowered (a 13 & 5/8 inch outer casing [339.7 mm OD, 313.6 mm ID] had been cemented into the hole prior to our installation). During installation, motorized supply spools pre-tensioned (stretched by about 0.02%) the cables as they were attached to the descending casing. After the casing was put in place, cement was pumped into the annular space between the casings, fixing the fiber cables to the casings and surrounding rock.

Each cable consists of two optical fibers encased in a flexible, stainless steel

jacket protected with a polyurethane coating. At the lower end of each cable, the two inner fibers are spliced to one another to form a long optical loop; they are also epoxied to the entrance of the splice protecting housing mounted to a clamp welded to the casing. At a depth of 9 m below the ground surface, an upper epoxy fixture attaches the fibers inside each cable to another clamp welded to the casing. The cables are under tension between the lower and upper clamps and loosely attached to the casing between the upper clamp and the surface, where they emerge through a flange at the wellhead. The lower ends of the two cables are at depths of 782 m and 864 m, making the sensitive intervals of the two strain sensors 773 m and 855 m in length. The 855 m sensor was monitored until 25 September, 2007, when the splice at the lower end failed (this occurred during continued drilling further down the SAFOD borehole). The 773 m sensor is still in operation.

To interferometrically record changes in the length of an optical fiber strainmeter, we form a Mach-Zender interferometer. In a junction box attached to the wellhead flange, an optical fiber coupler splits laser light into two arms: one is the borehole fiber loop, the other is a short loop within the junction box. Return light from the two arms is recombined using a second coupler and then passed to a photodetector and a digital signal processor (DSP) based fringe resolver (Zumberge et al., 2004). As the Earth strains, the optical path through the borehole fiber responds accordingly, forming interference fringes. The optical path difference is modulated by a piezoelectric transducer attached to the fibers inside the junction box to form a second fringe signal in quadrature with the direct signal. The DSP rapidly samples the two fringe signals and continuously calculates the optical phase, which is related to the change in length of the strain sensing fiber. A second interferometer monitors the apparent length of a 1560 m fiber wrapped around a mandril and buried for thermal stability, providing a laser wavelength fluctuation correction that is applied in post-processing. The laser (Koheras model Adjustik E15) and signal processing unit (Data Translations model DT9842), which consume some 50 W of electrical power, are housed in a trailer 35 m from the wellhead. Data are streamed via the internet to an archival computer in San Diego and at the NCEDC (Northern California Earthquake Data Center). Calibration proce-

dures for this type of instrument are described in Zumberge and Wyatt (1998) and Zumberge et al. (2002).

4.4 General Observations

4.4.1 Characteristics

Like other laser strainmeters (Agnew, 1986; Agnew and Wyatt, 2003), this is a relative measurement. If the data stream is interrupted for any reason, such as failure of an electronic component, there is no way to reconcile measurements surrounding the data gap aside from interpolation. The key advantage of this type of borehole strainmeter is the long baseline. Because strain ε is defined as $\Delta l/l$, strain noise decreases for a given displacement's (Δl) noise as the instrument's length l is increased. Optical fibers are also advantageous in that optical methods can be applied to detect a very small Δl, even when l is large, and they possess a large dynamic range (the initial stretch limits the maximum magnitude of negative strain, and the breaking point of optical fibers, about 2% of the initial length, determines the maximum allowable positive strain).

The main drawback to optical fibers as strain sensors is the temperature coefficient of the index of refraction, which can dominate strain signals at certain periods. This apparent strain coefficient is around 10^{-5} °C^{-1} (Butter and Hocker, 1978). Temperature, however, will affect the fibers in the borehole arm and the reference arm differently, as one segment is buried in the relatively stable environment of the borehole and the other is entirely on the surface. Figure 4.3 shows apparent strain and temperature records for a 170 hour interval spanning late February to early March, 2009. Temperature fluctuations at the wellhead contaminate the apparent strain measurement with around a 3 hour lag. We have yet to establish a reliable, linear method to subtract the temperature effect from the strain record.

The power-spectral density of the record in Figure 4.3 shows visible peaks corresponding to microseisms in the 6-8 s period range, and both diurnal and semi-diurnal peaks at near 24 and 12 hours, respectively. Those signals are primarily the result of temperature. This has prevented us from observing and removing the

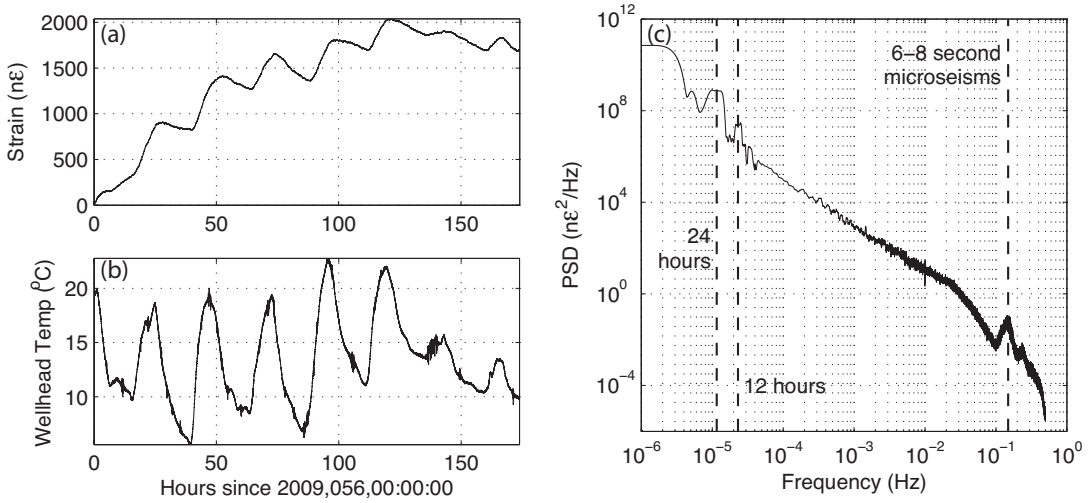

Figure 4.3: (a) Long strain record during a "quiet" period (no large earthquakes), showing an $\approx$ 24 hour signal. (b) Corresponding temperature record, recorded at the surface wellhead of the borehole strainmeter. (c) Power spectral density demonstrates significant signals at 24 hours, 12 hours, and microseisms from 6-8 seconds.

tidal records in the time series, which would require analyzing a several-month long record to differentiate tidal signals from temperature changes. While that record exists, there are practical challenges that make the correction beyond the reach of this study, such as occasional laser instability prompting "spikes" or brief gaps in the record. In this sense, the record is not fully continuous and would require these data issues to be manually corrected, which at present is beyond the scope of this dissertation.

Temperature sensitivity prohibits the use of this strainmeter for secular or tidal strain studies. An optical fiber strainmeter in which all of the temperature sensitive components are within the borehole, removed from surface temperature noise, is currently under construction at another facility. We note that the initial configuration as described in Blum et al. (2008) – which involved the entire interferometer being at depth within the borehole – would address the temperature problem, but that configuration only lasted 3.5 months as a 2 x 2 coupler at depth failed. The current configuration was redesigned onsite to overcome unexpected difficulties during deployment.

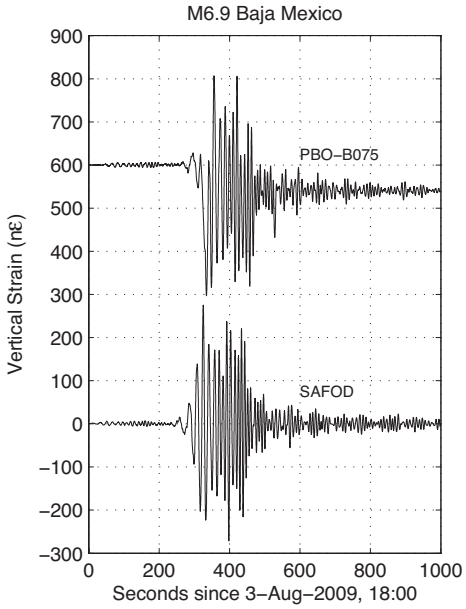

Figure 4.4: Vertical strain records at SAFOD and PBO-B075 from a $M6.9$ event in the Gulf of California, offshore Baja California, Mexico.

4.4.2 Observations of earthquakes

Temperature presents problems at diurnal periods, but the instrument signal-to-noise ratio is favorable at frequencies corresponding to earthquakes. We detect both ground motions from local microearthquakes as well as permanent coseismic offsets, along with strains from teleseismic earthquakes.

An example of a teleseismic event is shown in Figure 4.4 for a $M6.9$ earthquake in the Gulf of California offshore Baja California, Mexico on 3 August 2009. SAFOD experienced more than 400 $n\varepsilon$ peak-to-peak as the result of the surface waves. The Plate Boundary Observatory (PBO, 2010) station PBO-B075 , located $\approx$ 6 km from SAFOD, also recorded nearly 400 $n\varepsilon$ peak-to-peak vertical strain, which we calculated by transforming the recorded areal strain (e_A) to vertical strain (e_{zz}) using the plane-stress approximation, $e_{zz} = -\nu(1-\nu)^{-1}e_A$, with a Poisson's ratio of $\nu = 0.24$. The PBO-B075 record exhibits a permanent coseismic offset $>$ -50 $n\varepsilon$. The epicenter of this earthquake is $\approx$ 1050 km from both stations; elastic deformation theory (Okada, 1992) predicts a vertical strain offset of only $\approx$ -0.002 $n\varepsilon$, below the instrument resolution and the observed offset.

Similar coseismic strain-steps have been observed for local sources (Sacks et al., 1971; McGarr et al., 1982) and distant earthquakes (Ze-Hua and Yao-lin, 2004). One possible explanation is that the arriving surface waves create dynamic stresses (see, e.g., Marone, 2000) on local fault blocks or fractures that cause an immediate elastic response, resulting in deformation across smaller, kilometer-scale fault zones (Fialko et al., 2002). Another possibility is that the large dynamic strains create point defects due to coupling the strainmeter to less competent rock; the SAFOD instrument is less sensitive to this as it is coupled over the entire $\approx$ 800 m baseline (as opposed to 15 cm). The long baseline of our fiber systems would represent an advantage in this case. We note that some other nearby PBO stations (though not all) also exhibited strain steps. Whether such effects are physical, instrumental, or a combination of both is beyond the scope of this dissertation, but represent a possible future research direction.

Examples of some local microearthquakes (Table 4.1) near the SAFOD sensor are displayed in Figure 4.5. Events A and B exhibit offsets of $\approx$ -2 $n\varepsilon$ and 4 $n\varepsilon$, respectively. Applying a smoothing filter (Lowess method with a span of 5%) to the raw data clearly distinguishes the earthquake induced deformation. Event C displays no offset.

For comparison, we calculate theoretical strain offsets for a homogeneous half-space (Okada, 1992) and compute values of -0.97 and 0.13 $n\varepsilon$ for Events A and B, respectively. Zero coseismic strain is predicted for Event C due to its orientation with respect to the sensor and strike-slip faulting. For a layered crust [taken from CRUST2.0 at a location of 36N, 120W (Mooney et al., 1998; Bassin et al., 2000)], we use the EDGRN/EDCMP software from Wang et al. (2003) to predict offsets of -2.43, 0.35, and 0.00 $n\varepsilon$ for Events A, B, and C, respectively.

Possible error sources include uncertainties in crustal structure (i.e. sediment layering) and earthquake source parameters. Crustal structure is important, however, we only use average fault parameters at Parkfield with a strike of 314°, a dip of 89°, and a rake of $-180°$ (Mendoza and Hartzell, 2008). Uncertainties in the source parameters produce similar differences in the predicted strain-steps and are likely the more appropriate parameter to vary. The magnitudes and polarity

Table 4.1: Microearthquakes used in coseismic study.

Event	Date	Time	Latitude	Longitude	Depth (km)	M	R (km)
A	06/15/2008	05:26:54	35.9962 N	120.5605 W	4.05	3.23	4.79
B	07/06/2005	17:14:59	35.9738 N	120.5285 W	4.95	2.78	5.39
C	12/20/2008	06:22:19	35.9802 N	120.549 W	4.15	2.09	4.21

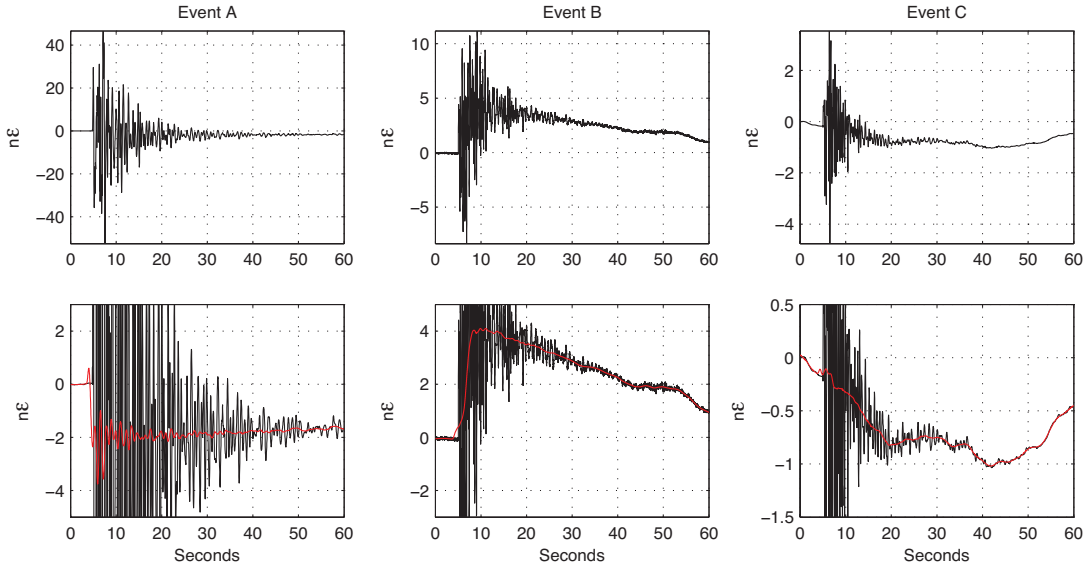

Figure 4.5: Observations of microearthquakes located near the SAFOD borehole. The top row shows the full record; the bottom row shows the same data but blown up with the raw record in black, and a smoothed record in red. Events A and B produce notable coseismic offsets whose magnitudes and polarity are consistent with elastic dislocation theory. Event C has no observed or predicted strain-step.

of the observed steps, however, are consistent with theoretical results. We propose that the ability to resolve these coseismic strain offsets to sub $n\varepsilon$ levels might be a potential tool to recover crustal structure and local fracture networks if coupled with accurate estimations of earthquake source.

We have also considered instrumental error sources that might be responsible for the the observed strain offsets, including local displacements at the endpoints of the sensor and miscounting in the fringe-signal processor. Local displacements between the cemented endpoints and the local rock would have to be on the order of microns to account for the observed offsets, which we consider unlikely. We have examined the records to be certain that the strain rates did not exceed the maximum rate allowed by our sampling interval and found that they were well below the acceptable range, indicating that fringe miscounting is not a cause of error. We believe the observed strain offsets are reliable at the 1 $n\varepsilon$ level. There is one fact worth noting for event B, however: this event occurred not long after the optical instrumentation was first installed, and in the early stage of operation, the

optics were configured such that the optical path length through the slack fiber in the 35 m conduit connecting the recording trailer to the wellhead was included in the strain measurement. It is possible that shaking during this microearthquake could have disturbed this length of slack fiber so as to cause (or increase) the apparent offset (though the laser reference fiber was also in this configuration for years, and no coseismic offsets have been observed.) This situation was rectified following event B by moving the key optical components to the wellhead.

4.5 Single-site estimation of phase velocity

We investigate the possibility of using the strainmeter to estimate local phase velocities by comparing observations of Rayleigh waves to a nearby seismometer. Seismic phase velocities are traditionally determined by measuring travel time arrivals over known distances, using networks comprised of widely spaced seismometers. Within the network, instrument separation must be large enough for satisfactory resolution of long wavelength arrivals. Large seismometer separation also filters contamination from small-scale refraction and diffraction of short wavelength waves.

Comparisons between collocated strainmeter and seismometer records can provide information about local seismic phase velocities that can not be directly inferred from the individual sensors (Benioff and Gutenberg, 1952). Mikumo and Aki (1964) first examined this idea using a horizontal pendulum seismometer and a collocated horizontal strainmeter. They observed five teleseismic earthquakes using both instruments and estimated local phase velocities using amplitudes, not travel times, and they found good agreement between measured and predicted phase velocities for body waves and, in some cases, surface waves. Okamoto et al. (2007a,b) similarly used horizontal strain components with velocity seismograms to estimate local Love wave and Rayleigh wave velocities in Japan; they discovered Love wave velocities were around 24% less and Rayleigh waves 54% greater than theoretical values, most likely the result of local geologic and topographic effects. Recent results comparing rotations to ground motions also contain information

about local phase velocities (see, e.g., Igel et al., 2005; Cochard et al., 2006; Kurrle et al., 2010), indicating the potential in using other deformation sensors in conjunction with seismometers in extracting the particulars of subsurface structure.

In this section, we present theory on how to estimate Rayleigh wave phase velocities from the comparison of vertical strain and vertical ground acceleration. We present results from measurements taken at the SAFOD borehole. To our knowledge, this is the first attempt to use vertical strain for such estimations.

Theory

Following King et al. (1976) and Sacks et al. (1976), we can express the vertical acceleration amplitude for the fundamental mode of a Rayleigh wave as

$$a_z(\omega) = -\frac{i\omega^2 \left(1-\gamma\right) A}{\kappa}, \tag{4.1}$$

and vertical strain amplitude as

$$e_{zz}(\omega) = ik\left(r^2+\gamma\right) A, \tag{4.2}$$

where $\gamma = \left(1 - \frac{c^2}{2\beta^2}\right)$ and $r = \sqrt{\frac{c^2}{\alpha^2} - 1}$. The parameters are A = amplitude constant, ω = angular frequency, c = Rayleigh wave phase velocity, $k = \omega/c$ = wave-number, and α and β are the P- and S-wave velocities at the surface. The ellipticity of particle motion, or κ, is the ratio of the axes of the elliptical ground motion in the radial-vertical plane (sometimes known as the H/V ratio), and can be expressed as

$$\kappa = \frac{v_r(\omega)}{v_z(\omega)}, \tag{4.3}$$

where v_r and v_z are the radial and vertical components of motion, respectively. Taking the ratio of vertical acceleration to vertical strain, substituting for Poisson's ratio $\nu = (\alpha^2 - 2\beta^2)/(2(\alpha^2 - \beta^2))$, and rearranging terms to solve for phase velocity, we have the following expressed in period $\tau = 2\pi/\omega$:

$$c(\tau) = \frac{-\nu}{1-\nu}\frac{\kappa\tau}{2\pi}\frac{a_z(\tau)}{e_{zz}(\tau)}. \tag{4.4}$$

We have thus arrived at a simple formulation to calculate phase velocity as a function of period. It requires us only to observe Rayleigh waves on a 3-component

seismometer (horizontal motions are needed to obtain the ellipticity) as well as on our optical fiber strainmeter.

It has been pointed out that phase velocity can also be estimated from the horizontal component of a seismometer in conjunction with strain. Similar to Mikumo and Aki (1964), if we assume a plane wave in an infinite inhomogeneous medium and transform areal strain to vertical strain via the plane-stress approximation, phase velocity can be expressed as

$$c(\omega) = \frac{-\nu}{1-\nu}\frac{v_r(\omega)}{e_{zz}(\omega)}, \tag{4.5}$$

where v_r is the radial component of motion (assuming in this expression that the Rayleigh wave arrives at zero angle with respect to one of the horizontal axes of the seismometer). Under specific conditions both expressions might lead to the same result. A problem exists, however, using horizontal components of motion: horizontal acceleration and tilt are difficult to separate for long periods ($>$ 100 s Rogers, 1968), and both seismometers and strainmeters encounter strain-strain and strain-tilt influences from local inhomogeneous rock properties (King et al., 1976). In particular, near-station inhomogeneous rock properties may produce azimuthal effects not considered in the plane-wave approximation of Mikumo and Aki (1964). Corrections can be made for these influences by applying a third-order tensor for seismometers and a fourth-order tensor for strainmeters. Vertical accelerations are neither affected by site effects nor contaminated by tilt. Therefore, we use the vertical acceleration formulation in Equation (4.4). Estimating the tensor coefficients needed to remove the site-effect influences on the strainmeter is beyond the scope of this dissertation; this method remains only a first order estimation.

One possible difficulty with this formulation is in estimating the ellipticity. The theory incorporates the approximation that ellipticity is frequency independent at the surface, while surface wave ray theory predicts that for a smooth, laterally heterogeneous and transversely isotropic earth, at a single-site, the ellipticity (or spectral ratio of the radial to vertical components) will depend on the local structure beneath the station (radial and vertical components will also be 90° out of phase). Therefore, ellipticity should be locally constant for all azimuths but should also depend on frequency (Woodhouse, 1974; Tromp and Dahlen, 1992a,b;

Ferreira and Woodhouse, 2007). The approximation above is valid as long as the length scale of lateral heterogeneities is large compared to the surface wave wavelength.

Several studies have utilized ellipticity measurements to determine local crustal structure beneath a station. Boore and Toksöz (1969) and Sexton et al. (1977) used Rayleigh waves with periods from 10-50 seconds to determine crustal structures within the near vicinity of the stations. Ellipticity measurements were especially useful in retrieving models with sedimentary layering. They provided an additional constraint towards uniqueness of model structure when used in conjunction with other geophysical data such as phase velocities from seismic arrays. At a single period, ellipticity values do exhibit variation depending on earthquake azimuth (Sexton et al., 1977; Munirova and Yanovskaya, 2001). This is attributed to poor signal-to-noise ratios and interference effects from scattering due to the presence of lateral heterogeneities. Averaging ellipticity values over different azimuths, however, suppressed path effects and allowed for the calculation of consistent crustal models (Munirova and Yanovskaya, 2001).

These results further support our choice in using the vertical-acceleration and vertical strain formulation in Equation (4.4). Ellipticity estimation depends on the horizontal components of ground motion (which we rotate to the radial component along the great circle path from source to receiver), which are subject to strain-strain and strain-tilt effects. Averaging over different azimuths appears to negate those influences, whereas a similar assumption might not be valid for Equation (4.5).

4.5.1 Data and Methods

Synthetic

We test the theory using PSVaxi, a higher-order finite-difference code that solves the elastic wave equation in spherical coordinates (Igel and Weber, 1996; Jahnke, 2008). PSVaxi generates global high frequency P-SV waves within an axisymmetric geometry using a heterogeneous Earth model.

We use the Preliminary Reference Earth Model (PREM: Dziewonski and

Anderson, 1981) for our calculations. We use a grid with 750 nodes in the z direction (corresponding to a vertical grid spacing of 4.7425 km) and 1750 nodes in the x direction, and we compute synthetic velocity and strain seismograms at epicentral distances from 5 to 90 degrees in 5 degree increments. The end result is the synthetic production of the components v_z and e_{zz}. We take the time derivative of the velocity seismogram to obtain acceleration.

Figure 4.6 shows the synthetic results. Upon arrival of the Rayleigh wave, there exists a clear correlation between the vertical acceleration and vertical strain terms (Figure 4.6a)). Waveforms were lowpass filtered with a cutoff period of 30 seconds. To estimate phase velocities according to Equation (4.4), we take the relevant amplitude spectra of signals for 21 synthetic events (using source depths at 10, 20, and 30 km and receivers at 5 degree increments from 60 to 90 degrees). The results are stacked and the mean synthetically determined phase velocity shown in Figure 4.6b along with 95% confidence limits (assuming errors are normally distributed) are compared to the PREM model. The synthetic results agree within the period band of 30 to 75 seconds to less than 10%, with an average difference of only 3.6%. Possible error sources include scattered and refracted P and SV waves but also numerical noise. These results demonstrate that this theory is appropriate for applications on real data, though it is important to reiterate: the theory is for the fundamental Rayleigh mode only and may be subject to contamination from higher modes.

Real Data

We examined SAFOD strain records around times corresponding to earthquakes in global earthquake catalogs to select teleseismic events. We restricted our search to events with $M_w \geq 6.5$ to ensure significant generation of low-noise, long period energy. We also restricted earthquakes to depths < 50 km to minimize overtone contamination. To limit near source effects and multiple orbit overlapping wave trains, we only examined events with epicentral distances between 50° and 120°. Due to various additional factors, such as noise from continue drilling of the SAFOD project, problems with our laser, or low signal-to-noise, we used only

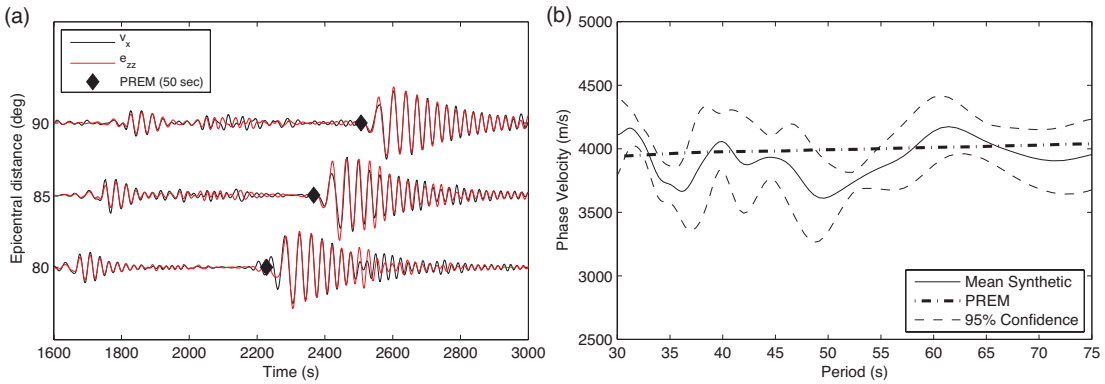

Figure 4.6: (a) Synthetic waveforms for a_z and e_{zz} recorded at epicentral receiver distances of 80, 85, and 90 degrees. Black diamonds denote the expected Rayleigh wave arrival time for the PREM model at periods of 50 seconds. Waveforms were lowpass filtered with a cutoff period of 30 seconds. (b) Phase velocities were estimated from synthetic spectra for 21 events; 95% confidence limits assume a normal distribution of errors.

9 earthquakes between August 2007, and January 2009. Events are listed in Table 4.2 and their locations are displayed in Figure 4.7.

One limitation to our study is that a broadband seismometer does not exist at the SAFOD site. Instead, we obtained three component seismic records for each event from station PKD: part of the Berkeley Seismic Network. Station PKD lies 3.36 km southwest of the SAFOD location. We used waveform cross correlation to align e_{zz} and a_z components, accounting for the arrival time delay from the station separation distance. Assuming a dominant period of 20 seconds, and a phase velocity of 4 km/sec, from $\lambda = c\tau$ we expect a characteristic Rayleigh wave wavelength to be around 80 km. This is much greater than the station separation distance and would seem to conform to our assumption of a medium whose lateral characteristics vary slowly compared to the station separation.

We obtained the radial component by rotating the E-and-N components along a great circle path to each earthquake source. We bandpass filtered all strain and seismic components between 10 and 200 seconds. Computing phase velocity requires estimating two spectral ratios – the ellipticity κ, which we obtain from the ratio of v_r to v_z – and the ratio of a_z to e_{zz}. Because the radial and vertical seismic components are theoretically out of phase by 90°, we applied a Hilbert transform to

Table 4.2: Teleseismic earthquakes used in Rayleigh wave study.

Date	Time	Latitude	Longitude	Depth (km)	M_w	Locality
08/15/2007	23:40:57	13.39 S	76.6 W	39	8	Peru
12/09/2007	07:28:21	25.87 S	177.52 W	30	7.8	Fiji
04/09/2008	12:46:12	20.07 S	168.89 E	33	7.3	Loyalty Islands
05/12/2008	06:28:01	31 N	103.32 E	19	7.9	China
10/16/2008	19:41:25	21.86 S	173.82 W	29	6.7	Tonga
10/19/2008	05:10:33	31.09 S	176.97 W	18	6.8	Kermadec Island
01/03/2009	19:43:53	0.51 S	132.78 E	35	7.6	Papua Indonesia
01/03/2009	22:33:42	0.71 S	133.34 E	35	7.4	Papua Indonesia
01/15/2009	17:49:39	46.81 N	155.15 E	36	7.4	Kuril Islands

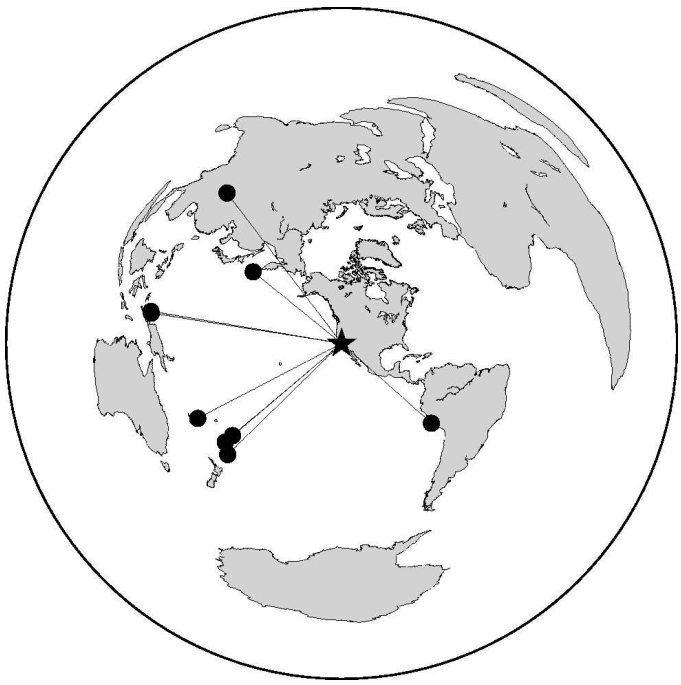

Figure 4.7: Azimuthal equidistant projection showing the epicenters of the teleseismic events used for velocity estimation in this study.

the radial component ($H(v_r)$), which has the effect of preserving amplitudes but shifting the radial component by 90° in phase (Ferreira and Woodhouse, 2007). We then estimated the required spectral ratios by calculating the transfer function between the respective components.

4.5.2 Results

As an example, we first analyze the $M7.3$ earthquake Loyalty Islands earthquake. Figure 4.8 shows the vertical strain and acceleration signals along with their correlation as a function of time. To compute correlation, we first narrowly bandpass filtered the signals between $0.9\tau - 1.1\tau$ for periods τ of 20 and 50 seconds. The filtered components should then contain only energy at those periods. We then calculate the correlation between signals every 5 seconds over a time window ranging from $\pm\tau$ [i.e., for the 20 second filtered signals, every 5 seconds, we calculated the correlation from ± 20 seconds around that point (two wavelengths)]. Vertical strain and vertical acceleration become highly correlated upon arrival of

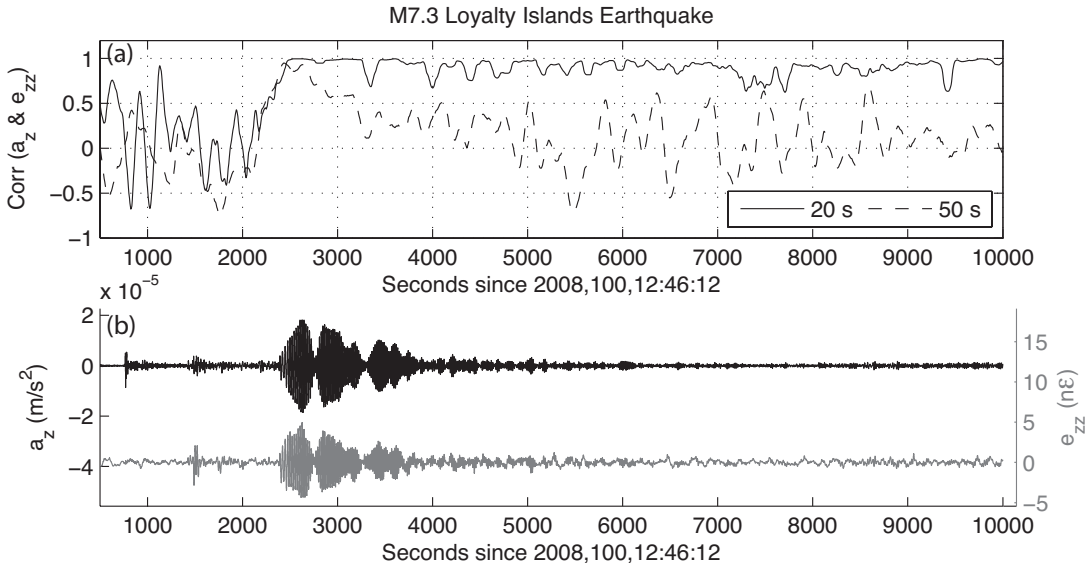

Figure 4.8: Record from the M7.3 Loyalty Island earthquake on 04/09/2008. (a) Correlation between a_z and e_{zz} for signals narrowly bandpass filtered with a passband from $0.9\tau - 1.1\tau$ for periods of 20 and 50 seconds. Correlations were calculated at 5 second intervals over a window spanning from $\pm\tau$ around each sample point, or over 2 cycles. (b) Vertical acceleration and strain signals de-trended and filtered between 10 and 200 seconds.

the first Rayleigh wave group and that correlation persists depending on period.

Figure 4.9 shows the first Rayleigh wave group for each of the relevant signals, along with the squared-coherency between signal pairs, resulting ellipticity κ, acceleration to strain ratio, and the resulting computed phase velocity for this event. The squared-coherency between e_{zz} and a_z is only well conditioned in the period range of 16 to 40 seconds. At periods where the coherency is low, the relationship between strain and acceleration is likely invalid.

The remaining earthquakes were analyzed in a similar manner. We placed several constraints on our analysis. For each earthquake, we required the squared-coherence between both v_z and $H(v_r)$, and e_{zz} and a_z, to be above 0.81. Only data points at periods meeting these criteria were included. We further required that at any period, at least 3 events (out of the 9 earthquakes) must meet the coherency criteria to use in subsequent analysis. This removed data at longer periods that often suffered lower signal to noise and limited the influence of any

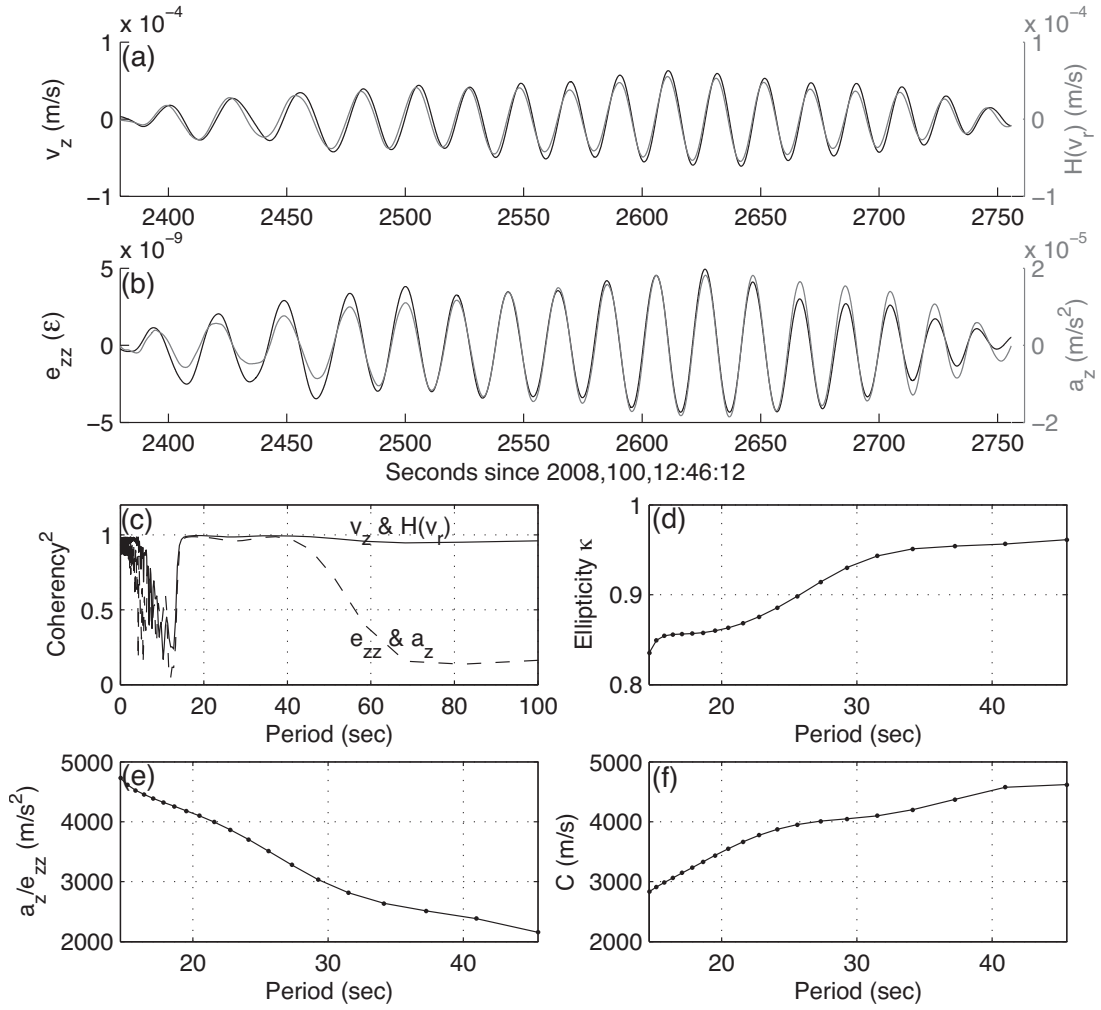

Figure 4.9: (a) First Rayleigh wave group for the M7.3 Loyalty Island earthquake, showing the relation between v_z and the Hilbert transformed radial component $H(v_r)$. (b) Corresponding e_{zz} and a_z components. (c) Coherency^2 between the v_z and $H(v_r)$, which are responsible for the ellipticity κ, and e_{zz} and a_z, which are responsible for the ratio a_z/e_{zz} in calculating phase velocity. (d) Estimation of ellipticity κ. (e) Estimation of the ratio a_z/e_{zz}. (f) Estimation of phase velocity.

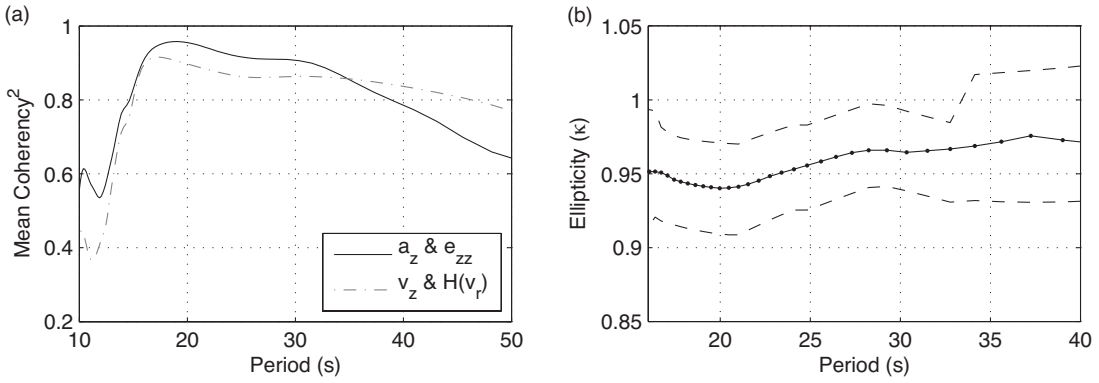

Figure 4.10: (a) Mean squared-coherence over all events between a_z & e_{zz} and v_z & $H(v_r)$ (ellipticity). (b)Spectral estimation of ellipticity. Dashed lines display the standard error.

single or anomalous event.

The mean squared-coherence over all events for the relevant spectral ratios roughly satisfies our selection criteria at periods between 16 and 40 seconds (Figure 4.10a). Values for ellipticity (κ) are shown in Figure 4.10b along with estimates of standard error at each period. Ellipticity is not constant, but varies by $< 3\%$ between 16 and 40 seconds. Phase velocities were then computed using Equation (4.4) using our constrained results for period, ellipticity, and the spectral ratio of a_z to e_{zz}. We used values of $\nu = 0.24$ taken from pilot hole velocity logs (Boness and Zoback, 2004). The results are shown in Figure 4.11. We estimate phase velocities between 3500 and 4500 m/s at periods between 16 and 40 seconds. These results agree to $< 8\%$ of the PREM model in that period range with a mean difference of 3.5%.

In comparison to our calculated phase velocities, we also plot two models, M1 and M2. Both models use the PREM model for the underlying mantle, but utilize variations of the CRUST2.0 model for the upper layers because SAFOD is located between two cells in the CRUST2.0; the proximity to the ocean limits interpolation. Model M1 is similar to the continental margin transition; model M2 is continental crust with 3 km of overlying sediments. Our intent with these models is to demonstrate the types of variations we would expect to see based on reasonable variations in crustal structure. These possible models fit our estimated

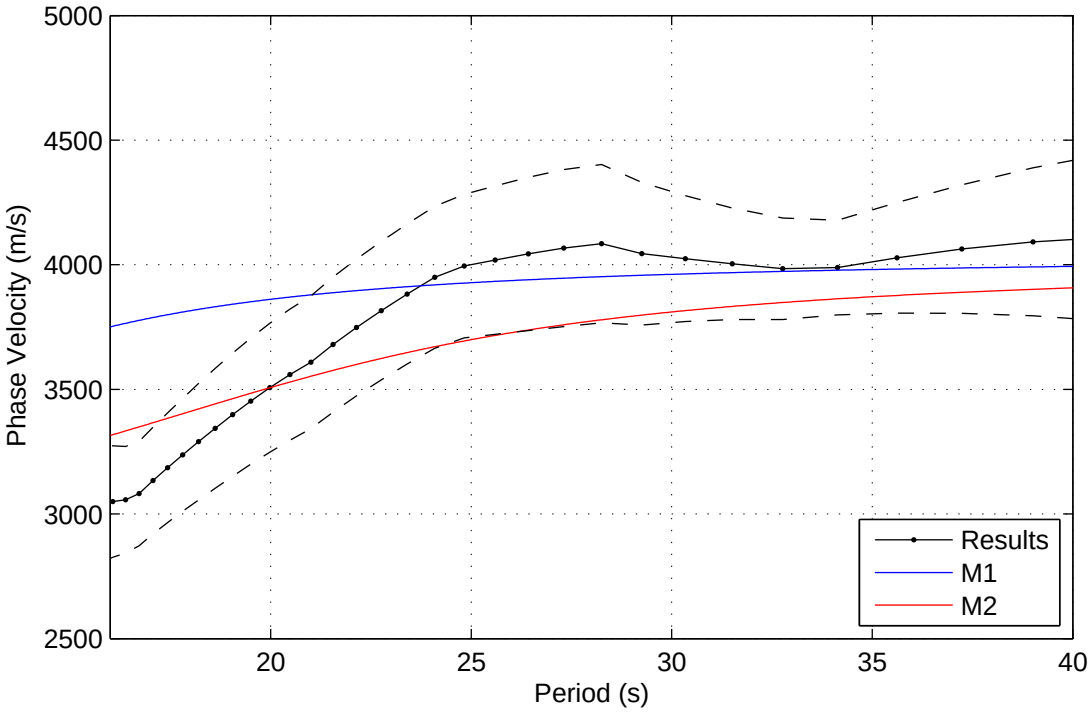

Figure 4.11: Spectral estimation phase velocity. Dashed lines display the standard error. Models M1 and M2 were calculated from the CRUST2.0 model atop of a PREM mantle.

results to within standard error for most of the coherent period range, with some departure at shorter periods.

4.5.3 Discussion

We successfully produced general phase velocity characteristics consistent with the variations expected for reasonable crust and upper mantle structure. Our results, however, are limited by a couple of factors. First, the number of available events is small (nine) and their azimuthal distribution is not uniform. Additionally, our seismometer and strainmeter were not collocated as the theory requires. This presents several problems. Boore and Toksöz (1969) discovered that ellipticity and phase velocities are equally sensitive to structural perturbations. Ellipticity, however, is more sensitive to the presence of low-velocity sedimentary layers, and predictions of ellipticity typically require the inclusion of sedimentary layering (Sexton et al., 1977). Local structure at Parkfield varies both vertically and horizontally across the fault (see, e.g., Eaton et al., 1970), but also includes significant variations on the Pacific side from which our events arrived. High-resolution seismic studies around SAFOD have revealed the presence of prominent low velocity zones at depth within the upper 1.5 km, possessing significant lateral variability with length scales on the order of hundreds of meters (Catchings et al., 2002). This result was confirmed by reports that examined cores from the SAFOD Pilot Hole (Boness and Zoback, 2004). Thus, our estimates of ellipticity from several kilometers away from SAFOD might slightly contribute to errors in our phase velocity estimation.

Other sources of error include the presence of vertical and lateral homogeneities, as well as the significant contrast in structure going across the San Andreas fault, which is only 1.8 km from the SAFOD borehole, may result in significant interference that prevents successful analysis at short periods where the signal to noise is contaminated with high frequency reflections, refractions, and diffractions, and long periods where the signal to noise of the strainmeter decreases, resulting in a lack of coherency with seismic accelerations. We also cannot discount the role of attenuation. The seismometer and strainmeter are not collo-

cated, and depending on azimuth, the separation distance may slightly attenuate one signal with respect to the other. We estimate attenuation over a distance of only 3.36 km, however, to be less than 1%, which is about the precision of the seismometer.

The most significant sources of error are likely to be the strain-strain and strain-tilt interactions, and contamination from higher modes. Interfering waves have been demonstrated to have a significant affect on ellipticity (Boore and Toksöz, 1969; Sexton et al., 1977), and they therefore arguably affect the ratio of acceleration to strain as well. This theory is only valid for the fundamental Rayleigh wave mode. The presence of higher mode surface waves has recently been shown to impede recovery of local dispersion characteristics in Love waves, though general dispersion characteristics can be recovered (Kurrle et al., 2010). Analogously, this method is only likely to recover general characteristics, and full waveform inversions may be required to recover structure (see, e.g., Ferreira and Igel, 2009).

4.6 Conclusions

We demonstrate the performance of an optical fiber, interferometric strainmeter sensing vertical strain in the SAFOD borehole. The strainmeter is capable of observing seismic waves similar to a seismometer and permanent, earthquake induced deformation. Using teleseismic events as a source, we demonstrate that general characteristics of local Rayleigh wave phase velocities can be estimated from collocated measurements of vertical seismic acceleration and vertical strain. We observe phase velocities between to within a few percent of viable Earth models at periods from 16 to 40 seconds. This is the first time vertical strain has been used in conjunction with acceleration to estimate phase velocity.

This method may be particularly well exploited in areas that have multiple collocated strainmeters and seismometers. Areas include the recent EarthScope project (see, e.g., `http://www.earthscope.org`) and the Plate Boundary Observatory (Miller and Jackson, 2009), as well as geothermal and oil and gas fields

which may contain both strainmeters and seismometers for reservoir monitoring and management. While higher order modes may impede the full recovery of local structure in these areas, previous results for rotations (Bernauer et al., 2009; Kurrle et al., 2010) – and now, in this study, strain – suggest that these methods should be incorporated into geophysical problems where data collection allows, as such collocated measurements can constrain, refine, or extract more realistic models of the local Earth. Future research directions include insulating the wellhead to limit the influence of temperature at long periods and examining ambient noise and transient signals.

4.7 Acknowledgements

We would like to thank Gabi Laske for stimulating discussions and assistance in deriving local dispersion curves from CRUST2.0. Comments from two anonymous reviewers led to important conclusions in the manuscript. We also acknowledge P. Durdevic, J. Lemire, S. Nooner, M. Norenberg, P. Walsh, and J. White for assisting in the deployment and maintenance of the strainmeter, as well as K. Walker for near real time data processing and archival. Maps were made using Generic Mapping Tools. M. Zoback, B. Ellsworth, and S. Hickman have also all contributed to various phases of our strainmeters development and we owe its success to their work.

Much of this chapter has been accepted for publication in the following manuscript: **Blum, J., Igel, H., and Zumberge, M., 2010: Observations of Rayleigh wave phase velocity and coseismic deformation using an optical fiber, interferometric vertical strainmeter at the SAFOD borehole, California. *Bulletin of the Seismological Society of America*, 100(5A), In Press**. The author's contribution to this study was to write the published manuscript and to assist with the design, development, and deployment of the optical system at SAFOD, as well as re-deriving the theory and all data analysis. Heiner Igel provided a modified version of PSVaxi which the author used to generate the synthetic seismograms, and both he and Mark Zumberge helped contribute

to the data interpretation.

REFERENCES

Agnew, D., 1986: Strainmeters and tiltmeters. *Rev. Geophys.*, **24**, 579–624.

Agnew, D., and Wyatt, F., 2003: Long-base laser strainmeters: a review. Technical report, Scripps Institution of Oceanography.

Bakun, W., Aagaard, B., Dost, B., Ellsworth, W., Hardebeck, J., Harris, R., Ji, C., Johnston, M., Langbein, J., Lienkaemper, J., Michael, A., Murray, J., Nadeau, R., Reasenberg, P., Reichle, M., Roeloffs, E., Shakal, A., Simpson, R., and Waldhauser, F., 2005: Implications for prediction and hazard assessment from the 2004 Parkfield earthquake. *Nature*, **437**, 969–974.

Bakun, W., and Lindh, A., 1985: The Parkfield, California earthquake prediction experiment. *Science*, **229**, 619–624.

Bakun, W., and McEvilly, T., 1984: Recurrence models and Parkfield, California, earthquakes. *J. Geophys. Res.*, **89**, 3051–3058.

Bassin, C., Laske, G., and Masters, G., 2000: The current limits of resolution for surface wave tomography in North America. *EOS Trans. AGU*, **81**, F897.

Benioff, H., and Gutenberg, B., 1952: The response of strain and pendulum seismographs to surface waves. *Bull. Seismol. Soc. Am.*, **43**, 229–237.

Bernauer, M., Fichtner, A., and Igel, H., 2009: Inferring Earth structure from combined measurements of rotational and translational ground motions. *Geophysics*, **74**(6), 41–47.

Blum, J., Nooner, S., and Zumberge, M., 2008: Recording Earth strain with optical fibers. *IEEE Sensors Journal*, **8**(7), 1152–1160.

Boness, N., and Zoback, M., 2004: Stress-induced seismic velocity anisotropy and physical properties in the SAFOD pilot hole in Parkfield, CA. *Geophysical Research Letters*, **31**.

Boore, D., and Toksöz, M., 1969: Rayleigh wave particle motion and crustal structure. *Bulletin of the Seismological Society of America*, **59**(1), 331–346.

Burford, R., and Harsh, P., 1980: Slip on the San Andreas fault in central California from alinement array surveys. *Bull. Seismol. Soc. Am.*, **70**, 1233–1261.

Butter, C., and Hocker, G., 1978: Fiber optics strain gauge. *Applied Optics*, **17**, 2867–2869.

Catchings, E., Rymer, M., Goldman, M., Hole, J., Huggins, R., and Lippus, C., 2002: High-resolution seismic velocities and shallow structure of the San Andreas Fault Zone at Middle Mountain, Parkfield, California. *Bull. Seismol. Soc. Am.*, **92**, 2493–2503.

Cochard, A., Igel, H., Schuberth, B., Suryanto, W., Velikoseltsev, A., Schrieber, U., Wassermann, J., Scherbaum, F., and Vollmer, D., 2006: Rotational motions in seismology: theory, observation, simulation. In *Earthquake source asymmetry, structural media and rotation effects*, editors R. Teisseyre, M. Takeo, and E. Majewski, 391–411. Springer-Verlag.

Dziewonski, A., and Anderson, D., 1981: Preliminary Reference Earth Model. *Phys. Earth and Planet. Int.*, **25**, 297–356.

Eaton, J., O'Neil, M., and Murdock, J., 1970: Aftershocks of the 1966 Parkfield-Cholame, California earthquake. *Bull. Seismol. Soc. Am.*, **60**, 1151–1197.

Ferreira, A., and Igel, H., 2009: Rotational motions of seismic surface waves in a laterally heterogeneous Earth. *Bull. Seismol. Soc. Am.*, **99**, 1429–1436.

Ferreira, A., and Woodhouse, J., 2007: Observations of long period Rayleigh wave ellipticity. *Geophysical Journal International*, **169**, 161–169.

Fialko, Y., Sandwell, D., Agnew, D., Simons, M., Shearer, P., and Minster, B., 2002: Deformation on nearby faults induced by the 1999 Hector Mine earthquake. *Science*, **297**, 1858–1862.

Grandori, G., Guagenti, E., and Petrini, L., 2008: Statistical grounds for favoring the characteristic magnitude model: a case study. *Bull. Seismol. Soc. Am.*, **98**, 2161–2169.

Hickman, S., Zoback, M., and Ellsworth, W., 2004: Introduction to special section: preparing for the San Andreas Fault Observatory at Depth. *Geophys. Res. Lett.*, **31**.

Hickman, S., Zoback, M., Younker, L., and Ellsworth, W., 1994: Deep scientific drilling in the San Andreas Fault Zone. *EOS Trans. AGU*, **75**, 137.

Igel, H., Schrieber, U., Flaws, A., Schuberth, B., Velikoseltsev, A., and Cochard, A., 2005: Rotational motions induced by the $M8.1$ Tokachi-oki earthquake, September 25, 2003. *Geophys. Res. Lett.*, **32**.

Igel, H., and Weber, M., 1996: P-SV wave propagation in the Earth's mantle using finite-differences: application to heterogeneous lowermost mantle structure. *Geophys. Res. Lett.*, **23**, 415–418.

Imanishi, K., and Ellsworth, W., 2006: Source scaling relationships of microearthquakes at Parkfield, CA, determined using the SAFOD pilot hole seismic array. In *AGU monograph on earthquakes: radiated energy and the physics of earthquake faulting*, 81–90. AGU.

Jackson, D., and Kagan, Y., 2006: The 2004 Parkfield earthquake, the 1985 prediction, and characteristic earthquakes: lessons for the future. *Bull. Seismol. Soc. Am.*, **96**, 397–409.

Jahnke, G., 2008: *Methods for seismic wave propagation on local and global scales with finite differences.* Ph.D. thesis, Ludwig-Maximilians-Universitat Munchen.

Kagan, Y., 1993: Statistics of characteristic earthquakes. *Bull. Seismol. Soc. Am.*, **83**, 7–24.

King, G., Zurn, W., Evans, R., and Emter, D., 1976: Site correction for long period seismometers, tiltmeters and strainmeters. *Geophys. J. R. astr. Soc.*, **44**, 405–411.

Kurrle, D., Igel, H., Ferreira, A., Wassermann, J., and Schrieber, U., 2010: Can we estimate local love wave dispersion properties from collocated amplitude measurements of translations and rotations? *Geophys. Res. Lett.*, **37**, L04307.

Langbein, J., Borcherdt, R., Dreger, D., Fletcher, J., Hardebeck, J., Hellweg, M., Ji, C., Johnston, M., Murray, J., and Nadeau, R., 2005: Preliminary report on the 28 September 2004, M 6.0 Parkfield, California earthquake. *Seismol. Res. Lett.*, **76**, 10–26.

Lisowski, M., and Prescott, W., 1981: Short-range distance measurements along the San Andreas fault system in central California, 1975 to 1979. *Bull. Seismol. Soc. Am.*, **71**, 1607–1624.

Marone, C., 2000: Earthquake science: shaking faults loose. *Nature*, **408**, 533–535.

McCloskey, J., and Bean, C., 1994: Temporally unstable recurrence behavior in large earthquakes due to breaks in fractal scaling. *Science*, **266**, 410–412.

McGarr, A., Sacks, I., Linde, A., Spottiswoode, S., and Green, R., 1982: Coseismic and other shortterm strain changes recorded with Sack-Evertson strainmeters in a deep mine, South Africa. *Geophysical Journal International*, **70**, 717–740.

Mendoza, C., and Hartzell, S., 2008: Finite-fault analysis of the 2004 Parkfield, California earthquake using P_{nl} waveforms. *Bull. Seismol. Soc. Am.*, **98**, 2746–2755.

Mikumo, T., and Aki, K., 1964: Determination of local phase velocity by intercomparison of seismograms from strain and pendulum instruments. *Journal of Geophysical Research*, **69**(4), 721–731.

Miller, M., and Jackson, M., 2009: Plate Boundary Observatory (PBO), MREFC close end of project report. Technical report, UNAVCO.

Mooney, W., Laske, G., and Masters, G., 1998: Crust5.1: A global crustal model at 5x5 degrees. *J. Geophys. Res.*, **103**, 727–747.

Munirova, L., and Yanovskaya, T., 2001: Spectral ratio of the horizontal and vertical Rayleigh wave components and its application to some problems of seismology. *Izvestiya, Physics of the Solid Earth*, **37**(9), 10–18.

Nadeau, R., Antolik, M., Johnson, P., Foxall, W., and McEvilly, T., 1994: Seismological studies at Parkfield III: microearthquake clusters in the study of fault-zone dynamics. *Bull. Seismol. Soc. Am.*, **84**, 247–263.

Nadeau, R., Foxall, W., and McEvilly, T., 1995: Clustering and periodic recurrence of microearthquakes on the San Andreas Fault at Parkfield, CA. *Science*, **267**, 503–507.

Nadeau, R., and McEvilly, T., 1997: Seismological studies at Parkfield V: characteristic microearthquake sequences as fault-zone drilling targets. *Bull. Seismol. Soc. Am.*, **87**, 1463–1472.

Okada, Y., 1992: Internal deformation due to shear and tensile faults in a half-space. *Bull. Seismol. Soc. Am.*, **82**, 1018–1040.

Okamoto, T., Ikegami, Y., and Kokubo, K., 2007a: Local effects on strain seismograms at Matsushiro Seismological Observatory -1. Love waves. *Terr. Atmos. Ocean. Sci.*, **18**, 547–565.

Okamoto, T., Ikegami, Y., and Kokubo, K., 2007b: Local effects on strain seismograms at Matsushiro Seismological Observatory -2. Rayleigh waves. *Terr. Atmos. Ocean. Sci.*, **18**, 901–921.

Otero, J., 2009: *Development and characterization of an observatory-class, broadband, non-fedback, leaf-spring interferometric seismometer.* Ph.D. thesis, University of California San Diego, La Jolla, CA.

PBO, 2010: Plate boundary observatory. *http://pboweb.unavco.org/.*

Rogers, P., 1968: The response of the horizontal pendulum seismometer to Rayleigh and Love waves, tilt, and free oscillations of the Earth. *Bull. Seismol. Soc. Am.*, **58**, 1364–1406.

Sacks, I., Snoke, J., Evans, R., King, G., and Beavan, J., 1976: Single-site phase velocity measurement. *Geophys. J. R. astr. Soc.*, **46**, 253–258.

Sacks, I., Suyehiro, S., and Evertson, D., 1971: Sacks-Evertson strainmeter, its installation in Japan and some preliminary results concerning strain steps. *Pap. Met. Geophys.*, **22**, 195–207.

Schwartz, D., and Coppersmith, K., 1984: Fault behavior and characteristic earthquakes: examples from the Wasatch and San Andreas faults. *J. Geophys. Res.*, **89**, 5681–5698.

Sexton, J., Rudman, A., and Mead, J., 1977: Ellipticity of Rayleigh waves recorded in the midwest. *Bulletin of the Seismological Society of America*, **67**(2), 369–382.

Sieh, K., 1978: Slip along the San Andreas Fault associated with the great 1857 earthquake. *Bull. Seismol. Soc. Am.*, **68**, 1421–1447.

Titus, S., DeMets, C., and Tikoff, B., 2005: New slip rate estimates for the creeping segment of the San Andreas fault, California. *Geology*, **33**, 205–208.

Tromp, J., and Dahlen, F., 1992a: Variational principles for surface wave propagation on a laterally heterogeneous Earth I. Time domain JWKB theory. *Geophys. J. Int.*, **109**, 581–598.

Tromp, J., and Dahlen, F., 1992b: Variational principles for surface wave propagation on a laterally heterogeneous Earth II. Frequency-domain JWKB theory. *Geophys. J. Int.*, **135**, 599–619.

Wang, R., Martinez, F., and Roth, F., 2003: Computation of deformation induced by earthquakes in multi-layered elastic crust – FORTRAN programs EDGRN/EDCMP. *Computers & Geosciences*, **29**, 195–207.

Woodhouse, J., 1974: Surfac waves in a laterally varying layered structure. *Geophys. J. R. Astr. Soc.*, **37**, 461–490.

Ze-Hua, Q., and Yao-lin, S., 2004: Application of observed strain steps to the study of remote earthquake stress triggering. *Acta Seismologica Sinica*, **17**, 534–541.

Zumberge, M., 1997: Precise optical path length measurement through an optical fiber: application to seafloor strain monitoring. *Ocean Eng.*, **24**, 531–542.

Zumberge, M., Berger, J., Dzieciuch, M., and Parker, R., 2004: Resolving quadrature fringes in real time. *Applied Optics*, **43**, 771–775.

Zumberge, M., Berger, J., Hedlin, M., Husmann, E., Nooner, S., Hilt, R., and Widmer-Schnidrig, R., 2003: An optical fiber infrasound sensor: a new lower limit on atmospheric pressure noise between 1 and 10 hz. *J. Acoust. Soc. America*, **113**, 2474–2479.

Zumberge, M., Berger, J., Otero, J., and Wielandt, E., 2010: An optical seismometer without force feedback. *Bulletin of the Seismological Society of America*, **100**(2), 598–605.

Zumberge, M., Husmann, E., Elsberg, D., Harrison, W., Morack, J., Pettit, E., and Waddington, E., 2002: Measurement of vertical strain and velocity at Siple Dome with optical sensors. *J. Glaciology*, **48**, 217–225.

Zumberge, M., and Wyatt, F., 1998: Optical fiber interferometers for referencing surface benchmarks to depth. *Pure Appl. Geophys.*, **152**, 221–246.

Chapter 5

Geohazards in the Santa Barbara Basin

5.1 Abstract

Seafloor slope instability in the Santa Barbara Basin poses risk to the populated coastline. Two prominent landslide features, the Goleta and Gaviota slides, occupy the northern flank of the basin, with a scarp-like crack extending eastward from the headwall of the Gaviota slide towards the Goleta complex. Downslope creep is one process that leads to slope failure and active deformation across the crack might indicate higher risk. Sub-bottom CHIRP profiles with < 1 m accuracy across the crack exhibit no evidence of internal deformation. Daily seafloor acoustic range measurements connecting transponders spanning the crack detected no significant motion above a 99% confidence level of $\pm$ 7 mm/yr over two years of monitoring. These disparate data over different timescales indicate no downslope creep across this margin, suggesting that the elongated scarp-like crack is most likely a relict feature formed concomitantly with the adjacent Gaviota failure.

The M7.1 earthquake of 21 December 1812 is often attributed as the trigger of the Gaviota landslide, with a source initially within the Santa Barbara Basin. Other fault sources including the San Andreas and San Cayetano fault have been proposed. Given the uncertainties in the slide date, we examine these fault sources

and whether they could match both historical intensities observed at missions, as well as produce the required ground shaking to induce failure. Using sediment cores and a generalized Newmark model, we confirm that $\approx 0.12g$ of ground acceleration is needed to induce failure. Probabilistic seismic hazard models predict that an earthquake within the basin could best produce similar ground acceleration and match the observed intensities. This result argues against relocating the event to other faults and suggests that the 21 Dec. 1812 event occurred within the Santa Barbara Basin.

5.2 Introduction

Submarine landslides are common features along many continental margins. The consequences of these events include the destruction of seafloor infrastructure, tsunami, and the loss of human life (Masson et al., 2006). Effective mitigation strategies require identifying future areas susceptible to failure, monitoring high-risk submarine slopes, and modeling the consequences. In 2004, we began developing innovative instrumentation to assess submarine slope stability, including the enhancement of seafloor acoustic ranging systems and the fiber optic seafloor strainmeter (FOSS: Blum et al., 2008) discussed in Chapters 2 and 3. In this study, we present results from CHIRP sub-bottom profiles and a two year deployment of an acoustic ranging system deployed across a potentially active forming future head scarp of a submarine landslide in the Santa Barbara Basin. We also examine the seismic-landslide triggering potential of various earthquake sources often attributed to a historical event, the Gaviota slide, in 1812.

5.3 Geologic Background

The Santa Barbara Basin is bounded by the Channel Islands to the south and the Santa Ynez mountains to the north (Figure 5.1). At least 15 earthquakes of $M \geq 5.0$ have affected the region between 1800 and 1999 (Toppozada et al., 2000), with large historical events occurring in 1812 (M 7.1),1925 (M 6.8), 1927

(M 7.1) (Toppozada and Branum, 2004) and a surprisingly damaging event in 1978 (M 5.1) (Miller, 1979; Corbett and Johnson, 1982).

Normal, reverse faults, and landslides occupy the basin (Eichhubl et al., 2002; Fisher et al., 2005; Greene et al., 2006), most notably the Goleta and Gaviota slides on the north flank (Figure 5.2.) The Goleta slide is located southwest of Coal Oil Point and measures 10.5 km wide with a head to toe distance of 14.6 km, displacing a total volume of 1.75 km^3 (Greene et al., 2006). Three prominent lobes comprise the bulk of the complex, with ages ranging from a minimum of 5.5 ka (Lee et al., 2004) to a maximum of 37 ka (Greene et al., 2006). Using the western lobe as a hypothetical tsunami source, Greene et al. (2006) modeled a tsunami with a maximum wave runup of 10 m and a maximum landward inundation of over 2 km.

The Gaviota slide is located approximately 8 km west of the Goleta Complex, and is roughly 1.65 km wide and 2.6 km long and involved the displacement of 0.01-0.02 km^3 (Edwards et al., 1995). The Gaviota slide is estimated to have occurred between 1715 and 1840 (Schwehr et al., 2006), and is commonly attributed to the M 7.1 earthquake of 21 December 1812 due to its age and reports of a tsunami following the main shock (Lander et al., 1993). Borrero et al. (2001) modeled a tsunami with a source similar in size and location and obtained wave runup of 1-2 m. Geotechnical analyses of surrounding sediment cores showed that moderate shaking of $0.12g$ could have induced sediment failure (Lee and Edwards, 1986), suggesting a $M \approx 7.5$ source (Edwards et al., 1995).

Between these slides exists a highly gullied slope with what resembles a crack or head scarp running more than 7 km from adjacent to the Gaviota headwall towards the Goleta complex, thinning eastward (Figure 5.2). At its widest, this depression is $\approx$ 10 m wide and 2 m deep. The eastern end terminates in a region of gradually increasing slope gradient (from 4°-12°) along with an increase in gullies ($\approx$ 8 gullies/km). Greene et al. (2006) suggest that this gullied bulge may be creeping downslope and prone to failure. They calculate that failure of this section would produce a local tsunami with a maximum runup of 5.7 m and 280 m landward inundation. Dingler (2007) argues that the bulge is at a lower risk for

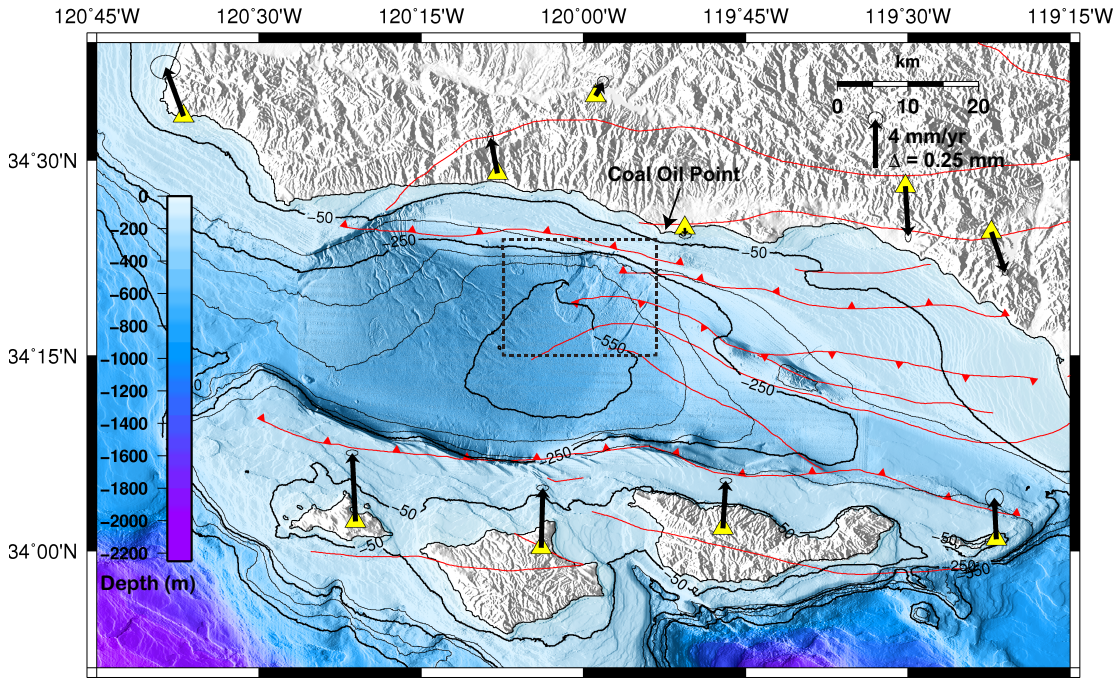

Figure 5.1: Santa Barbara Basin. Faults (red) are from Fisher et al. (2005) and the US Geological Survey. GPS velocity vectors (black arrows) are calculated relative to the mean velocity of stations (yellow triangles) on the northern flank and indicate $\approx -4.45 \pm 0.49$ mm/yr North-South compression of the Channel Islands with respect to the northern coast. The inset dashed black box shows the location of this study (Figure 5.2.)

failure, as the gullies introduce sediment heterogeneity along the relief, inhibiting the development of high pore pressures. The goals of this study are to address whether this seafloor crack is actively deforming or if it is a relict feature associated with the adjacent Gaviota failure. Active deformation of the margin may indicate higher risk to the nearby, populated coastline. We also desire to assess what earthquake source is required to generate sufficient ground acceleration to induce seafloor slope failures such as the Gaviota slide.

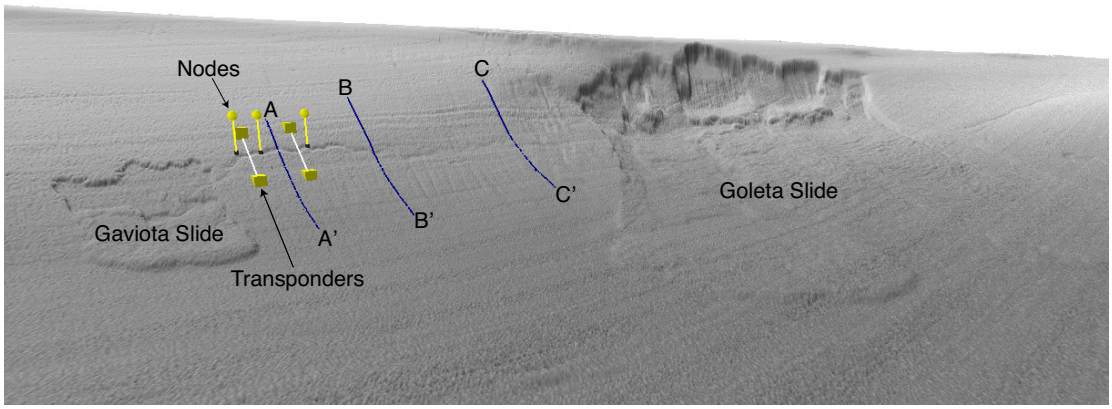

Figure 5.2: 3D perspective (10x vertical exaggeration) showing the location of the moored nodes (yellow spheres), transponders (yellow cubes) and CHIRP sub-bottom profile (blue line) shown in this study. Lengths of the CHIRP lines are: A-A', 2.495 km; B-B', 2.968 km; C-C', 3.020 km. White lines denote the measurement between transponder pairs.

5.4 Deformation across a seafloor crack

5.4.1 CHIRP

Evidence of downslope creep can delineate areas susceptible to failure (O'Leary and Laine, 1996). Internal, arcuate deformation of strata , for example, has been interpreted as creep-induced deformation upslope of gas blowouts on the U.S. East coast (Hill et al., 2004; Newman et al., 2007). Arcuate folds also exist along the Central Adriatic Deformation Belt above a thin detachment layer (Canals et al., 2004). Similar subsurface expressions of creep across the crack between the Gaviota and Goleta slides may therefore indicate imminent failure.

High-resolution CHIRP seismic data were collected over a region enveloping the Gaviota and Goleta slides during 2004 and 2006 cruises. Approximately 350 km of seismic lines were collected in this area. We used a modified Edgetech SubScan (digital) CHIRP profiler to acquire data with a 1-6 kHz pulse (50 ms in 2004, 35 ms in 2006). The CHIRP system is capable of resolving features < 1 m in thickness in the upper 50 to 75 m of the seabed.

Analysis of our CHIRP profiles indicates no evidence of down-slope creep along the margin between the Gaviota and Goleta slides. Figure 5.3 displays line

A-A' which crosses through the acoustic network (see Figure 5.2). We observe no deformation such as arcuate folds of strata similar to other studies (e.g., O'Leary and Laine, 1996; Hill et al., 2004; Canals et al., 2004). Deformation appears to exist only at the crack as a vertical offset and not further downslope or within the bounds of the acoustic ranging network. Similarly, in Lines B-B' (Figure 5.4) and C-C' (Figure 5.5), which is closer to the "bulge" that Greene et al. (2006) asserts is likely more prone to failure, we observe no indicators of down-slope creep. Analyses of an additional 13 CHIRP lines not displayed in this dissertation result in the same conclusion.

This observation is consistent with 3D elastic shear stress models of submarine landslides. Martel (2004) demonstrated that generally, downslope deformation will precede surface fracturing, but for slip patches that are less than twice as long as they are wide – consistent with the dimensions of the margin between the Gaviota and Goleta slides – landslides will initiate with a fracture at the head and then 'unzip' downslope. The model implies that the crack would form first and would suggest near imminent failure if the surface fracture were a new active feature. An ROV dive in 2006 revealed no evidence indicating recent crack movement or growth (Greene et al., 2006), and the smooth fracture morphology suggests that it is an old feature. Geotechnical assessment of sediment cores suggests that the sediment shear strength in the region would resist downslope gravitational stresses, and that only earthquake loading can generate sufficient downslope stress to trigger failure (Lee and Edwards, 1986; Lee et al., 1991). This implies that the seafloor crack is likely an older feature that formed in response to a large $M = 7.0 - 7.5$ event (Edwards et al., 1995). Given its morphology – extending eastward from the Gaviota slide and thinning from west to east – the CHIRP results indicate that the crack most likely formed when the Gaviota failure occurred but did not progress into a slide.

5.4.2 Acoustic ranging from nodes

We developed a new seafloor geodetic technique to monitor deformation along slopes. Existing approaches struggled with relief (Chadwell et al., 1999),

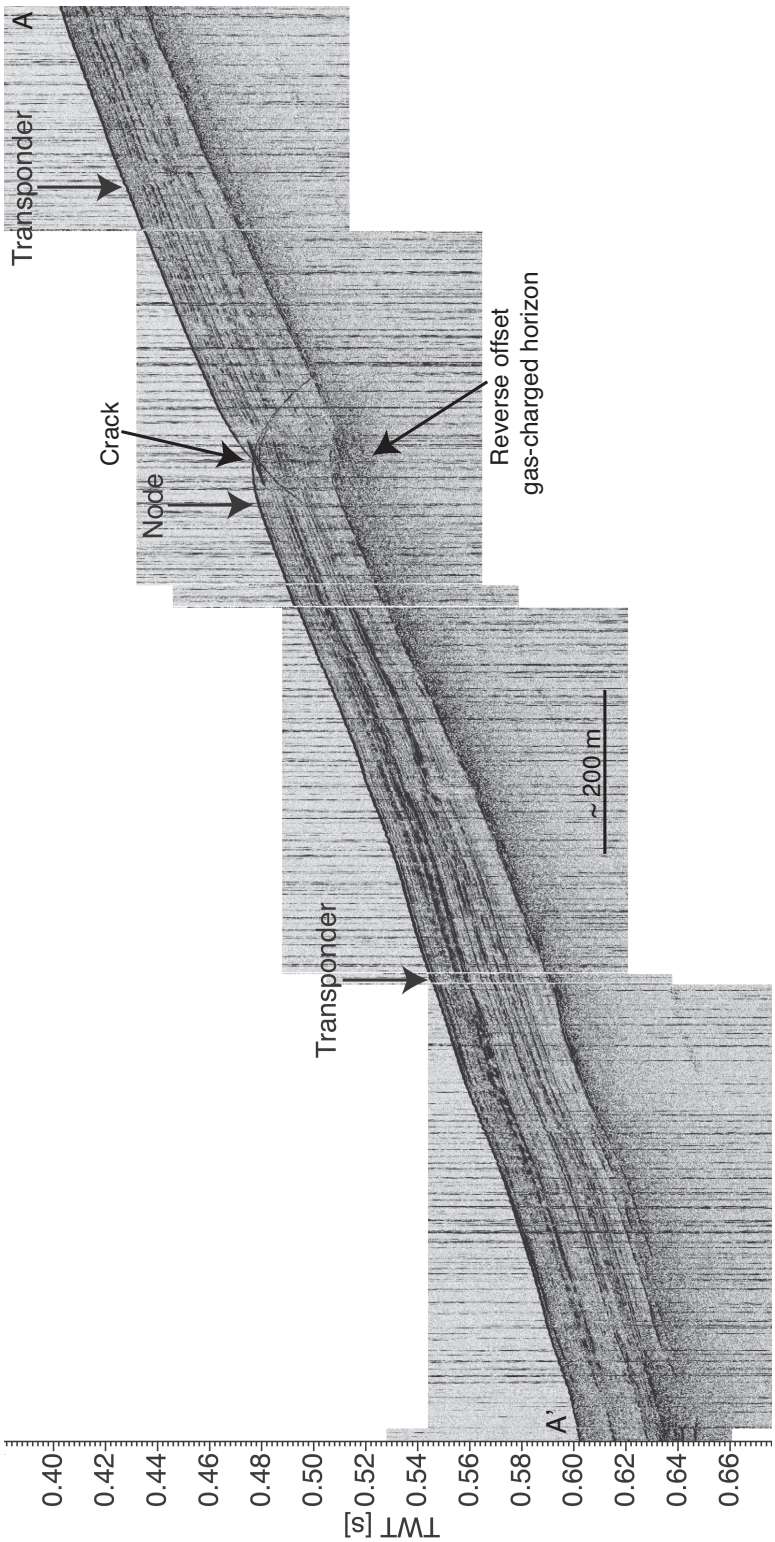

Figure 5.3: CHIRP sub-bottom profile A-A' from Figure 5.2. Mean location of the nodes and transponders are projected onto the line.

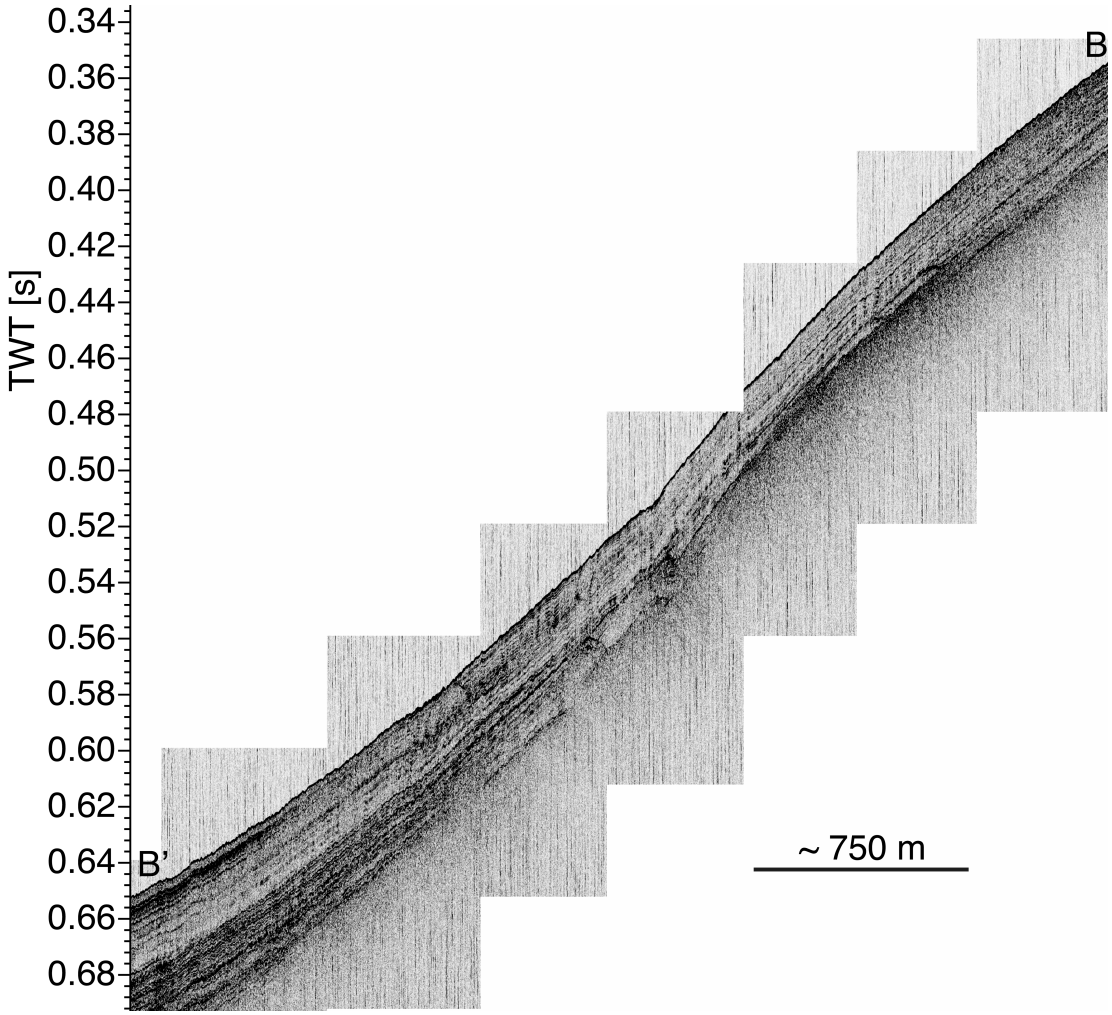

Figure 5.4: CHIRP sub-bottom profile B-B' from Figure 5.2.

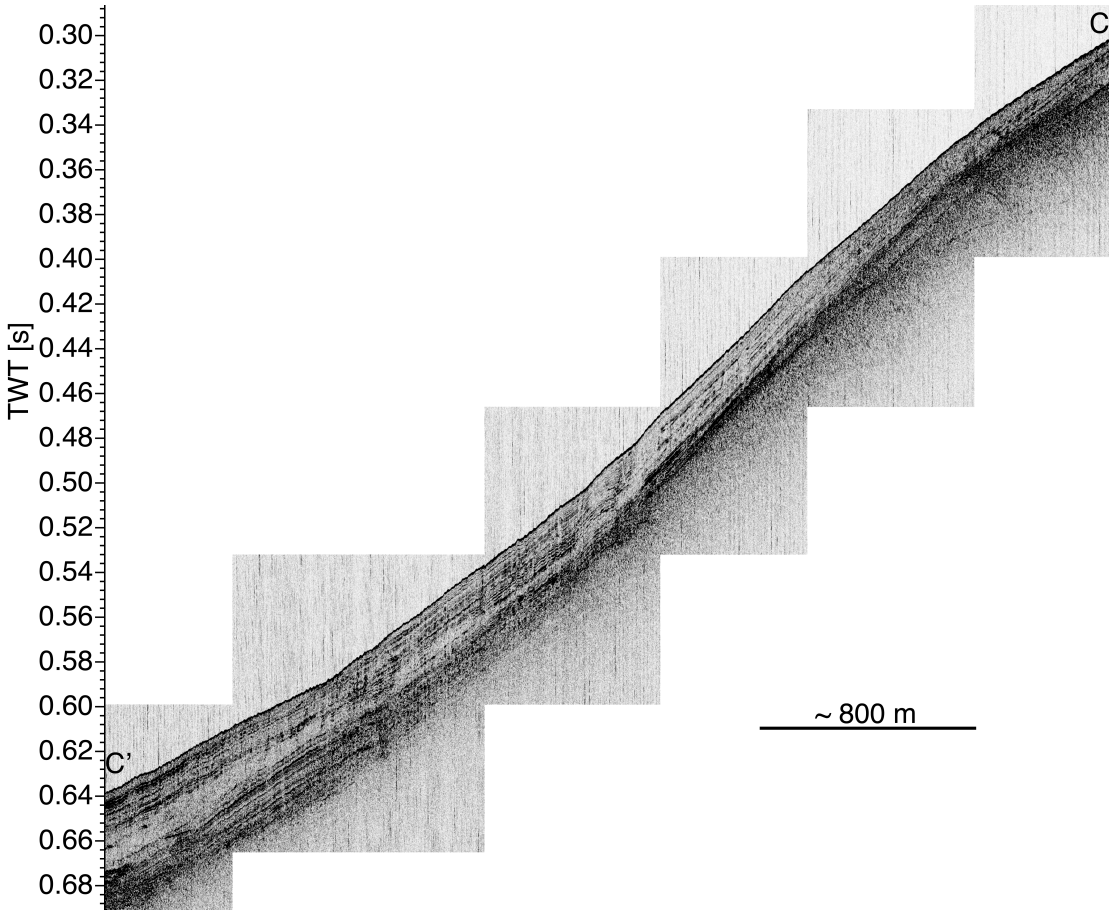

Figure 5.5: CHIRP sub-bottom profile C-C' from Figure 5.2.

removing instrument drift (e.g., Chadwick et al., 2005; Phillips et al., 2008), and providing the desired spatial resolution (e.g., Spiess et al., 1998; Gagnon et al., 2005; Chadwell and Spiess, 2008). The new approach uses acoustic ranging from a network of nodes to a network of transponders. The nodes are small probes, moored to the seabed and floating a few tens-of-meters in the water column, possessing a power source, computer, and clock to function as an autonomous transmitter and recording unit. The nodes act as intermediate tie points that bridge acoustic paths over bathymetric obstructions and depth differences between seafloor transponders. The transponders (PXPs) are markers whose displacement is to be monitored. They receive an acoustic signal from the nodes and automatically re-transmit the received signal back to the node network. In a typical configuration, four PXPs are deployed to form a square that brackets the seafloor feature to be monitored. Three to four nodes are deployed to bisect the square.

The acoustic travel time between the node and PXP is not a direct measure of deformation. The location of each transponder is determined from acoustic travel times using triangulation with the nodes. An illustration of this is shown in Figure 5.6. The ranges from three PXPs uniquely triangulate the position of a node. The range from a fourth PXP slightly over-determines the position and any misfit is information about the difference between the assumed and true positions of the PXPs (Sweeney et al., 2005). Misfit from four-range fixes collected at three or more nodes can be inverted to refine the relative positions of the PXPs. Tracking the change in PXP coordinates over time gives the deformation.

The acoustic geodesy system was deployed adjacent to the Gaviota slide in November 2006. Two PXPs were placed upslope and parallel to the crack ($\approx$ 330 m depth) and two were placed downslope and parallel ($\approx$ 420 m depth), forming a rectangular array with $\approx$ 1000 m N-S and 750 m E-W sides. Four nodes were placed just downslope of the seafloor crack at $\approx$ 375 m depth on 115 m long mooring lines. Three nodes were recovered (Figure 5.7) and redeployed in November 2007 after off loading the data and replacing the batteries. The fourth node did not respond either due to malfunction or loss due to a pre-release. In October 2008, the remaining three nodes and PXPs were recovered after 2 years

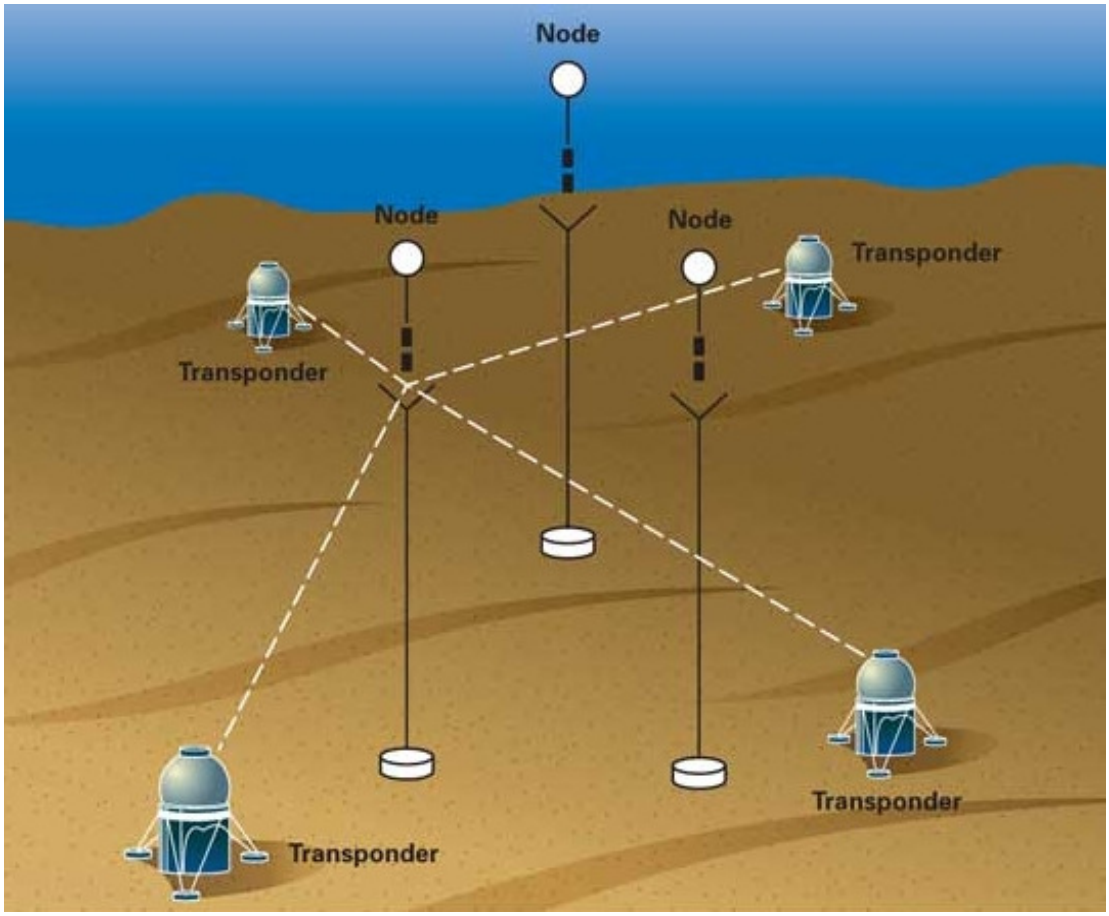

Figure 5.6: Acoustic ranges from transponders triangulate the location of each Node.

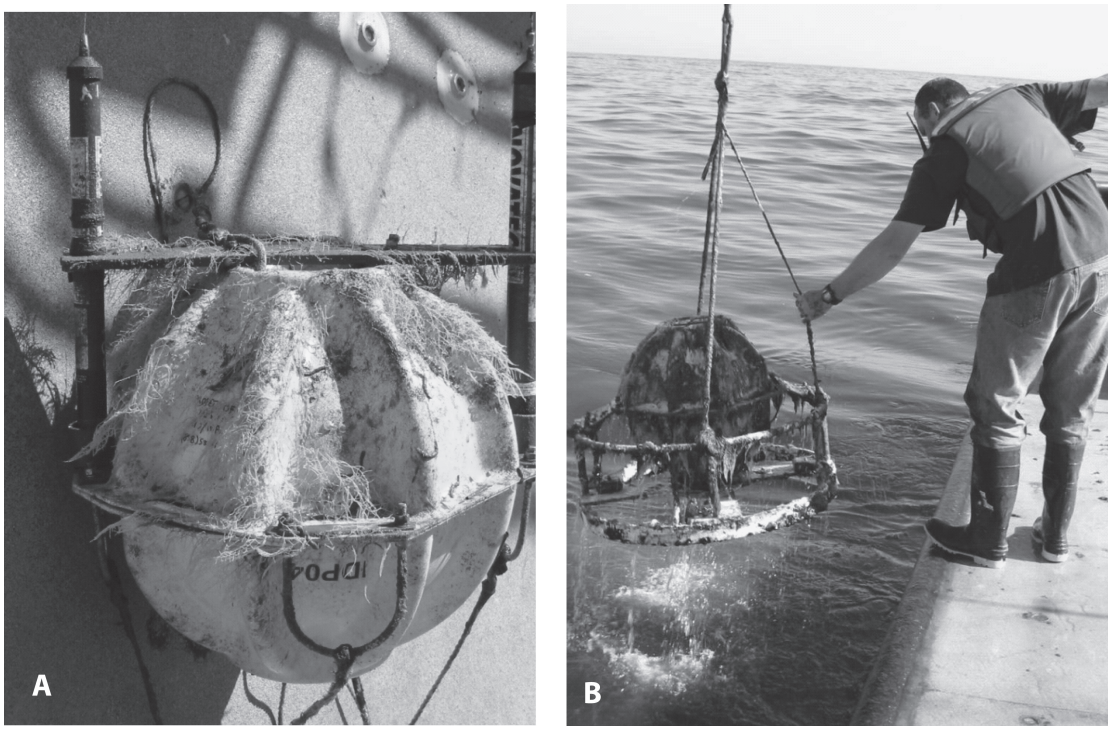

Figure 5.7: A: recovered node. B: recovery of transponder.

of nearly continuous monitoring.

A typical daily measurement session consisted of 20 acoustic interrogations from each of the three nodes to all four PXPs in sequence for a total of 240 range observations with a precision of ± 3 microseconds (a range equivalent of ≈ 3 mm Spiess et al., 1997). Sound speed is measured along a depth profile with a conductivity, temperature, and depth (CTD) sensor during ship visits. Temporal variations between these visits can be estimated from the acoustic travel times by constraining the distance between the two PXPs pairs that are perpendicular to the expected motion and introducing a mean sound speed correction to be estimated in the inversion (Chadwell et al., 1999).

The data were processed to determine for each day the distance between the transponder pairs that straddle the crack (one east and one west). The daily lengths were plotted with the mean removed to examine if any episodic or creep motion occurred (Figure 5.8). The day-to-day RMS repeatability is ± 6.5 mm below the design goal of ± 10 mm. Two artifacts are apparent: a cyclical trend

with an approximate annual period and more scatter in the second year's data. In year one, the nodes were programmed to start their daily interrogation sessions in a sequence where one node followed the next after 15 minutes. The entire set of 60 interrogations took $\approx$ 1 hour and the mean sound speed recovered in the inversion is likely valid over that one hour. Upon redeployment in 2008, one node was incorrectly programmed and the 60 interrogations were spread over $\approx$ 3.5 hours. Here, sound speed variability may not be adequately recovered by a mean estimate. We suggest the long-term trend in the data is due to seasonal motion of the thermocline introducing a small change in the lateral structure of the sound speed field. Our mean sound speed parameterization in the inversion assumes a homogenous bias. We have not estimated lateral sound speed corrections in the inversion because they can absorb real PXP motion.

A linear fit to the data reveals an estimated velocity of -2.4 ± 2.3 mm/yr which is a statistically insignificant contraction. The velocity uncertainty is estimated noting that at present an entire year's data is required to remove the annual signal, the data spans $\approx$ 2 years, and the daily RMS is $\pm$ 6.5 mm/yr (Coates et al., 1985). This result suggests there is no motion exceeding $\pm$ 7mm/yr at the 99% confidence level (3 x 2.3 mm/yr). In the future, lateral variations in sound speed might be captured by a set of continuous self-recording CTD sensors attached to a bottom-moored line deployed at three or more locations within array. Removing the seasonal trends could provide velocity uncertainties approaching $\pm$ 1 mm/yr.

5.4.3 Conclusions

Sub-centimeter repeatability of seafloor positions are viable for the seafloor acoustic ranging system. The absence of internal deformation in the high-resolution CHIRP data, and the lack of an extensional signal in the seafloor acoustic geodetic observations, suggest that there is no active long-term or short-term downslope creep in the margin containing the prominent crack between the Gaviota and Goleta slides. We conclude that the scarp likely formed during an episodic event, which may have been synchronous with the event that caused the Gaviota slide to fail. These results are consistent with geotechnical studies and suggest a lower risk

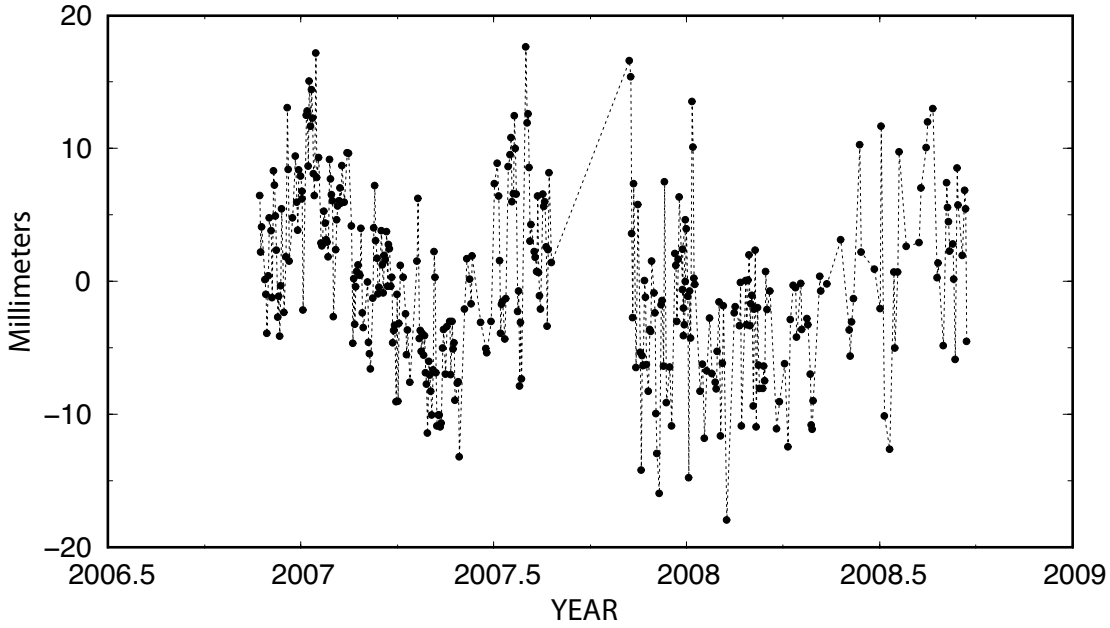

Figure 5.8: Daily lengths of the distance between transponder pairs that straddle the crack with one east and one west. Mean length has been removed.

for imminent failure. The possibility remains, however, that a moderate magnitude earthquake might destabilize the slope beneath the crack given the existing surface expression. Extending estimates of probabilistic seismic hazards to this offshore region and enhanced geotechnical modeling are required to accurately assess the risk. In the next sections of this chapter, we attempt these estimates.

5.5 What triggered failure? Was it the 21 Dec. 1812 Earthquake?

The morphology and absence of deformation across the seafloor crack extending from near the headwall of the Gaviota slide suggests that it possibly formed concomitantly with the event that prompted the Gaviota failure. While seismic acceleration appears to be a necessary trigger, notable uncertainties exist in the slide date as well as the epicenter of the M 7.1 earthquake of 21 December 1812 commonly attributed as its source.

Age estimates of the Gaviota slide are uncertain. For example, using sedi-

ment cores, both Edwards et al. (1995) and Schwehr et al. (2006) noted an abrupt increase in shear strength around 0.5 m depth in sediment cores taken from within the excavation zone of the Gaviota complex, suggesting that sediment below this depth was preloaded by an overlying sediment column removed during the mass wasting. The weaker sediment above that layer is credited to sediment deposition after the event. Greene et al. (2006) also suggests 0.5 m of overlying modern sediment, whereas Duncan et al. (1971) and Schwehr et al. (2006) report 0.15 and 0.23 m, respectively. Recent radiocarbon dating of 1.5-5 m long piston cores suggest sedimentation rates from 0.8 to 1.9 m/ky (Lee et al., 2004). Based upon those sedimentation rates and the dates those cores were collected, the available literature suggests a range of failure dates from 1605 ± 204 to 1837 ± 90. Given the paucity of historical records before 1812 (the Santa Barbara Mission was founded in 1782), it is possible that an earlier, or even later earthquake than the 21 December 1812 event triggered the slide.

Sources outside the Santa Barbara Basin have been argued as the cause of the 21 Dec. 1812 event. One alternate candidate is the San Cayetano Fault. Dolan and Rockwell (2001) examined a trench across this fault and identified a post-1660 rupture of $\approx M$ 7.5. They suggest that it is plausibly the 21 Dec. 1812 event due to its location and large size, indicated by at least 4.3 m of surface slip. Toppozada et al. (2002) rules out this source, arguing that its proximity to a couple of missions would have produced greater damage, and that the orientation of the proposed source with respect to all of the missions in the area is inconsistent with the historically reconstructed Modified Mercali Intensity (MMI) scale values.

Instead, Toppozada et al. (2002) proposes that the 21 Dec. 1812 "Santa Barbara" event should be relocated even further from the basin to the San Andreas fault. A M7.3 event on 8 Dec. 1812 preceded the M7.1 event of 21 Dec. This earlier event was originally thought to be located near San Juan Capistrano (killing 40 people at Catholic mass when a tower fell onto the mission). Jacoby et al. (1988) relocated the event to the San Andreas fault near Wrightwood, based on observations of tree ring data; the rupture damaged root systems that traversed the fault, which affected the character of the annual rings. They estimated an

$\approx$ 170 km rupture length extending southeastward, consistent with the $\approx$ 6 m of offset purported at Pallet Creek (Salyards et al., 1987).

The 8 Dec. 1812 rupture is not well defined, and Toppozada et al. (2002) argues that the $\approx$ 170 km rupture can be split into two segments, the southeastern section representing the 8 Dec. event and the northwestern segment the 21 Dec. earthquake. The relocation of the 21 Dec. event from the Santa Barbara Basin to the San Andreas is based on several arguments, including that historical reports suggesting liquefaction in the San Bernardino Valley as being fictitious (Harley, 1988). Lander et al. (1993) argued that a strictly fault source would need to produce a $\approx M7.7$ earthquake to produce the required tsunami – which Toppozada et al. (2002) argues is not supported by the Modified Mercali Intensities (MMI) of VII observed across the missions – and that the tsunami characteristics are indicative of a submarine landslide source. A similar landslide induced tsunami is purported to have occurred within the Santa Barbara channel on 31 May 1854, coincident with earthquake shaking (Lander et al., 1993).

Assuming a that the earlier, 8 Dec. earthquake occurred on the San Andreas with its rupture terminating at Pallet Creek, Deng and Sykes (1996) calculated the change in the Coulomb failure function. This method calculates the spatial distribution of where there is an increased chance of failure due to the earlier rupture. They note an increased chance of failure extending westward as a lobe, extending from the Pallet Creek rupture termination, across the San Cayetano fault, and into the Santa Barbara Basin. Their conclusion was that the 8 Dec. 1812 rupture increased the likelihood of future failure in the Santa Barbara Basin and produced the 21 Dec. earthquake. Toppozada et al. (2002) notes, however, that their calculated change in Coulomb failure function also shows a greatly increased chance of failure northwest of the rupture termination along the San Andreas fault.

Based on the distribution of damages at missions – some were damaged during both earthquakes but others only on 8 Dec. or 21 Dec. – it is argued that not all of the $\approx$ 170 km rupture occurred during the 8 Dec. event, and that the historical MMI values suggest that the San Andreas fault ruptured in two segments: a 100 km eastern segment on 8 Dec., consistent with a $M7.3$ earthquake; and a 70

km western rupture on 21. Dec., consistent with a $M7.1$ event. Additional support for this argument is the suggestion that the 1812 rupture actually extended over a length up to $\approx$ 200 km (Sieh et al., 1989; Grant, 1996; Arrowsmith et al., 1997), which would require a multiple segment rupture to explain the mission MMI values, as well as a trench across the San Andreas fault with evidence for large 19th century rupture (Lindvall et al., 2002).

In the next sections, we explore each possible fault source: within the Santa Barbara Basin, the San Cayetano Fault, and the San Andreas Fault. For these faults to be responsible for both the 21 December 1812 earthquake and the Gaviota slide, it is necessary that they generate the required ground acceleration to drive slope instability, and they must also sufficiently match the MMI mission records.

5.5.1 Theoretical Critical Ground Acceleration

While 0.12g has been reported as the required value of ground acceleration to drive slope instability, this value represents the empirical horizontal ground acceleration. Recent work (Ingles et al., 2006) using a generalized infinite slope model in which seismic ground acceleration is both normal and tangential to the slope has show that in most cases, a component of vertical upslope motion from the seismic source is non-negligible in determining the critical horizontal seismic acceleration, often known as the PGA (peak ground acceleration). This value is often lower than the PGA estimates that commonly only assume ground acceleration tangential to the slope. We use sediment cores from Schwehr et al. (2006) to calculate the theoretical critical acceleration needed to drive instability from geotechnical properties.

Following Ingles et al. (2006), a block of mass M on a slope may become unstable and slide if subjected to seismic ground acceleration; the seismic acceleration, however, is generally not parallel to the slope. The ratio of vertical to horizontal components of seismic acceleration is defined as

$$\frac{a_{Sv}}{a_{Sh}} = \tan\beta = k_1, \tag{5.1}$$

where β is the angle of seismic acceleration a_S with the horizontal. The vertical

accelerometric parameter k_1 goes as:

- vertical upslope acceleration: $\beta > 0 \Rightarrow k_1 > 0$
- vertical downslope acceleration: $\beta < 0 \Rightarrow k_1 < 0$
- horizontal acceleration only: $\beta = 0 \Rightarrow k_1 = 0$.

Seismic acceleration can be both tangential and normal to the potential slip surface. For downslope acceleration, these components are expressed as

$$a_{St} = a_c(\cos\alpha - k_1 \sin\alpha) \tag{5.2}$$

$$a_{Sn} = a_c(\sin\alpha + k_1 \cos\alpha). \tag{5.3}$$

For upslope acceleration, the tangential and normal components are

$$a_{St} = a_c(\cos\alpha + k_1 \sin\alpha) \tag{5.4}$$

$$a_{Sn} = a_c(\sin\alpha - k_1 \cos\alpha). \tag{5.5}$$

We define the critical seismic acceleration a_c to be horizontal just like the peak ground acceleration (PGA) in the scientific and engineering literature.

During the seismic event, the block M experiences both seismic acceleration and gravitational acceleration on the normal and tangential surfaces. The resulting, total acceleration goes as the sum of those two accelerations, and we have

$$a_{rt} = a_{St} + g\sin\alpha \tag{5.6}$$

$$a_{rn} = a_{sn} - g\cos\alpha. \tag{5.7}$$

There also exists an inertial force with components tangential T and normal N to the slip surface, given as

$$T = Ma_{rt} \tag{5.8}$$

$$N = Ma_{rn} + U, \tag{5.9}$$

where U is the resulting static force from pore water pressure acting normal to the block. The sum of the driving forces (from both seismic and gravitational

acceleration) acting on the block, is thus

$$F_D = T. \tag{5.10}$$

The resisting force F_R is expressed as

$$F_R = N \tan \phi + c' l, \tag{5.11}$$

where c' is the material cohesion and ϕ the internal friction angle.

The pseudo-static factor of safety F is the ratio of the resisting forces to the driving forces,

$$F = \frac{F_R}{F_D}. \tag{5.12}$$

A slope is generally considered unstable when the driving force equals and exceeds the resisting forces, or $F = 1$. In this ratio, we consider the positive values of these forces depending on upslope or downslope acceleration. For downslope acceleration, we have

$$T = M a_{rt}, \tag{5.13}$$

and for upslope acceleration, we have

$$T = -M a_{rt}. \tag{5.14}$$

The normal force goes as

$$N = -M a_{rn} - U. \tag{5.15}$$

Setting the factor of safety $F = 1$, we can go through all the above equations and solve for the critical seismic acceleration a_c needed for instability for the upslope and downslope cases. Because seismic acceleration oscillates between positive and negative values, the critical acceleration occurs at the minimum value for a_c between the upslope and downslope cases for $\pm k_1$.

Our pseudo-static analysis generally ignores dynamic pore-pressure reponses and assumes dynamic shear parameters are the same. We introduce a modified pore-pressure such that $U \rightarrow U + \Delta U$, where ΔU might be an increase in pore pressure from fluids creeping along a fault or other process that precedes a seismic event. It follows that

$$N = -M a_{rn} - (U + \Delta U). \tag{5.16}$$

Setting the factor of safety to one, $F_D = F_R$ and

$$-Ma_{rt} = N \tan\phi + c'l. \tag{5.17}$$

Substituting all the above equations for the upslope case, we solve for the critical seismic acceleration as

$$a_c = \frac{\frac{-(U+\Delta U)\tan\phi + c'l}{M} + g(\sin\alpha + \cos\alpha\tan\phi)}{(\sin\alpha - k_1\cos\alpha)\tan\phi - (\cos\alpha + k_1\sin\alpha)}. \tag{5.18}$$

Similarly, for downslope acceleration we begin with $Ma_{rt} = N\tan\phi + c'l$. Substituting the downslope equations we have

$$a_c = \frac{\frac{-(U+\Delta U)\tan\phi + c'l}{M} - g(\sin\alpha - \cos\alpha\tan\phi)}{(\sin\alpha + k_1\cos\alpha)\tan\phi + (\cos\alpha - k_1\sin\alpha)}. \tag{5.19}$$

Recall that the critical seismic acceleration is the minimum value of a_c for the upslope and downslope cases when varying the seismic parameter between $\pm k_1$. Ingles et al. (2006) demonstrate that in most cases, downslope acceleration with a positive k_1 produces the minimum acceleration needed for instability.

Another interesting problem is to evaluate what pore pressure increase is necessary in order to induce slope instability in the absence of seismic acceleration. Assuming all seismic accelerations are zero, we can solve for $\Delta U/U$ as

$$\frac{\Delta U}{U} = \frac{gM\,(\sin\alpha + \cos\alpha\tan\phi) + c'l}{U\tan\phi} - 1. \tag{5.20}$$

5.5.2 Results from sediment cores

Slope stability is a function of geometry and geotechnical properties of the material, as well as physical processes such as seismic shaking. Geotechnical information is typically obtained from sediment cores. We use geotechnical information from three cores (Schwehr et al., 2006) to examine shallow stability in the study area. The location of the cores and setting are in Table 5.1.

Schwehr et al. (2006) calcluated the weight percent water, η, which we desire to turn into water content w as a proxy for density, ρ. Beginning with

$$\eta = \frac{W_w}{W_w + W_s}, \tag{5.21}$$

Table 5.1: Location of Cores from Schwehr et al. (2006)

Core	Latitude	Longitude	Depth (m)	Length (m)	Slope (°)	Location
C1	34°21′40.2″	−120°06′28.8″	480	1.68	4.4208	Toe
C2	34°22′12.0″	−120°06′27.0″	439	0.73	6.6049	Evacuation Zone
C4	34°22′44.4″	−120°03′25.8″	322	1.25	6.0355	Gullied Ridge

where W is weight and the subscripts w and s denote water and solid. Moisture content goes as

$$w = \frac{W_w}{W_s}, \tag{5.22}$$

and it follows that

$$w = \left(\frac{1}{\frac{1}{\eta} - 1} \right). \tag{5.23}$$

Density is related to moisture content using

$$\rho = \rho_w G_s \left(\frac{1 + w}{1 + w G_s} \right), \tag{5.24}$$

where ρ_w is the density of seawater and G_s is the specific gravity. Common practice is to assume a constant grain specific gravity (see, e.g., Kayen et al., 1999). We use a value of 2.71, roughly the average adjacent to the Gaviota mudflow (Edwards et al., 1995).

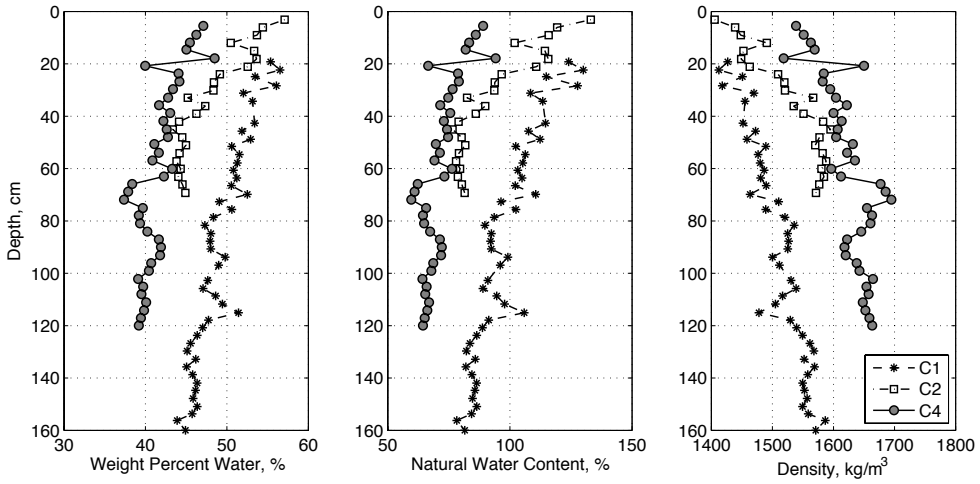

Figure 5.9: Density of shallow cores from Schwehr et al. (2006).

The results are in Figure 5.9. Core 1, located in the toe of the slide, has the greatest water content, possibly because water was entrained during deformation. It also possesses the lowest density. Core 2, in the evacuation zone, has a density more close to Core 1 at the surface, but appears to approach that of Core 4 with depth. Core 4 possesses the lowest water content, the highest density, and therefore a higher shear strength assuming $\tau = \rho g h \tan \phi + C$.

Now that we have derived densities, we can calculate the theoretical critical acceleration as a function of depth within the cores. For the critical acceleration, we use the downslope model with $k_1 = 0.66$, a common value for the ratio of vertical to horizontal seismic acceleration (Newmark and Hall, 1982). We use the actual slopes for each core (Table 5.1) in order to compare the critical acceleration required for instability as we move westward from the Gaviota slide to the eastward gullies.

Figure 5.10 displays our estimated values for critical acceleration for each core. The weakest material near the surface appears to be in Core 2, the evacuated zone of the slide. Core 4 possesses the greatest critical acceleration, approaching 0.12 g at depth – the level calculated by Lee et al. (1991) – on the order of 0.01-0.03 g's greater than the other cores. Greene et al. (2006) suggest that the gullied slope containing Core 4 is likely at a higher risk for failure due to the greater slope gradient. Dingler (2007) argued that the gullies lower slope failure by introducing sediment heterogeneities that inhibit the development of high pore pressures. Our model suggests that the geotechnical properties of the sediments in that region require greater ground acceleration to fail than the region around the Gaviota slide. This might explain why the Gaviota slide failed but the adjacent margin remained intact, and the "bulge" section next to the Goleta complex also remains intact despite its higher slope gradient.

Figure 5.11 shows the results assuming there is no seismic ground acceleration, and we instead are relying on increases in pore pressure to induce slope instability. We find that on the order of a 25-40% increase in pore pressure is required to destabilize the slope in the absence of seismic ground motion. We believe it is unlikely that such an increase could occur without associate seismic shaking driving changes in fluids. Therefore, we agree with the notion that a large earthquake (i.e., $\geq M7$ Edwards et al., 1995) is required for slope failure.

5.5.3 Assessing ground acceleration from possible sources

Using sediment cores, we have verified that around 0.12g is needed to drive slope failure. The question is now whether the three purported seismic sources

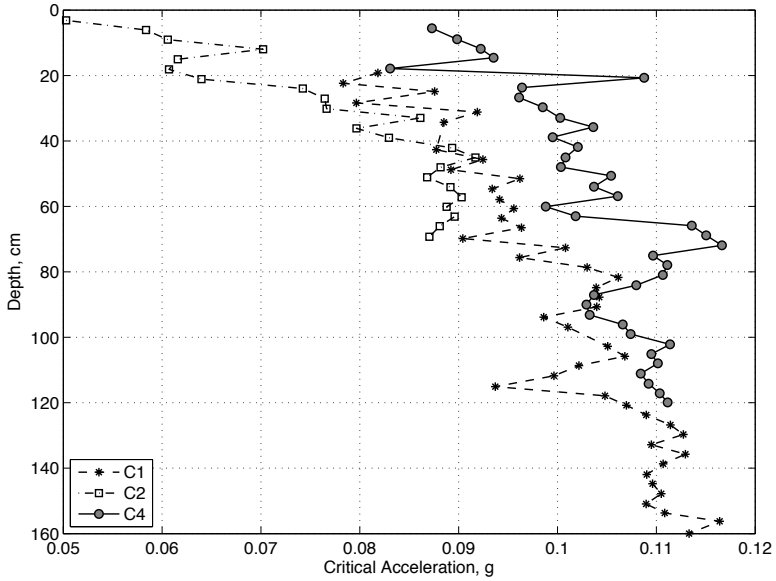

Figure 5.10: Critical acceleration calculated for the shallow cores.

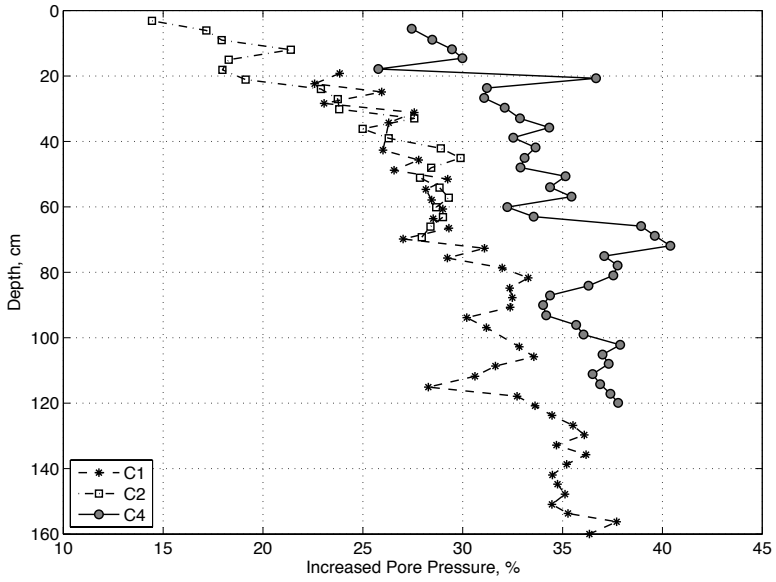

Figure 5.11: Increased pore pressure needed to decrease the factor of safety to 1.

– a fault within the Santa Barbara Basin, the San Cayetano Fault, and the San Andreas Fault – could produce this ground shaking. We note that one of the motivations for relocating the event from the Santa Barbara Basin to the San Andreas fault was the notion that a submarine landslide – arguably the Gaviota slide – was responsible for the observed tsunami, not displacement along a fault. If the earthquake did occur on the San Andreas, it is required that a landslide occur in response to the seismic ground acceleration. The hypothetical seismic sources thus have two constraints: (1) they must reproduce the observed MMI values at the missions; and (2) they must produce ground shaking exceeding 0.12g to induce slope failure.

We test these different scenarios using OpenSHA (Field et al., 2003; OpenSHA, 2009), an open seismic hazard analysis model that inputs seismic sources and outputs expected ground accelerations and MMI values as a function of distance from the source. The model relies on empirical attenuation relationships (e.g., Campbell and Bozorgnia, 2003) as well as local geology and near surface (upper 30m) surface wave velocity to characterize site response (Wills et al., 2000) .

Earthquake source parameters are in Table 5.2. Peak Ground Acceleration (PGA) results as well as MMI values are generated for each source. Figure 5.12 shows the 0.12g PGA contour for each of these sources, as well as the locations of the missions and their historically derived MMI values. Only the Santa Barbara Basin source – and possibly the San Cayetano fault given uncertainties and the absence of fault rupture directivity effects in the OpenSHA model – could produce ground shaking exceeding 0.12g in the vicinity of the landslide complexes. Ground shaking from a San Andreas fault source would be insufficient to drive slope instability and create a landslide generating tsunami. Calculated MMI values were compared to historical values and the sum of squares of the residuals was also calculated for each source (Figure 5.12). The "best fit" is again for a Santa Barbara Basin source, followed by the San Cayetano fault. The San Andreas fault source significantly under-predicts the historical MMI values.

These results are uncertain for offshore areas. Seismic attenuation relationships on land are empirically calibrated; there are no long term observations of

ground accelerations with respect to varying sources (size, focal mechanism, and distance) within the Santa Barbara Basin. Moreover, the model also assumes a constant shear-wave velocity of the upper 30 m of sediment of 180 m/s – a value typical for marine sediments and clays – for offshore areas, but uses varying values on land dependent on surface geology maps. Offshore near-surface shear-wave velocities are not homogeneous, and introducing heterogeneities would likely alter the results. In addition, the effect of basin amplification on the site response within the Santa Barbara Basin is unaccounted and unknown.

We assert that the results of OpenSHA for these sources are therefore inaccurate for predictive purposes, but the relative results between sources are unlikely to be altered. Given the large discrepancy between the San Andreas fault model and the San Cayetano fault and Santa Barbara Basin sources, we argue against a San Andreas fault source. One caveat to that argument is that it assumes the 21 Dec. 1812 earthquake did indeed generate a tsunami or a submarine landslide. If that is not the case – and it is entirely possible that the Gaviota slide failed at an earlier or later date – the possibility of a larger rupture area of 200 km may explain the discrepancy of the MMI results.

Given the unusual sea activity reported to have occured (Lander et al., 1993), however, and the numerous aftershocks in coastal communities (Toppozada and Parke, 1982), it is likely that the earthquake was within the Santa Barbara Basin. Additionally, even the great M_w7.9 earthquake of 1857, which ruptured the San Andreas fault at its closest point to Santa Barbara, was felt with less intensity than the 21 Dec. 1812 event (Agnew and Sieh, 1978). One possible caveat is that a basin source of this size does not guarantee slope instability. The 0.12g threshold is a necessary but not a sufficient condition, as material must displace a certain distance – typically due to the duration of shaking at some critical level – before catastrophically failing (see, e.g., Jibson, 1993; Ingles et al., 2006). A basin source is likely required to drive instability, but the Gaviota slide may be from a different event given the uncertainty in its date.

Table 5.2: 21 Dec. 1812 seismic sources used in the OpenSHA model.

Source	Lat	Lon	M	Rake	Dip
San Andreas Fault	34.75	-118.6	7.1	180	90
San Cayetano Fault	34.411	-118.754	7.5	90	60
Santa Barbara Basin	34.2	-119.9	7.1	90	24.33

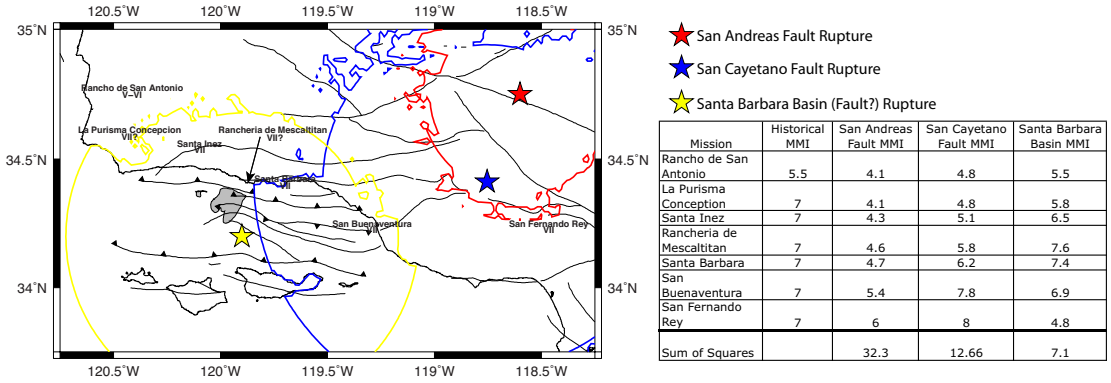

Mission	Historical MMI	San Andreas Fault MMI	San Cayetano Fault MMI	Santa Barbara Basin MMI
Rancho de San Antonio	5.5	4.1	4.8	5.5
La Purisma Conception	7	4.1	4.8	5.8
Santa Inez	7	4.3	5.1	6.5
Rancheria de Mescaltitan	7	4.6	5.8	7.6
Santa Barbara	7	4.7	6.2	7.4
San Buenaventura	7	5.4	7.8	6.9
San Fernando Rey	7	6	8	4.8
Sum of Squares		32.3	12.66	7.1

Figure 5.12: The 0.12g peak ground acceleration contour from the OpenSHA model for hypothetical 21 Dec. 1812 sources along the San Andreas Fault, San Cayetano Fault, and in the Santa Barbara Basin. Historical MMI values at missions are from (Toppozada et al., 2002). The table on the lower right contains the historical MMI values and the results from OpenSHA, as well as the sum of squares of the residuals between the modeled and historical values.

5.6 Conclusions

Based on the high-resolution CHIRP data, GPS velocities, and acoustic seafloor positioning, we observe no indicators of long-term or short-term downslope creep in the gullied margin containing the prominent crack between the Gaviota and Goleta slides. This evidence suggests that the scarp likely formed during an episodic event, potentially the same event that prompted the Gaviota slide failure, though it is possible that the feature is from a subsequent earthquake but did not displace a great enough distance from the seismic accelerations to exceeded its failure strength and catastrophically fail.

Sub-centimeter and near millimeter repeatability of seafloor positions are viable for the acoustic geodesy and fiber optic seafloor strainmeter systems, respectively. In the case of the optical fiber system, a remotely operated vehicle is likely needed to deploy the cable given the sensitive cable breaking strength ($\approx$ 100 lbs). Use of these systems, and the ability to integrate an AUV into the acoustic network (see, e.g., Kussat et al., 2005) can allow for decimeter precision translations over kilometers, which is highly applicable for repeat mapping surveys.

Our assessment of potential earthquake sources for the 21 Dec. 1812 event suggests a basin source. Moreover, a basin source of $M > 7$ is likely required to produce ground accelerations significant in intensity and duration to induce slope instability. This suggests that the lack of observable downslope deformation reduces the imminence of mass wasting and tsunami hazard in the region, as a more large earthquake may be required to induce instability than if downslope deformation were actively occurring. Characterization of geohazards in this region therefore depends on characterizing the fault and earthquake history within the basin, and probabilistic hazard assessment should be extended offshore, incorporating spatially varying seabed sediment properties and basin amplification effects.

5.7 Acknowledgements

We thank BP America, Inc. for initiating and funding this project, Richard Zimmerman, David Price, and Dennis Rimington at the Marine Physical Laboratory (SIO) for their assistance in developing and deploying the optical

fiber and acoustic geodesy systems, and Gary Greene for stimulating discussion on this region. We also thank the Captains and crew of the R/V Roger Revelle and Robert Gordon Sproul.

Much of the work in this chapter has been published as: **Blum, J.A., Chadwell, C., Driscoll, N., and Zumberge, M., 2010: Assessing slope stability in the Santa Barbara Basin using seafloor geodesy and CHIRP seismic data.** ***Geophysical Research Letters*****, doi:10.1029/2010GL043293**. The author is responsible for writing the published manuscript and collecting and interpreting all data. Dave Chadwell designed and processed the acoustic geodesy survey and data. Neal Driscoll was responsible for designing and collecting the CHIRP seismic survey data. The author of this dissertation processed and interpreted the seismic and bathymetry data and is additionally responsible for the entire discussion on earthquake relocation and slope stability.

REFERENCES

Agnew, D., and Sieh, K., 1978: A documentary study of the felt effects of the great California earthquake of 1857. *Bulletin of the Seismological Society of America*, **68**, 1717–1729.

Arrowsmith, R., McNally, K., and Davis, J., 1997: Potential for earthquake rupture and M7 earthquakes along the Parkfield, Cholame, and Carizo segments of the San Andreas Fault. *Seism. Res. Lett.*, **68**, 902–916.

Blum, J., Nooner, S., and Zumberge, M., 2008: Recording Earth strain with optical fibers. *IEEE Sensors Journal*, **8**, 1152–1160.

Borrero, J., Dolan, J., and Synolakis, C., 2001: Tsunamis within the eastern Santa Barbara Channel. *Geophysical Research Letters*, **28**(4), 634–646.

Campbell, K., and Bozorgnia, Y., 2003: Updated near-source ground-motion (attenuation) relations for the horizontal and vertical components of peak ground acceleration and acceleration response spectra. *Bulletin of the Seismological Society of America*, **93**, 314–331.

Canals, M., Lastras, G., Urgeles, R., Casamor, J., Mienert, J., Cattaneo, A., Batist, M. D., Haflidason, H., Imbo, Y., Laberg, J., Locat, J., Long, D., Longva, O., Masson, D., Sultan, N., Trincardi, F., and Bryn, P., 2004: Slope failure dynamics and impacts from seafloor and shallow sub-seafloor geophysical data: case studies from the COSTA project. *Marine Geology*, **213**, 9–72.

Chadwell, C., Hildebrand, J., Spiess, F., Morton, J., Normark, W., and Reiss, C., 1999: No spreading across the southern Juan de Fuca Ridge axial cleft during 1994-1996. *Geophys. Res. Lett.*, **26**, 2525–2528.

Chadwell, C., and Spiess, F., 2008: Plate motion at the ridge-transform boundary of the south Cleft segment of the Juan de Fuca Ridge from GPS-Acoustic data. *J. Geophys. Res.*, **113**, 10.1029/2007JB004936.

Chadwick, W., Nooner, S., Zumberge, M., Embley, R., and Fox, C., 2005: Vertical deformation monitoring at Axial seamount since its 1998 eruption using deep-

sea pressure sensors. *Journal of Volcanology and Geothermal Research*, **150**, 313–327.

Coates, R., Frey, H., Mead, G., and Bosworth, J., 1985: Space-age geodesy: the NASA crustal dynamics project. *IEEE Transactions on Geosciences and Remote Sensing*, **GE-23**(4), 360–368.

Corbett, E., and Johnson, C., 1982: The Santa Barbara, California, earthquake of 13 August 1978. *Bulletin of the Seismological Society of America*, **72**, 2201–2226.

Deng, J., and Sykes, L., 1996: Triggering of 1812 Santa Barbara earthquake by a great San Andreas shock: implications for future seismic hazards in southern California. *Geophys. Res. Lett.*, **23**(10), 1155–1158.

Dingler, J., 2007: *New geophysical approaches to study neotectonics and associated geohazards*. Ph.D. thesis, University of California San Diego: Scripps Institution of Oceanography.

Dolan, J., and Rockwell, T., 2001: Paleoseismic evidence for a very large $M_w > 7$, post-A.D. 1660 surface rupture on the Eastern San Cayetano fault, Venture County, California: was this the elusive source of the damaging 21 December 1812 earthquake? *Bulletin of the Seismological Society of America*, **91**(6), 1417–1432.

Duncan, J., Hoover, R., Pflum, C., Widmier, J., and Daetwyler, C., 1971: Near-surface geology of the Santa Ynez unit, Santa Barbara, California. Technical report, Esso Production Research Company.

Edwards, B., Lee, H., and Field, M., 1995: Mudflow generated by retrogressive slope failure, Santa Barbara Basin, California Continental Borderland. *Journal of Sedimentary Research*, **A65**, 57–68.

Eichhubl, P., Greene, H., and Maher, N., 2002: Physiography of an active transpressive margin basin: high-resolution bathymetry of the Santa Barbara basin, Southern California continental borderland. *Marine Geology*, **184**, 95–120.

Field, E., Jordan, T., and Cornell, C., 2003: OpenSHA: a developing community-modeling environment for seismic hazard analysis. *Seism. Res. Lett.*, **74**(4), 406–419.

Fisher, M., Normark, W., Greene, H., Lee, H., and Sliter, R., 2005: Geology and tsunamigenic potential of submarine landslides in Santa Barbara channel, Southern California. *Marine Geology*, **224**, 1–22.

Gagnon, K., Chadwell, C., and Norabuena, E., 2005: Measuring the onset of locking in the Peru-Chile trench with GPS and acoustic measurements. *Nature*, **434**, 205–208.

Grant, L., 1996: Uncharacteristic earthquakes on the San Andreas fault. *Science*, **272**, 826–827.

Greene, H., Murai, L., Watts, P., Maher, N., Fisher, M., Paull, C., and Eichhubl, P., 2006: Submarine landslides in the Santa Barbara Channel as potential tsunami sources. *Natural Hazards and Earth System Sciences*, **6**, 63–88.

Harley, R., 1988: Rev. Juan Caballeria: historian or storyteller? Rethinking the 1810 Dumetz expedition: Redlands, Calif. *San Bernardino County Museum Association Quarterly*, **35**, 42.

Hill, J., Driscoll, N., Weissel, J., and Goff, J., 2004: Large-scale elongated gas blowout along the U.S. Atlantic margin. *J. Geophys. Res.*, **109**, 1–14.

Ingles, J., Darrozes, J., and Soula, J., 2006: Effects of the vertical component of ground shaking on earthquake-induced landslide displacement using generalized Newmark analysis. *Engineering Geology*, **86**, 134–147.

Jacoby, G., Sheppard, P., and Sieh, K., 1988: Irregular recurrence of large earthquakes along the San Andreas fault: evidence from trees. *Science*, **241**, 196–199.

Jibson, R., 1993: Predicting earthquake-induced landslide displacement using Newmark's sliding block analysis. *Transportation Research Record*, **1411**, 9–17.

Kayen, R., Edwards, B., and Lee, H., 1999: *Nondestructive laboratory measurement of geotechnical and geoacoustic properties through intact core-liner*, volume 1350 of *ASTM STP*. American Society for Testing and Materials, West Conshohocken, PA.

Kussat, N., Chadwell, C., and Zimmerman, R., 2005: Absolute positioning of an autonomous underwater vehicle using GPS and acoustic measurement. *IEEE. J. Oceanic Engineering*, **30**, 153–164.

Lander, H., Lockridge, P., and Kozuch, M., 1993: *Tsunamis affecting the west coast of the United State 1806-1992*, volume 242 of *NGDS Key to Geophysical Records Doc. No. 29*. U.S. Dept. of Commerce.

Lee, H., and Edwards, B., 1986: Regional method to assess offshore slope stability. *Journal of Geotecnical Engineering*, **112**, 489–509.

Lee, H., Normark, W., Fisher, M., Greene, H., Edwards, B., and Locat, J., 2004: Timing and extent of submarine landslides in Southern California. 16744. Offshore Technology Conference, Houston Texas.

Lee, H., Schwab, W., Edwards, B., and Kayen, R., 1991: Quantitative controls on submarine slope failure morphology. *Marine Geotechnology*, **10**, 489–509.

Lindvall, S., Rockwell, T., Dawson, T., Helms, J., and Weaver, K., 2002: Timing of the penultimate large earthquake on the San Andreas fault at Frazier Mountain, California. *Bulletin of the Seismological Society of America*, **92**(7), 2689–2703.

Martel, S., 2004: Mechanics of landslide initiation as a shear fracture phenomenon. *Marine Geology*, **203**, 319–339.

Masson, D., Harbitz, C., Wynn, R., Perderen, G., and Lovholt, F., 2006: Submarine landslides: processes, triggers, and hazard prediction. *Philosophical Transactions of the Royal Society A*, **364**, 2009–2039.

Miller, R., 1979: The Santa Barbara, California, earthquake of 13 August 1978. *Earthquake Engineering & Structural Dynamics*, **7**, 491–506.

Newman, K., Cormier, M.-H., Weissel, J., Driscoll, N., Kastner, M., Solomon, E., Robertson, G., Hill, J., Singh, H., Camilli, R., and Eustice, R., 2007: Active methane venting observed at giant seafloor pockmarks along the U.S. mid-Atlantic shelf break. *Earth and Planet. Sci. Lett.*, **267**, 341–352.

Newmark, N., and Hall, W., 1982: *Earthquake spectra and design.* Earthquake Engineering Research Institute, Berkeley, CA.

O'Leary, D., and Laine, E., 1996: Proposed criteria for recongizing intrastratal deformation features in marine high resolution seismic reflection profiles. *Geo-Marine Letters*, **16**, 305–312.

OpenSHA, 2009: Open Seismic Hazard Analysis.

Phillips, K., Chadwell, C., and Hildebrand, J., 2008: Vertical deformation measurements on the submerged south flank of Kilauea volcano, Hawaii reveal seafloor motion assoicated with volcanic collapse. *J. Geophys. Res.*, **113**, 10.1029/2007JB005124.

Salyards, S., Sieh, K., and Kirshvink, J., 1987: Paleomagnetic measurement of dextral warping during the past three large earthquakes at Pallet Creek, southern California. *Geol. Soc. Am. Abstr. Programs*, **19**(7), 828.

Schwehr, K., Tauxe, L., Driscoll, N., and Lee, H., 2006: Detecting compaction disequilibrium with anisotropy of magnetic susceptibility. *Geochemistry Geophysics Geosystems*, **7**.

Sieh, K., Stuiver, M., and Brillinger, D., 1989: A more precise chronology of earthquakes produced by the San Andreas Fault in southern California. *J. Geophys. Res.*, **94**, 603–623.

Spiess, F., Boegeman, D., Zimmerman, R., Chadwell, C., and Hildebrand, J., 1997: SIO Precision Transponder. SIO Technical Report 97-3, Univ. of Calif., Scripps Institution of Oceanography.

Spiess, F., Chadwell, C., Hildebrand, J., Young, L., Jr., G. P., and Dragert, H., 1998: Precise GPS/Acoustic positioning of seafloor reference points for tectonic studies. *Phys. Earth Planet. Inter.*, **108**, 101–112.

Sweeney, A., Chadwell, C., Hildebrand, J., and Spiess, F., 2005: Centimeter-level positioning of seafloor acoustic transponders from a deeply-towed interrogator. *Marine Geodesy*, **28**, 39–70.

Toppozada, T., and Branum, D., 2004: California earthquake history. *Annals of Geophysics*, **47**, 509–522.

Toppozada, T., Branum, D., Petersen, M., Hallstrom, C., Cramer, C., and Reichle, M., 2000: Epicenters of and areas damaged by $M \geq 5.5$ California Earthquakes, 1800-1999. Map sheet 49, California Division of Mines and Geology.

Toppozada, T., Branum, D., Reichle, M., and Hallstrom, C., 2002: San Andreas Fault Zone, California: $M \geq 5.5$ earthquake history. *Bulletin of the Seismological Society of America*, **92**, 2555–2601.

Toppozada, T., and Parke, D., 1982: Areas damaged by California earthquakes, 1900-1949. Open File Report 82-11, California Division of Mines and Geology.

Wills, C., Petersen, M., Bryant, W., Reichle, M., Saucedo, G., Tan, S., Taylor, G., and Treiman, J., 2000: A site-conditions map for California based on geology and shear-wave velocity. *Bulletin of the Seismological Society of America*, **90**(6b), 5187–5208.

Chapter 6

The M_S 5.3 Green Canyon (northern Gulf of Mexico) earthquake of 10 February 2006: a landslide source?

6.1 Abstract

We study the anomalous M_s 5.3 earthquake of 10 February 2006 in the Green Canyon district in the Gulf of Mexico. The earthquake is relatively depleted in high frequency body wave energy with respect to surface wave energy. Surface wave full-waveform inversion produced a best fit by either a model of a shallow landslide translating on a low angle subsurface plane, or sub-horizontal or vertical faulting within shallow low velocity sediments (Nettles, 2007). The location from the surface wave inversion differed significantly from the USGS location obtained using first arrival P-waves. To relocate the epicenter, we integrated the results of two seismic exploration surveys – including over 500 four-component ocean bottom seismic nodes from the Atlantis OBS survey, operated by BP in partnership with BHP Billiton Limited – and the CGG Green Canyon phase VIII multi-client towed streamer survey (Courtesy CGGVeritas, Houston, Texas). The relocation

is consistent with the sliding source model, and geotechnical modeling suggests that the sharp bathymetric relief is capable of supplying a large landslide. To test the landslide hypothesis, we performed a multibeam, sidescan, and sub-bottom seismic profile survey in October, 2008. The results of that survey indicate no evidence of a large debris flow. This suggests a source mechanism within the shallow sedimentary section on either a near sub-horizontal or near vertical plane.

6.2 Introduction

A series of earthquakes in 2006 has led to a reevaluation of the seismic hazards and tectonic activity in the northern Gulf of Mexico (GoM): a M_s 5.3 event on 10 February, which we refer to as the Green Canyon event; a M_s 4.6 event on 18 April; and a M_w 5.8 event on 10 September. Figures 6.1 and 6.2 show the locations of these events in the context of regional seismicity and geology. These earthquakes were the largest in the region since a well studied M 5.0 event on 24 July,1978 (Frohlich, 1982). Significant offshore development – including pipelines, communication cables, and production platforms – has occurred since that 1978 event. The proximity of the first two earthquakes in 2006 to active and potential hydrocarbon leases generated interest within the oil and gas industry in the form of special workshops at the annual Offshore Technology Conference and meeting of the Society of Exploration Geophysicists. Understanding the causes and consequences of these events is critical for managing risks to infrastructure, economy, and environment.

Despite immense understanding of the GoM geologic history due to hydrocarbon exploration (Salvador, 1991; Bird et al., 2005), the paucity of seismicity in the northern and central segments has led to little research on the tectonics and seismic potential of the region. The sparse intraplate events that do occur are generally attributed to sediment loading (Frohlich, 1982; Nunn, 1985). Whether the GoM is tectonically active today is an active topic of debate (Sarwar, 2002; Dokka, 2006).

The northern GoM is currently designated as a Zone 0 seismic risk area

(API, 2000b,a), meaning that the maximum expected horizontal ground motion from possible earthquakes is less than 0.05g. While Zone 0 attribution does not account for the occurrence of earthquakes with $M > 5.5$, the magnitude at which surface rupture becomes common (Wells and Coppersmith, 1994), industry employs best practice hazard analysis from regions with greater seismic activity (Angell and Hitchcock, 2007), and subsea structures in the Gulf of Mexico are considered to be within the design limits for up to Zone 2 ground accelerations (0.2g, Brown et al., 2003). The earthquakes of 2006, however, suggest the need to update our assumptions on the frequency and magnitude of seismic activity within the region. (Angell and Hitchcock, 2007).

In this study, we examine potential source mechanisms for the M_s 5.3 Green Canyon event of 10 February, 2006. We use industrial seismic data to revise the epicenter's location and we test various source hypotheses consistent with local geology. Ultimately, we present the results of a geophysical survey (bathymetry, sidescan sonar, and sub-bottom profiling) of the epicentral region to assess the cause of the event and associated hazards.

6.3 Geologic Background

6.3.1 GoM Seismicity

Historically, the best studied and best recorded earthquake in the GoM is the M 5.0 earthquake on 24, July 1978. Frohlich (1982) located the event near the edge of the Mississippi fan and estimated a source depth of 15 km, roughly the depth of the Moho in the region. The observed ground motions at stations along the Gulf Coast indicated reverse faulting. The hypocenter locations, combined with calculations of sediment-stress accumulation, suggested that the source was related to downwarping of the lithosphere due to sediment loading from the Mississippi River. Nunn (1985) confirmed that the high rate of sedimentation along the Gulf Coast since the Pleistocene could create enough load to generate bending and produce horizontal extension and normal faulting. A thrust mechanism was also suggested using Mohr's circle analysis (Talwani and Rajendran, 1991).

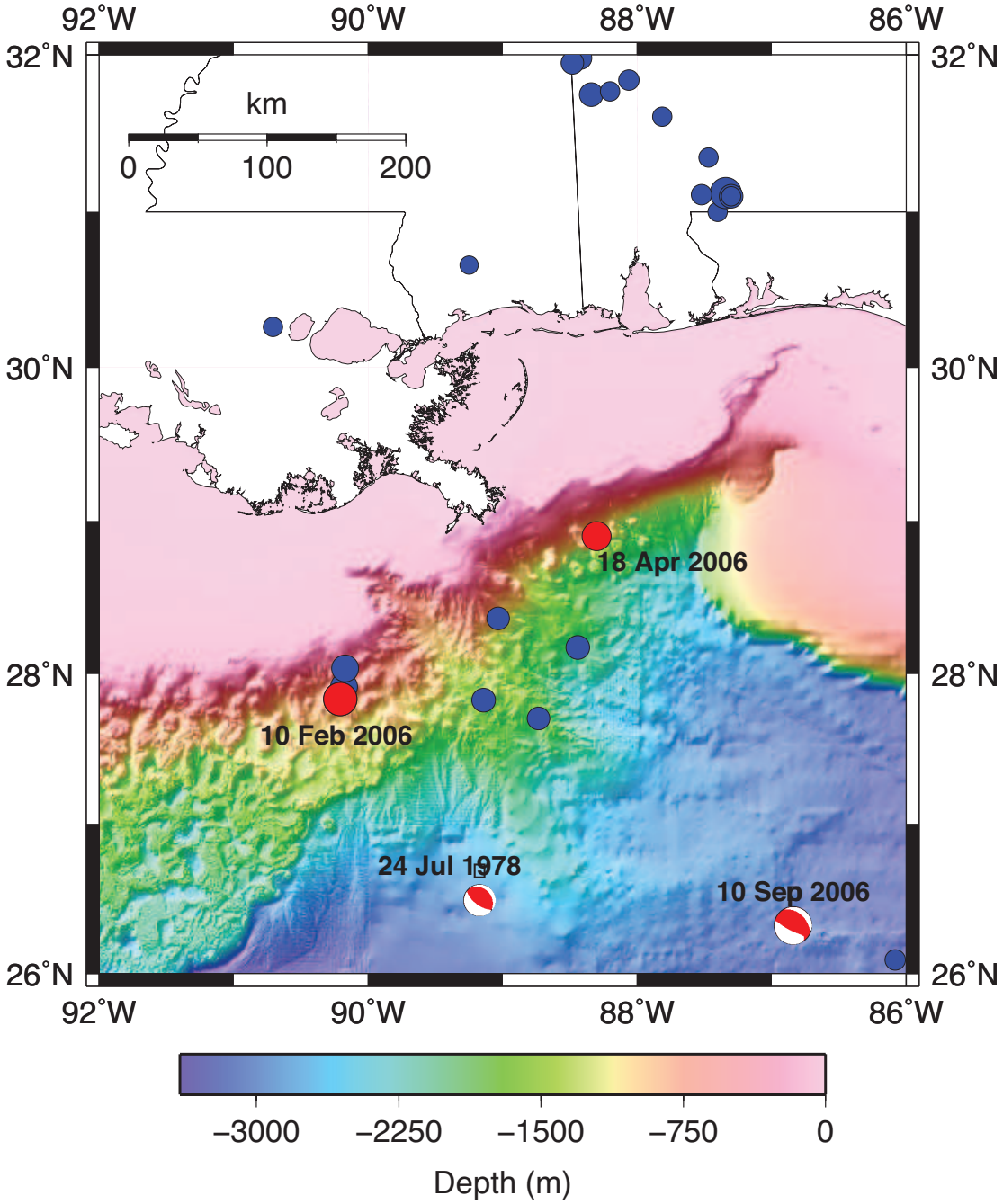

Figure 6.1: Northern Gulf of Mexico seismicity between 1973 and 2008. Earthquakes are taken from the U.S. Geological Survey's National Earthquake Information Center catalog. The 18 Apr. 2006 event is not in the catalog and was detected using surface waves (Nettles, 2007)

.

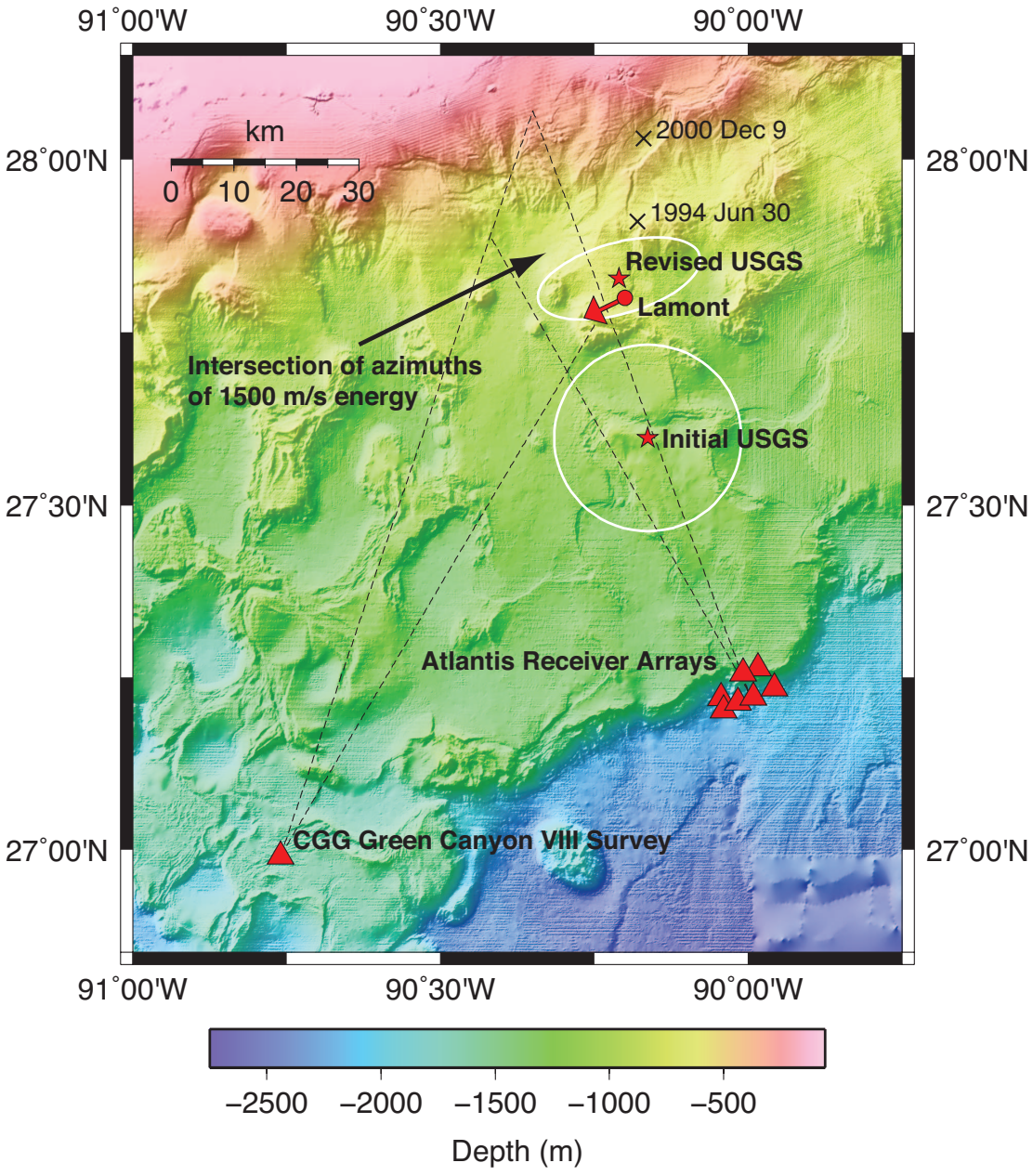

Figure 6.2: Regional map showing the initial and revised earthquake locations as well as the receivers used to update the epicenter. The intersection of azimuth lines coming from the CGG Green Canyon VIII survey (Courtesy CGGVeritas, Houston, Texas) and Atlantis receiver arrays provide independent information on the possible location. They assume a P-wave water velocity of 1500 m/s and represent the azimuthal uncertainty in which energy arrives. The intersection of those lines in the western portion of the error ellipse suggests that the event is more likely to occur in that region.

While downwarping from sediment loading has been considered the dominant source of seismicity, it is certainly not the cause of every earthquake. Gangopadhyay and Sen (2008) used 2-D and 3-D distinct element models to examine stress concentrations due to contrasts in the mechanical properties between salt deposits and surrounding sediments in the northern GoM. They surrounded a simplified salt body with sediments and assigned mechanical properties based on geologic interpretations and seismic velocities. After tectonically loading the model for a year, they discovered that regions of relatively high shear stress correlate with the spatial distribution of seismicity along the boundary of the salt canopy. This suggested that a causal tectonic association, not aseismic sediment loading, could be responsible for observed seismic activity.

Regardless of dominant mechanisms and the general absence of tectonics, significant faulting does exist throughout the sedimentary column in the form of shallow gravity driven listric faults along salt boundaries (Angell and Hitchcock, 2007). Sections of salt interrupt the thick (5-14 km) sedimentary column in the GoM. Due to the weak mechanical properties of salt with respect to the overlying sediments, the rapid sediment accumulation results in the salt behaving plastically, forming diapirs and canopies. Basinward gravitational movement of sediment along these salt boundaries results in upslope extension and downdip compression, producing a series of concave up listric growth faults reminiscent of slump blocks.

6.3.2 Green Canyon

The Green Canyon region of the GoM is a designated MMS protraction area beginning roughly midway between the present day shelf edge and terminating just past the base of the Sigsbee escarpment. Salt withdrawal basins and salt domes and diapirs dominate the seafloor topography, resulting in pocketed areas of sharp relief and basins of smooth, shallow slopes.

Peel (2007) describes the local structural setting that may contain the seismic source. The earthquake epicenter lies close to a step in the depth to the basement. A change in regional magnetics corresponds to this step, and it is thought to represent a stretched crustal transition between oceanic and continental crust.

Above the change in basement lies a change in deep salt; directly atop the continental basement sits autochthonous Louann salt, whereas the salt atop the oceanic section is an allochthonous nappe unfurled throughout younger Jurassic and Cretaceous stratigraphy. A folded unit from the Jurassic to Upper Miocene overlies the deep salt. Plastered above the folded unit is the Sigsbee Salt Nappe, a major allochthonous salt canopy that spread by large-scale glacier-like flow from NNW – with a large basal shear zone – from the middle Miocene to Early pliocene, with some salt still spreading in the present day. A carapace of more recent sediment rests atop the Sigsbee salt, punctuated by withdrawal basins that have subsided to produce significant sediment-sediment interfaces known as welds. The lower part of the sediment carapace exhibits compressional folding and small-scale thrusting.

6.3.3 Possible Source Mechanisms

Numerous potential source mechanisms were initially suggested, including faulting at the basement transition, sediment-salt slip along the deep salt nappe, movement along a weld at the base of the Sigsbee salt, a surge of salt movement within the Sigsbee salt, shallow faulting in the overlying sediments, a large scale landslide or seafloor slumping, and large-scale sediment redistribution from recent Hurricanes (see, e.g., Walsh et al., 2006) redistributing stress. Not all of these mechanisms proved to be consistent with the location and seismological characteristics discussed in the next section. A schematic showing some of these sources is in Figure 6.3.

The Society of Exploration Geophysicists dedicated a special workshop at its 2006 annual meeting to the Green Canyon event, and while no consensus was reached amongst attendants, the following three mechanisms were widely considered. (1) Faulting within crystalline basement in the transitional region. This may be the result of intraplate stress, loading from sediment or an advancing salt nappe, differential thermal subsidence, or differential isostatic subsidence. (2) A shallow earthquake within the sedimentary cover. (3) A large undersea landslide. In the remainder of this paper, we review these scenarios by constraining the earthquake's location using additional industrial data, and by integrating geotechnical

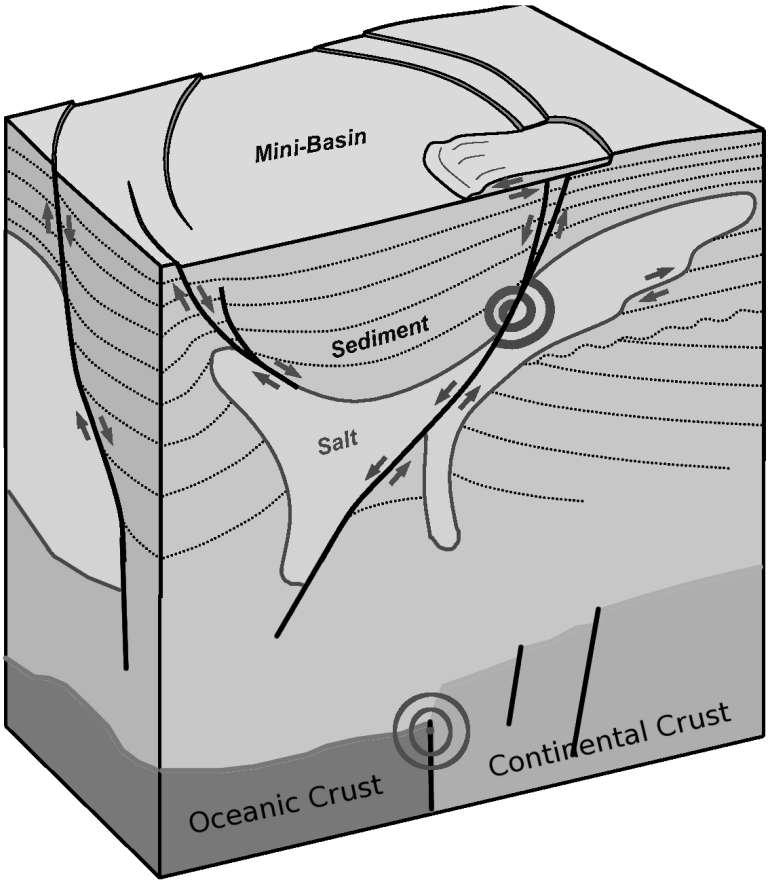

Figure 6.3: Hypothetical mini-basin displaying potential source mechanisms, including: shallow slumping or landslides; shallow sediment-sediment slip; slip along the salt-sediment interface; salt-salt slip or salt tectonics; movement along the weak boundary at the transition between oceanic and continental crust. Not all sources are consistent with the observed seismic characteristics. Modified from an initial figure courtesy of Rich Weiland, BP.

modeling with the results of a hydrographic and geophysical survey.

6.4 Seismic Characteristics

The Green Canyon event was detected by the National Earthquake Information Center (NEIC) of the U.S Geological Survey (USGS) using traditional P-wave arrival methods (Dewey and Dellinger, 2008). It was estimated to have occurred on 10 February, 2006 at 04:14:17.8 UTM (HH:MM:SS) with a hypocenter at 27.828° N, 90.210° W and at a depth less than 5 km, with magnitudes m_b =

Table 6.1: Green Canyon epicenter locations. The revised USGS location is the official location using first arrivals and the additional industrial data; the Lamont location used the entire waveform of the longer-period surface waves.

Method	Lat	Lon
Revised USGS	27.828 N	90.210 W
Initial USGS	27.597 N	90.163 W
Lamont	27.8 N	90.2 W

4.2 and $M_s = 5.3$. Note: the quoted epicenter is a revised location using industrial exploration data (an explanation of that revision occurs later in this paper). The Lamont-Doherty Earth Observatory also detected the event using surface waves with periods around 50 seconds (Ekström, 2006a; Nettles, 2007). The Lamont method located the earthquake at 27.8 N, 90.2 W.

The revised (official) USGS location, initial location, and Lamont location are listed in Table 6.1. Differences in methods are not trivial, as initial P-wave arrival detection algorithms are not designed to detect events with weak or null P-wave arrivals. If stations use an algorithm dependent on that detection, an event may go unnoticed. Application of the surface wave methods using periods from 40-150 seconds has led to the discovery of hundreds of previously unreported earthquakes around $M5.0$ (Ekström, 2006b). The M_s 4.6 10 April, 2006 event, for example, was obtained via the surface wave method, but it was not recognized via algorithms designed to detect initial P-wave arrivals and is therefore absent from the USGS catalog. Given the unusual characteristics of these earthquakes (as explained below), it is possible that seismicity in the GoM is greater than previously thought: the known prevalence is partially a function of detection algorithms of receivers on land. Placing seismic receivers offshore, possibly taking advantage of existing infrastructure, may be one solution to this problem.

Vibrations from the Green Canyon earthquake were felt by personnel onboard a nearby tension leg platform roughly 15 km from the initial USGS location (Rijken and Leverette, 2007). Tension leg platforms are floating platforms with a system of mechanically anchored steel tendons coupling the platform to pilings driven into the seafloor. This platform had six tendons; each were monitored with

a tensiometer, and the platform also possessed accelerometers. During the earthquake, the onboard monitoring system recorded platform accelerations primarily in the vertical direction that were uncharacteristic of wave, tidal, and natural periods, along with an in-phase step-increase in tension on all six tendons. The six tendons are in phase for sixty seconds following the onset of the event, indicating that the quake excited the platform in heave, an observation consistent with the accelerometers. The maximum accelerations were $0.005g$ and the running mean of the increased tension over all tendons indicated 2 cm (0.8 inches) of seafloor subsidence. This displacement was permanent and was only able to be deduced due to an uncharacteristically calm sea. While the clock of the tensiometer was not accurate enough to treat as a seismometer, the observed displacement places a relevant constraint on possible seismic sources, even though the subsidence is minor.

The characteristics of the seismic waveforms differ from other earthquakes of similar size around the world. The waveforms are deficient in high-frequency energy relative to low-frequency energy, which is reflected in an unexpectedly low m_b magnitude (a measure of high-frequency energy) of 4.2 with respect to a M_s value (a measure of low-frequency energy) of 5.3 (Dewey and Dellinger, 2008). This discrepancy is inconsistent with earthquakes that occur in highly competent rock. From relationships between m_b and M_s values from around the world, we would expect a M_s 5.3 earthquake to produce a $m_b \geq 5.4$ (Stevens and Day, 1985). These discrepancies are displayed in Figure 6.4, which shows a record of the Green Canyon event alongside an earthquake of similar size and distance from the station, but with a source in highly competent rock.

Arrival time data did not allow a reliable depth computation but there are reasons to constrain it to less than 5 km. The epicentral distance of receivers should have identified reflections of seismic phases off the Earth's surface, but the observed waveforms were too complex to identify those phases. This suggests a source in the sedimentary section (< 15 km) as opposed to the crustal basement. The unexpectedly low high-frequency energy content and low m_b value also suggest a sedimentary source, as inefficient generation of high-frequency energy is expected

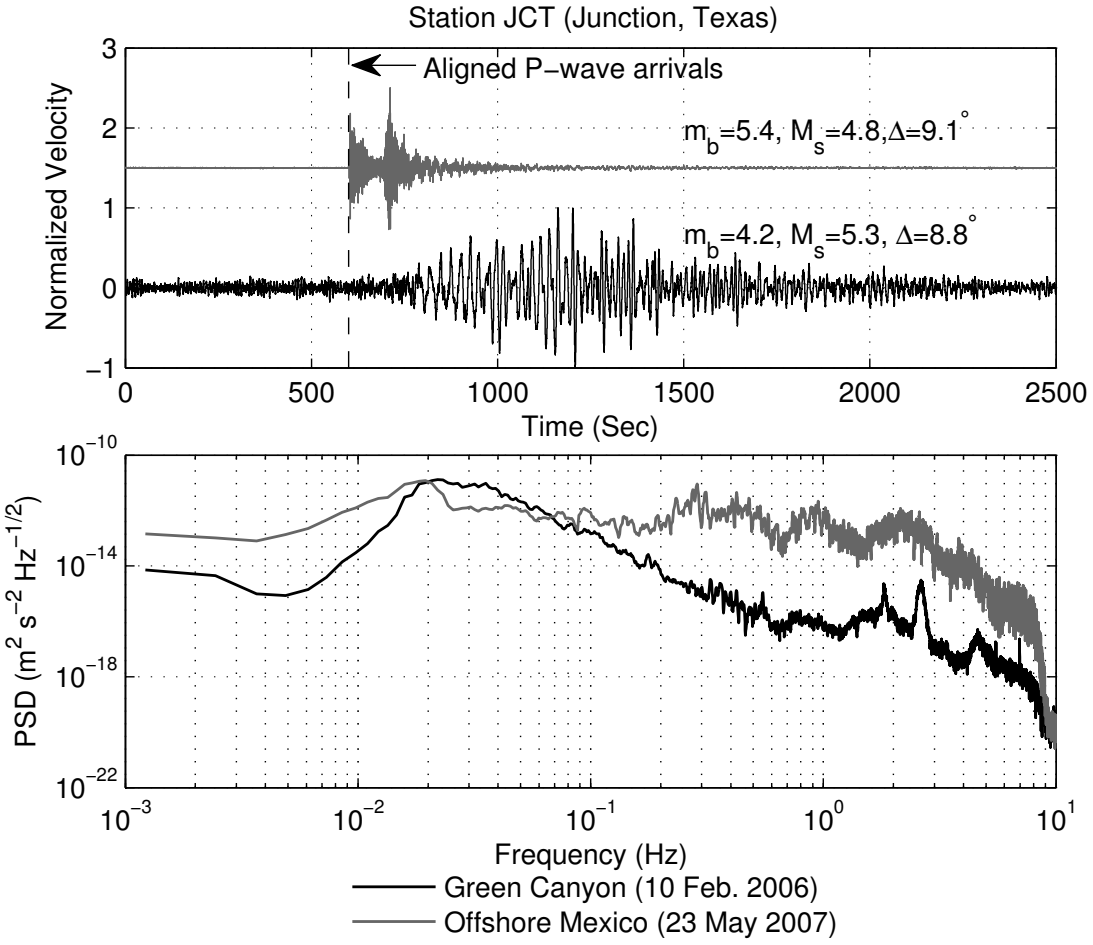

Figure 6.4: (a) Seismograms comparing an earthquake offshore Mexico possessing a similar magnitude and epicentral distance to the Green Canyon event. Velocities are normalized with respect to the maximum value. (b) The Green canyon event is relatively depleted in high-frequency energy compared to the "typical" offshore Mexico event and possesses an unexpected m_b compared to M_s from scaling relationships.

for faulting of weak sedimentary rock at shallow depths (Kovach, 1974; Ottemöller et al., 2005). Richter (1958) noted that deficient high-frequency energy content with respect to significant long-period energy would be characteristic of a sliding mass or landslide source. This so called single-force mechanism, as opposed to a double couple, has been successfully applied to massive landslides associated with long period seismic waves comparable in amplitude to major earthquakes (Kanamori and Given, 1982; Kanamori et al., 1984; Eissler and Kanamori, 1987; Hasegawa and Kanamori, 1987; Kawakatsu, 1989).

Trying to establish a focal mechanism for the Green Canyon event proved difficult. Nettles (2007) attempted to model the observed waveforms using standard centroid-moment-tensor (CMT) methods (Dziewonski et al., 1981; Ekström et al., 2005), but these standard attempts were problematic. In contrast, the observed waveforms were well fit using the centroid-single-force (landslide) inversion method of Kawakatsu (1989). The landslide inversion produced the following parameters: sliding at an azimuth of 244° east-of-north on a slope of 4°, with a Mass $\times$ Distance parameter $M_D = 0.6 \times 10^{14}$ kg m. M_D is analogous to a scalar seismic moment; its attributes cannot be separated. For example, a 20 m thick section of sediment sliding 1 m is equivalent to a 1 m thick section of sediment being displaced 20 m.

A moment-tensor solution did exist, but only by placing the earthquake centroid within a few km of the surface and applying an uncharacteristically low shear modulus (see, e.g., Selby et al. 2006). Nettles (2007) was able to fit a double-couple source with a scalar seismic moment $M_0 = 1.4 \times 10^{17}$ N m, using a shear wave velocity of $V_s = 2.6$ km/s. The solution was either a horizontal dip-slip source at an azimuth of 230° east-of-north; or a vertical dip-slip source along a vertical plane with a strike of 320°. The area of the slip plane and slip distance cannot be independently evaluated from the surface waves, but to produce that moment, earthquake scaling relationships would suggest an average displacement of 1m over a fault with an area of 1 km^2. Those scaling relationships, however, are applicable to highly competent rock, and may not be viable for the weak sedimentary section. The slip parameters of these various sources are summarized in Table 6.2.

Table 6.2: List of possible earthquake sources and slip parameters from the Lamont full-waveform surface wave inversion (Nettles 2007).

Source	Moment	Azimuth (° N of E)	Dip (°)	Rake (°)
Landslide	0.6×10^{14} kg m	244	4	N/A
Horizontal slip	1.4×10^{17} N m	230	0	0
Vertical slip	1.4×10^{17} N m	320	90	90

Table 6.3: Significant earthquakes in the GoM and whether they had clear, demonstrable focal mechanisms and were identified by the USGS using P-wave detection algorithms.

Date	M	Lat	Lon	Focal Mechanism	USGS Catalog
24 Jul 1978	5	26.79 N	89.17 W	Yes	Yes
10 Feb 2006	5.3	27.528 N	90.210 W	No	Yes
18 Apr 2006	4.6	28.8 N	88.3	No	No
10 Sep 2006	5.8	26.62 N	86.84 W	Yes	Yes

A paramount point is that while standard CMT methods struggle to fit solutions to the Green Canyon event (and similarly, the M_s4.6 18 April, 2006 earthquake), the CMT methods do produce good solutions for the focal mechanisms and magnitudes of both the M5.0 24 July, 1978 and M_w5.8 10 September, 2006 earthquakes (Table 6.3). This discordance further suggests an unusual source for the Green Canyon event.

6.5 Revising the epicenter using industrial data

The original USGS location for the Green Canyon earthquake – obtained from initial P wave arrivals at stations north of the event along the United States Gulf Coast – differed greatly from the Lamont surface wave method. To reconcile these differences, we used recordings from industrial seismic surveys to the southeast and southwest of the suspected epicenters.

We first obtained recordings from the Atlantis ocean-bottom-node survey, a large experiment involving a total of 900 four-component ocean-bottom nodes rolling through 1628 receiver locations over two patches, with nodes spaced every

426 m, spanning a surface of 247 km^2. This experiment was designed to image beneath complex salt overburdens. The nodes possessed a natural frequency of 10 Hz (Beaudoin and Ross, 2007). At the time of the earthquake, the Green Canyon event was detected on over 500 active nodes operating over a 10 km by 6 km array. We obtained 2.5 hours of data spanning the period around the earthquake and analyzed it for both natural and anthropogenic signals such as ongoing seismic airgun sources that could contaminate the data. Although there are a large number of signals in the data, they can be identified by their distinct arrival times, frequencies, and apparent phase velocities across the array. Dellinger and Ehlers (2007) show that at frequencies above 5 Hz, repetitive airgun shots from oil industry seismic exploration surveys dominate the data. Below 1 Hz, a nearly continuous background noise rumbles from the south and east with an apparent phase velocity across the array of 2000 m/s. At 2 Hz and below, the earthquake signal dominates the data from 04:14:34 UTM to about 04:20. It begins with several discrete bursts arriving from the NNW over a span of 20 seconds, followed by a drawn out coda from the NNW lasting over 8 minutes. Other distinct events from different azimuths arrive following the main event: one from the SSE at 04:22:13 with a drawn out coda over 3 minutes; and a weak, diffuse event from the ESE at 04:27 that also fades in and out over a 3 minute interval. The source of these secondary events from different azimuths remains unknown, though they may be distant reflections.

To improve the data quality, we separated the nodes into seven distinct patches, taking care to avoid the most geologically complex areas such as the Sigsbee escarpment (Figure 6.5a). We beam-formed stacked all the nodes within each patch by identifying the phase velocity of the first-arrival and then stacked at that velocity over each patch, thereby creating signals from seven synthetic stations to the southeast of the event. The first arrivals of these stacked signals are shown in Figure. 6.5b.

We applied a similar process to industrial streamer recordings located southwest of the Green Canyon event, from the CGG Green Canyon Phase VIII multiclient survey (Courtesy CGGVeritas, Houston, Texas). The rumbling of the earthquake was apparent in each individual streamer (Fig.6.6). First arrivals were

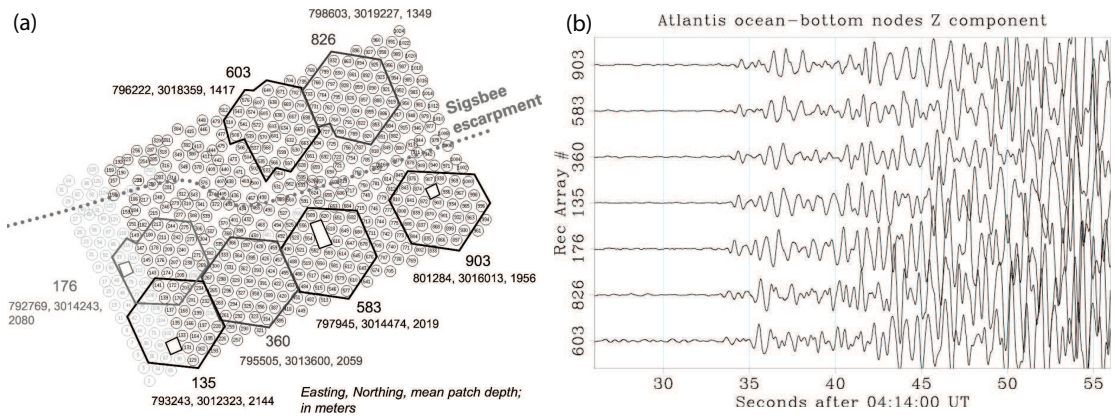

Figure 6.5: (a) Reproduced from Dellinger et al. (2007): more than 500 4-C nodes were in operation during the Green Canyon event as part of the Atlantis ocean-bottom-node survey. We created seven patches, chosen to avoid the Sigsbee escarpment and other complex geology. We included as part of each patch, all good receivers within 1400 m horizontally and 100 m vertically of the chosen central node. Records from all nodes within each patch were stacked to create seven apparent seismic stations. (b) Reproduced from Dellinger et al. (2009) Figure 2a: Green-Canyon earthquake first arrivals observed on the vertical component of stacked node patches. The data has been low-pass filtered to 2 Hz, which removed most of the airgun source from the observed signal.

less clear. To obtain a convincing first arrival, we stacked with an appropriate phase velocity over the entire streamer array and treated the results as a single seismic station located southwest of the epicenter.

The seismic records from these apparent stations were then provided to the USGS to improve their data coverage. Using first arrival times, the Green Canyon event was relocated to 27.828 N, 90.210 W (Dewey and Dellinger, 2008). The revised epicentral location was essentially coincident with the Lamont location (27.8 N, 90.2 W), which was calculated using a full-waveform surface-wave inversion instead of first P-wave arrivals. The Lamont location did not have the benefit of using the additional synthetic stations derived from industrial data (the frequency limitations of the industrial receivers would also prohibit that analysis,) but the locations agree to within the grid spacing of their model (a tenth of a degree, or six minutes.) This gave us confidence that the other parameters in the surface-wave waveform inversion – such as the landslide parameters or slip distributions in weak media – were correct.

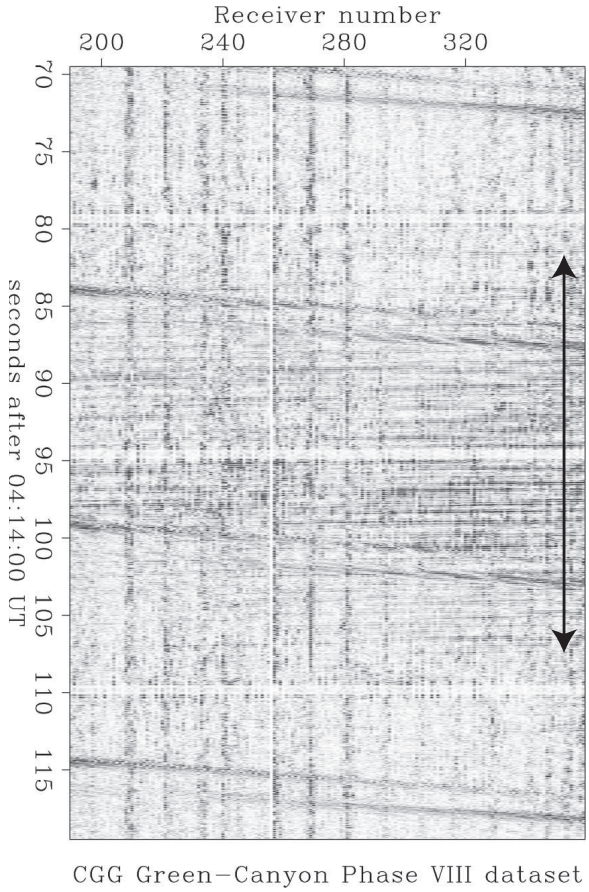

Figure 6.6: Modified from Dellinger et al. (2009) Figure 3: Part of one streamer line from the CGG Green-Canyon Phase VIII multi-client survey, covering all or part of four shots. There are three short no-data gaps between consecutive shots. The data have been bandpass filtered from 1.5 to 6 Hz and is shown unstacked. The airgun shots slope down to the right. The burst of noise sloping in the opposite direction around the middle of the plot is the loudest part of the Green Canyon earthquake (denoted by the black arrow). The much weaker first arrival is not directly visible in the unstacked data, but was detectable by stacking the entire streamer array to one trace. (Courtesy CGGVeritas, Houston, Texas.)

We applied additional constraints to the epicenter from the results of our apparent stations. Although the first arrivals impinged on the arrays nearly vertically, later arrivals came from a range of azimuths. Assuming a P-wave velocity of 1500 m/s, we were able to constrain the back azimuths of these arrivals. We did this for both the apparent Atlantis receiver arrays and the CGGVeritas streamer signal. The intersection of these back azimuths (see Figure. 6.2) provides an independent location of the event, indicating that the western portion of the revised USGS error ellipse was the most likely location for the earthquake. That portion of the epicentral area contains complex geology and sharp relief that coincides with the azimuths determined by the Lamont landslide model.

6.6 Slope stability and dislocation modeling

For the landslide source to be viable, it must be consistent with the geology near the epicenter. A detailed map showing high-resolution bathymetry and the revised USGS and Lamont locations is shown in Figure 6.7. This bathymetry is pre-earthquake (1999), obtained from a prestack water-velocity time-migration of the CGG Green Canyon Phase II dataset (Courtesy CGGVeritas, Houston, Texas). The revised USGS location and the Lamont full-waveform surface-wave inversion location are in a region with complex geologic relief. The azimuth of the slopes in this region is generally in the same orientation as the hypothetical landslide source (the arrow in Figure 6.7 and all subsequent figures indicates only the predicted azimuth of the landslide. The length of the arrow in these figures has no physical meaning such as distance, nor does it suggest an uphill slide since the model is only precise to a tenth of a degree, or six minutes.) For the landslide model to be plausible, slopes must not only be able to support large failures, but those failures must be of sufficient dimension to produce a M_s 5.3 event. We address these issues by utilizing slope stability and elastic half-space modeling.

6.6.1 Mudflow modeling

Slope angle, source volume, and sediment shear strength are all parameters that will govern the extent of a submarine landslide. The landslide model of Nettles (2007) produced a Mass × Distance parameter, which can be thought of as the scalar equivalent to seismic moment, of 0.6×10^{14} kg m. The slopes near the epicentral area of the Green Canyon event will only be able to sustain landslides of a certain size. Using mudflow modeling, we seek to determine if that size is consistent with the Mass × Distance number from the landslide model.

We use the BING 1D numerical model for muddy, subaqueous debris flows (Imran et al., 2001a,b) to determine the extent of hypothetical landslides on the suggested slopes. The BING model treats sediments as a viscoplastic fluid and solves the layer-integrated conservation equations of mass and momentum to model the downslope spreading of a subaqueous debris flow on a given bathymetric profile. The model is capable of supporting several rheologies corresponding to different viscoplastic fluid types and assumes an initial parabolic mass which then collapses and spreads along the slope.

We must assume a density ρ and a volume V, along with a runout distance R (which we calculate from the BING model). The Mass × Distance number is defined as $M_D = \rho V R$. BING assumes an initial parabolic mass, so we must invoke the volume under a parabola, $V = (2/3)LWH$, such that L is the initial length of material allowed to fail (required as an input into BING, i.e. 1000 m), H the maximum thickness of the initial mass (also required as an input into BING, i.e. 10 m), and W is the width of the initial mass (what we desire to constrain). Combining these equations and solving for W, we have

$$W = \frac{3M_D}{2\rho LHR}.$$

Two prominent slopes stand out in Figure 6.7: the one immediately south and to the west of the Lamont landslide location (and possessing nearly the same azimuth), and the slope to the northwest of that hillside. Our recipe is to run BING for different profiles along these possible hillsides for different initial masses (length and thickness) and to calculate their predicted runout distances R. We can then

calculate W. If W is much larger than the actual width of those escarpments, then that means a much larger mass than is physically possible is required to produce the suggested value for M_D. If W is within the physical limits of these slopes, it means that the slope is capable of producing a landslide consistent with M_D.

Using a density $\rho = 1800$ kg/m^3 and regional sediment properties (VanShaar et al., 2002), we computed runout distances for sediment thickness of 2.5, 5, 7.5, 10, 15, and 20 m, and initial lengths of 250, 500, 750, and 1000 m. Due to differences in sediment shear strength at depth, the maximum runout distance occurred for a thickness of 10 m and an initial length of 1000 m. This maximum runout distance for a hypothetical failure along the southwestern scarp was around 2375 m (1375 m plus 1000 m initial length). The width of this mass required to achieve the known value for M_D would be around 4.1 km, which is physically permissible by this slope. For comparison, a 5 m thick volume with an initial length of 1000 m would require an 11 km wide slope, and a 10 m thick volume with an initial length of 500 m would require a 14.3 km wide slope: neither of which fit the permissible geological dimensions. To produce the required M_D, any failure on that slope must approach 1000 m initial length and 10 m initial thickness – which is physically possible – but would also be observable in a post-earthquake, high-resolution bathymetry survey.

The more northern slope, in contrast, has too low of a gradient to support the runout distances required to generate M_D. For our soil model, the width of that slope would need to be on the order of 20 km, more than four times the actual physical dimensions. If a large landslide were to occur on that escarpment, that mudflow models suggests that it would not be large enough to produce the necessary value for M_D.

6.6.2 Elastic Dislocation Modeling

Recall that the Green Canyon event produced roughly 0.8 inches of subsidence at the tension leg platform (Rijken and Leverette, 2007). This subsidence is minor, and one caveat is that the subsidence at the platform is difficult to interpret because we are not completely sure what the effects of the platform's pilings

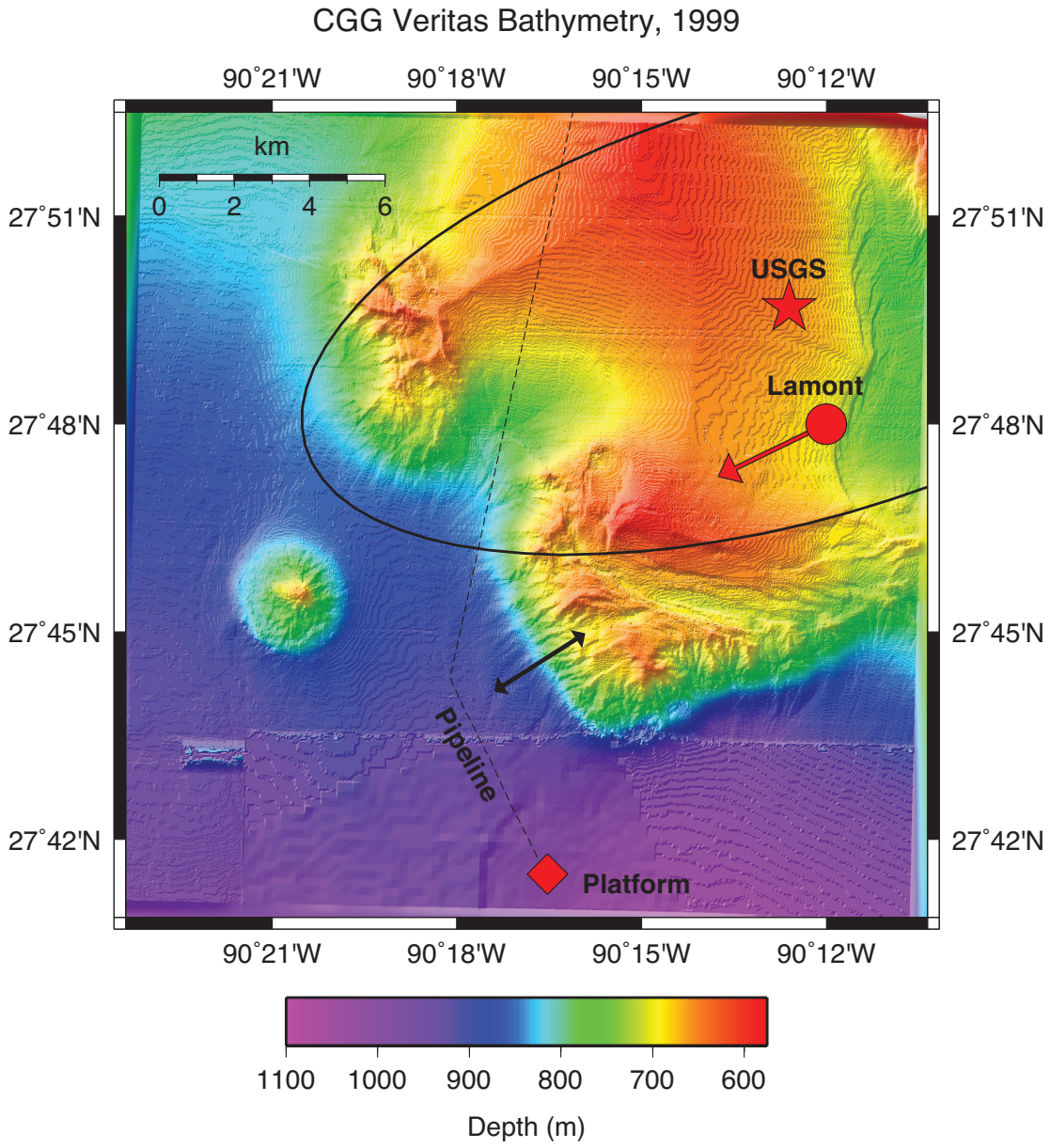

Figure 6.7: Close-up of the suspected epicentral area including the revised USGS location along with the landslide location azimuth (red arrow; the length of this arrow in this figure and all subsequent figures is meaningless, it only indicates the direction of the modeled sliding.) Bathymetry data is from before the earthquake (1999), Courtesy CGGVeritas. A platform and pipeline are within the plotted area. The black arrow shows the predicted landslide runout distance using the BING mudflow model.

being shaken would be – though it has been suggested that due to the nature of the design, liquefaction, for example, would create the opposite sign, making the ocean appear to get shallower, not deeper. For the purposes of this section, we assume the subsidence is accurate and we test whether our hypothetical sources – a landslide or a horizontal or vertical dip slip in an elastic medium – could produce roughly 0.8 inches of vertical seafloor displacement at the necessary distance and azimuth.

We model the landslide source as the removal of a load and an addition of the same load at a distance corresponding to the modeled runout distance atop an elastic half-space. We correct for the addition or removal of sea water that occupied or evacuated the thickness of the translated load. The problem of surface loading of an elastic half-space can be traced back to Boussinesq (1885), who demonstrated that the displacement and stress field in response to surface loading can be expressed in spatial derivative potential functions. Love (1929) attempted to solve this problem for uniform pressure applied to a rectangular load at the surface. As a result, this problem is typically referred to as Love's problem, though he only provided a solution for the stress field within an elastic half-space, not the displacement. Expanding upon that work, Becker and Bevis (2004) formulated explicit expressions for displacements in a non-gravitating, homogeneous, semi infinite half-space generated by uniform surface pressure applied over a rectangular region. Since the problem is linear, the solutions for any number of rectangular loads can be summed together to produce the solution for an arbitrary surface load.

We assumed a removed rectangular load of thickness 20 m, length 1000 m, and width 5000 m, and an applied load of the same dimensions located 3000 m along the length axis. These dimensions are slightly greater than the maximum dimensions supported by the mudflow modeling, so any deformation from this model should be an upper limit. We used a bulk modulus $\kappa = 33.65$ GPa and a shear modulus $\mu = 13.23$ GPa, along with a sediment density of 1781 kg/m^3 (or an apparent density of 0.78 since the problem is linear and requires us to add or subtract the influence of the increase or decrease in seawater) (Gangopadhyay and

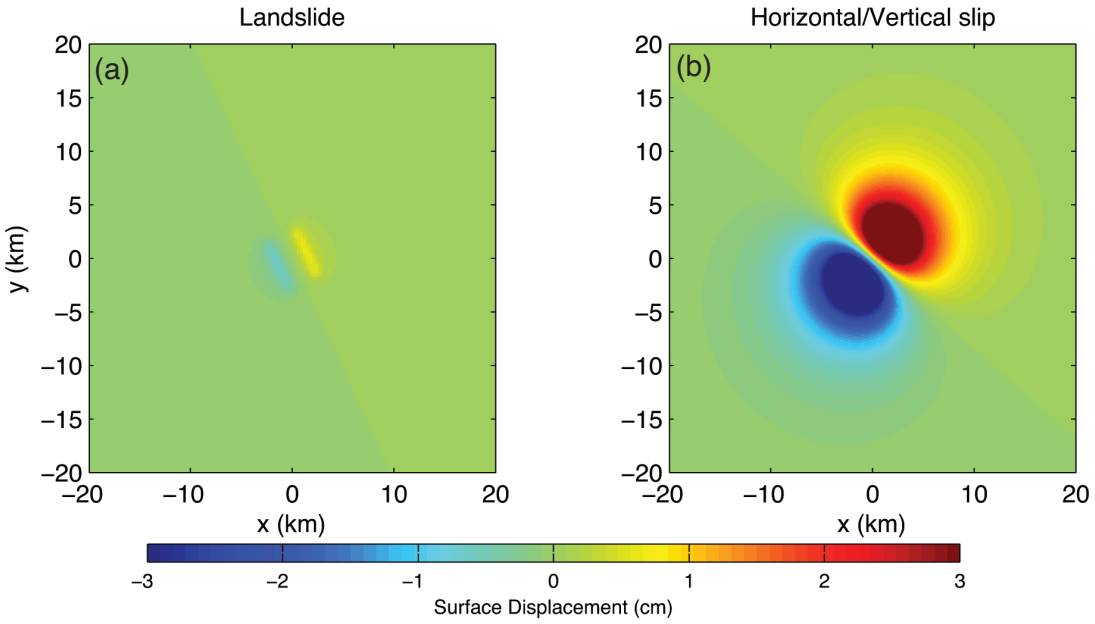

Figure 6.8: Surface deformation for different source models. (a) Landslide source modeled as the superposition of an evacuated rectangular mass and a deposited rectangular mass atop an elastic halfspace (Becker and Bevis, 2004). (b) Horizontal/vertical slip solution.

Sen, 2008). The vertical deformation for a landslide source is in Figure. 6.8a. For reference, the location of the tension leg platform would be to the southwest of the origin. We deliberately leave off plotting that location with respect to the origin given the actual uncertainty in the epicenter's location.

For the sub-horizontal and vertical slip models, we compute surface displacements using the formulation of Okada (1985, 1992), which is encoded into the EDGRN/EDCMP software package (Wang et al., 2003). We assume a point source dislocation and a Lame parameter of $\lambda = 24.83$ GPa and a shear modulus of 13.23 GPa, and the strike and dip orientations from the Lamont inversion (Table 6.2). The resulting vertical surface deformation for these sources is in Fig. 6.8b. Towards the platform, we observe 1 to 3 cm subsidence.

The observed subsidence at the tension leg platform was 0.8 inches, or ≈ 2 cm. Only the horizontal or vertical slip source is capable of producing that coseismic displacement within the uncertainty epicenter with respect to the platform. From the standpoint of a hypothetical applied pressure load, the landslide source is

insufficient to fully explain the observed ground deformation. While the observed deformation is unlikely to be solely the result of elastic dislocation theory (the weak upper sediments may not behave elastically), this is a possible constraint.

6.7 Geophysical Survey

While it cannot fully explain the observed subsidence, geotechnical modeling suggested that a landslide consistent with the volume and sliding distance from Nettles (2007) surface-wave inversion could occur on the escarpments near the epicenter. To confirm or reject the landslide hypothesis, we conducted a geophysical survey of the region.

This survey was performed in October 2008. The Scripps Institution of Oceanography vessel R/V Roger Revelle was in the GoM for a controlled source marine electromagnetic experiment imaging gas hydrates (see `http://marineemlab.ucsd.edu/`). The Green Canyon earthquake epicenter was located near the transit between two sites, and we arranged for a geophysical survey of the area including multibeam bathymetry, sidescan sonar, and sub-bottom profiling. The results from BING mudslide modeling suggested that if a landslide occurred along the slopes in the western epicentral area, it would have dimensions on the order of a couple kilometers in length (evacuation and deposition), up to 5 km in width, and several meters in thickness at the head scar or deposit. A feature of this size would be within the resolution limits of our multibeam echosounder.

The R/V Roger Revelle was equipped with a Kongsberg Simrad EM120 multibeam echosounder. The 12 kHz system has up to 191 beams capable of covering a 150 degree swath of the seafloor, mapping a width up to 6-7 times the water depth. The beam footprint is $1^\circ \times 1^\circ$ and the instrument is operable in depths from 50 to 11000 m. For sub-bottom profiling, we used the Knudsen 320 B 3.5 kHz profiler. Survey design was conflicting, as sub-bottom imaging is ideally performed across or along a slope, whereas multibeam will best resolve regions of sharp relief with the ship traveling at an oblique angle. We therefore surveyed two lines along the southwestern slope – to provide the best sub-bottom images –

and the remainder of the lines were E-W, which was roughly at a 30 degree angle with respect to the features we wished to image in the multibeam. Bathymetry and backscatter data were processed using the software MB-System (Caress and Chayes, 1995; MB-System, 2010)] and sub-bottom data using SIOSEIS (Henkart, 2010).

6.7.1 Bathymetry

The results of the multibeam mapping are in Figure 6.9b. The pre-earthquake high-resolution bathymetry in Figure 6.7a was obtained from prestack time-migration of a 3D seismic data set acquired in 1999, the CGGVeritas Green-Canyon Phase II multi-client survey (Courtesy CGGVeritas, Houston, Texas). Visual comparison between the pre (1999) and post (2008) bathymetry shows no large scale, significant differences (Figures 6.9 & 6.12).

We also difference the resulting grids to examine systematic spatial variations between the two surveys. Pre-earthquake bathymetry was converted from time to depth assuming a constant sea water velocity of 1500 m/s. We estimate, however, that the depth of the seismic source of that survey was around 8 m and the receiver depth at 9 m, so we would expect roughly a 17 m offset between the two surveys. To correct for this offset and possible differences in sound speed, we perform a least-squares fit on the two data sets to correct the pre-earthquake bathymetry so that its mean value is the same as the post-earthquake multibeam survey. We estimate a slope of 0.99435 and an intercept of 16.92 m. The 0.994 multiplicative factor means there is a little more than a half percent difference in the water velocity.

After correcting the pre-earthquake survey with these factors, we subtract it from the post-earthquake multibeam survey. Figure 6.10 shows the results of this differencing. There are significant errors and artifacts in the difference map, particularly directly below the ship, but we believe no large scale excavation or deposition is evident adjacent to the suspected slopes, at least not of the size required to account for the Mass $\times$ Distance parameter from the centroid-single-force inversion. Similar difference maps with respect to slope and azimuth also

reveal no significant differences over the area we believe would be required from the hypothetical landslide inversion.

There are technical reasons to explain some of the differences. 3D seismic and multibeam are different technologies, and the differences in technology may be responsible for differences in data. Multibeam sonar captures normal and angular incident reflections and scattering of narrow-band, rectified high-frequency sound (12 kHz), whereas 3D seismic captures near-normal incident reflection of broad-band, non-rectified sound at low frequencies (3-125 Hz[1]) (see, e.g., Mosher et al., 2006). The 3D seismic bathymetry has a higher data data density over most of the survey area (except for the south), and therefore better smoothing and rendering, and this may lead to minor differences. Ship roll artifacts also are also uncertain. A roll bias correction involves sailing along the same or partially overlapping track, but in different directions, and correcting for the difference in bathymetry as a bias in roll to the port or starboard side. This correction is ideally made over identical tracks in an area of no or gently varying relief. Our tracks are only partially overlapping, and the significant relief along the escarpments make this correction difficult. We did apply a roll-bias correction, but the standard deviation amongst parallel tracks was almost as large as the signal.

6.7.2 Backscatter

We also analyzed sidescan sonar data (Figure 6.11.) A 3D perspective view in Figure 6.12 exhibits this information. Sidescan sonar (or backscatter) values are related to surface lithology, and contrasts may delineate not only different sediment types (mud versus rock outcrop), but also remolded versus intact sediments. While groundtruthing (video or sediment samples) is needed to statistically calibrate backscatter, raw data values can meaningfully distinguish physical and geological seabed. Using GLORIA sidescan, Schlee and Robb (1991) showed that submarine landslide debris deposits can be recognized by their generally brighter backscatter compared to seafloor covered by undisturbed, hemipelagic finer grained sediments.

[1]In practice, the frequencies typically range from 5-80 Hz (Personal Communication, Joe Dellinger, BP America, Inc.

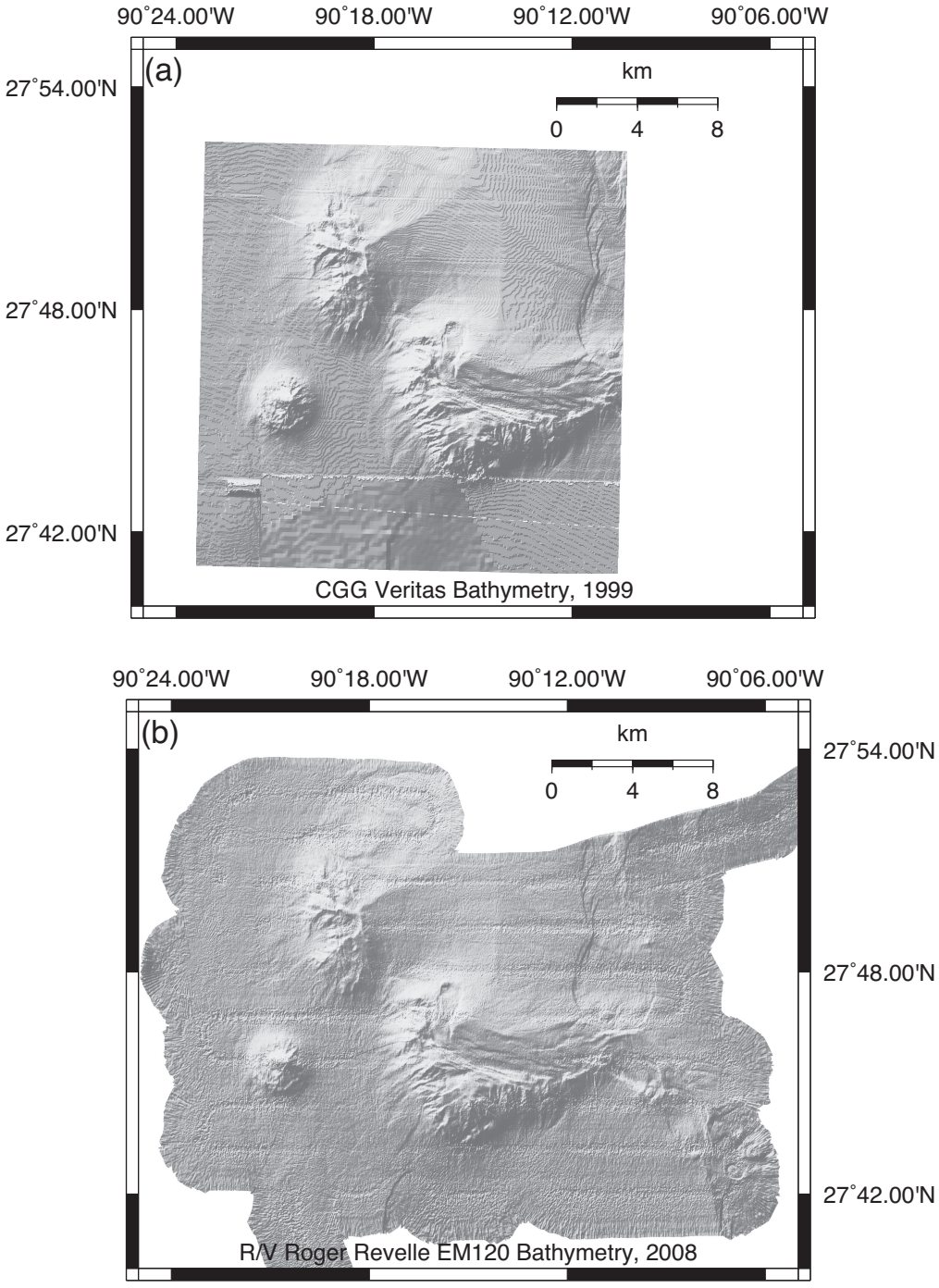

Figure 6.9: (a) CGGVeritas Green Canyon Phase II multiclient survey; bathymetry from pre-stack time migration (Courtesy CGGVeritas, Houston, Texas). (b) R/V Roger Revelle EM120 multibeam bathymetry.

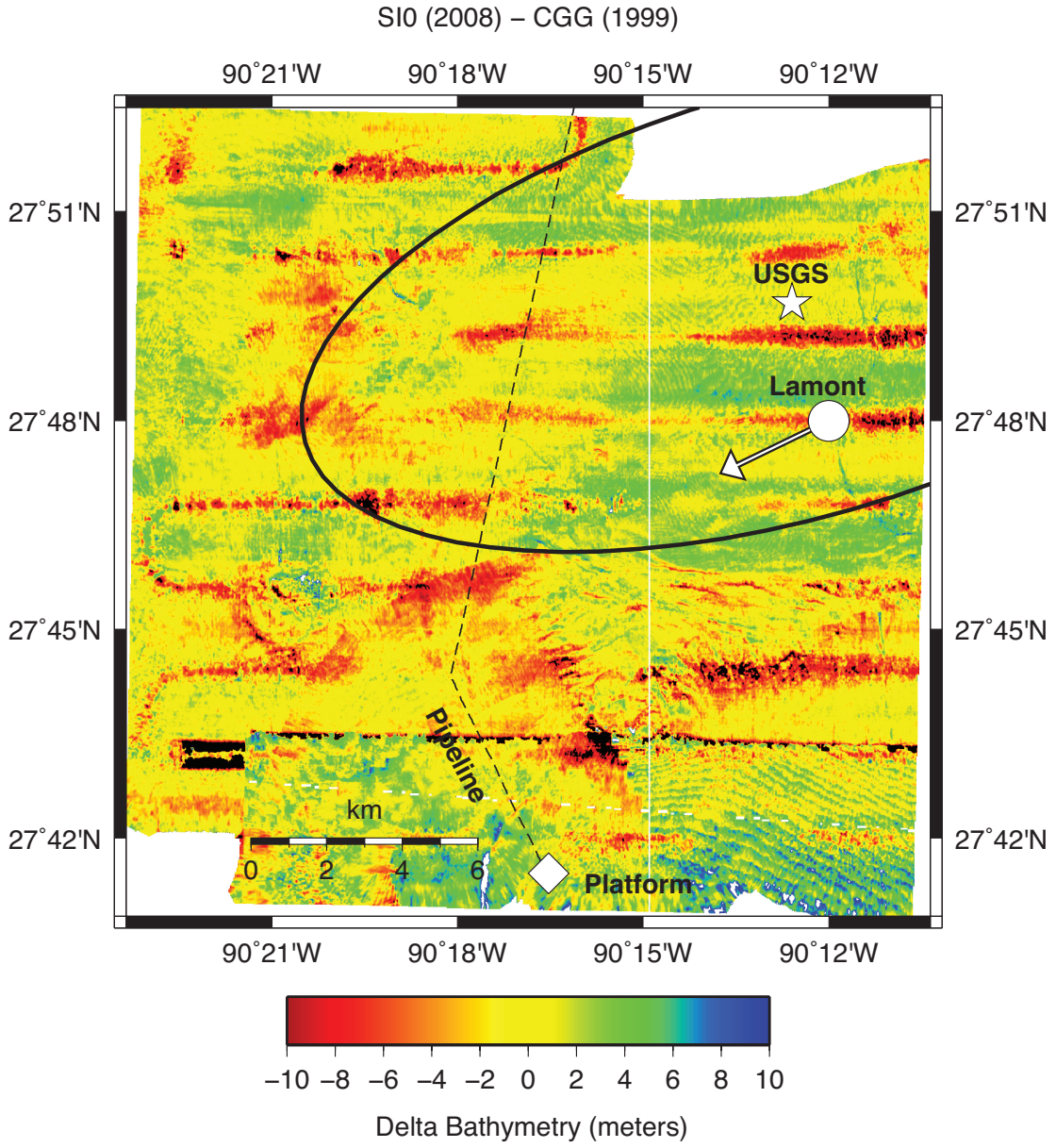

Figure 6.10: Change between the post-earthquake (2008 EM120) and pre-earthquake (1999 CGGVeritas) bathymetry. Negative values represent areas of excavation and positive values regions of deposition. Expected scale of a slide is roughly 2.5×4 km.

We reversed the backscatter values to better delineate features; darker backscatter indicates higher reflectivity and is likely to indicate mass-wasting.

The results in Figure 6.11 indicate no significant change in backscatter value along the predicted landslide azimuth on the steepest, southwestern slope which we felt was the most likely to support failure. There is a significant difference in texture to the south, which suggests debris, but such features are smaller than required for the Mass $\times$ Distance parameter and in the wrong orientation. The slope just north and to the west of the pipeline route exhibits some minor textural change from the crown of the slope to out along its base. The morphology of this feature in both pre-and-post earthquake bathymetry suggests it is a slope failure. The width of the material is not consistent with the value required for the landslide inversion unless it was an extremely deep seated mass wasting event (i.e. $>$ 20 m of material). This feature suggest a slope failure, but close examination (Figures 6.9 & 6.12) suggests it is present in both pre and post earthquake bathymetry and is therefore an older feature.

6.7.3 Sub-bottom

Sub-bottom profiling was acquired coincident with the multibeam. Results are shown in Figure 6.13. Profiles up the potential slopes of failure are along lines A-A' and G-G', respectively. No head scarp, zone of evacuation, or toe are evident. There does exist an uppermost, opaque layer at the base of those slopes (which pinches out, for example, along profile F-F'), but we traced that layer to all profiles, suggesting it is from sedimentation, not mass wasting. The eastern portion of the survey area exhibits normal faults with potentially several meters of offset just east of the epicenters, along with diapirs that interrupt the sedimentary layering and correspond to areas of high backscatter (most likely from cap rock atop of salt) in Figure 6.11. We conclude that there is no evidence of a large debris flow in the sub-bottom data, at least to within the instrument resolution ($\approx$ 1 m.)

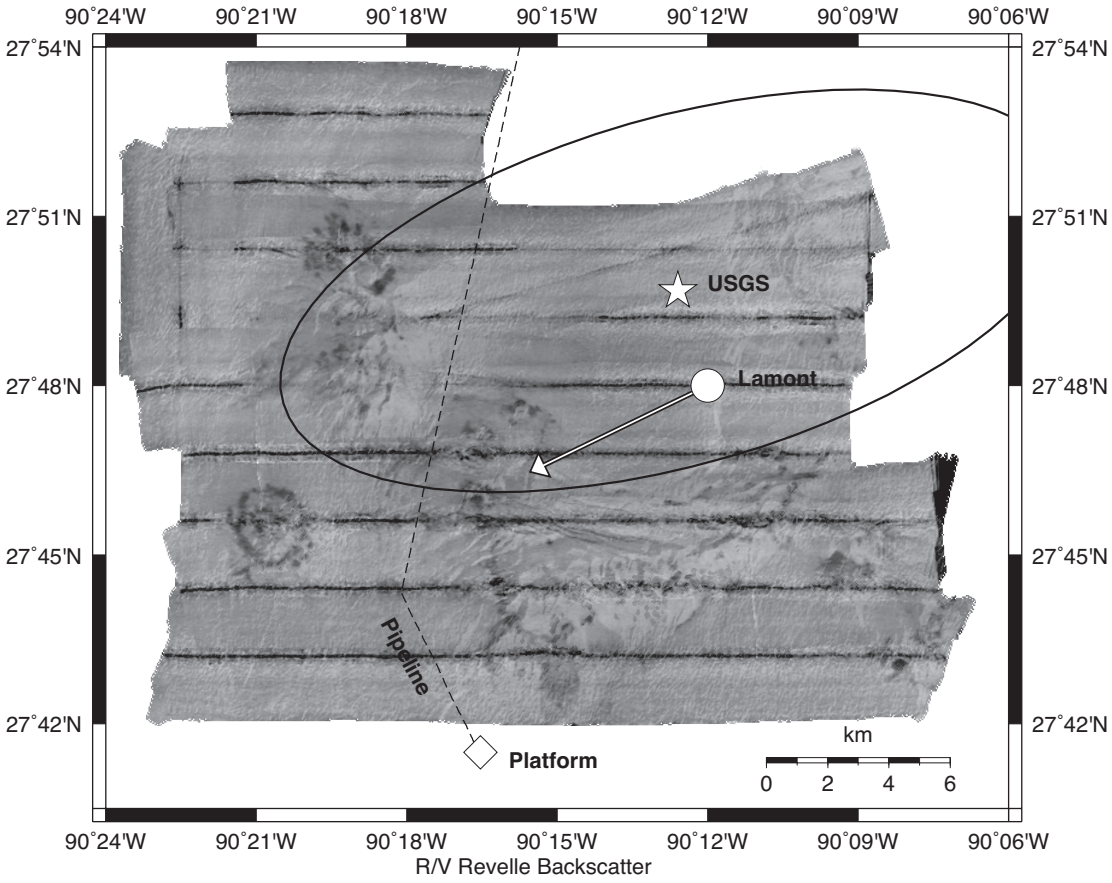

Figure 6.11: EM120 backscatter results draped over bathymetry. Darker shades indicate higher reflectivity.

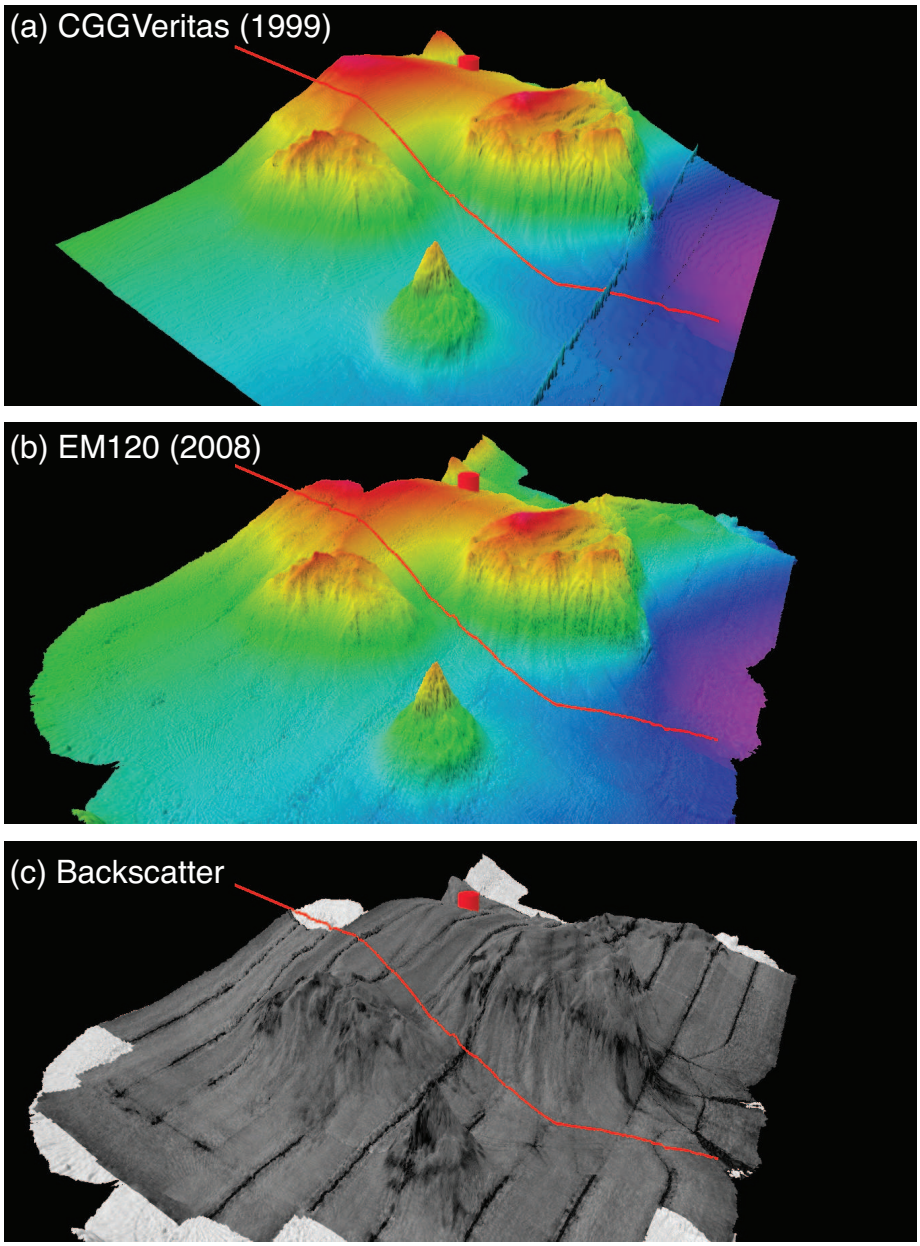

Figure 6.12: 3D perspective views of (a) pre-earthquake bathymetry (Courtesy CGGVeritas, Houston, Texas); (b) post-earthquake bathymetry; and (c) draped backscatter. Images possess a 12X vertical exaggeration. The red line denotes the pipeline and the red cylinder the USGS epicenter.

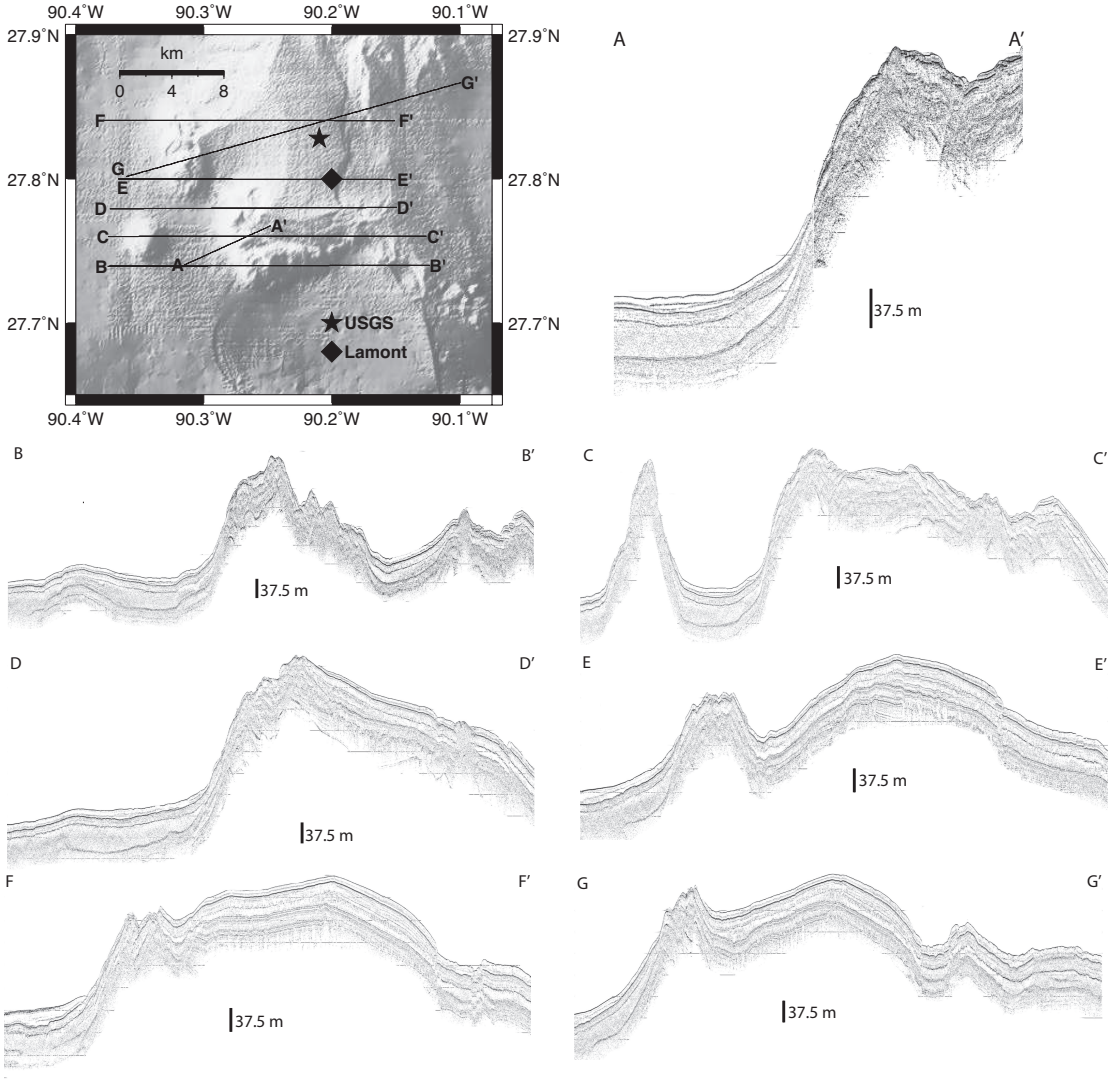

Figure 6.13: Sub-bottom profiles. Vertical lines in each profile are equivalent to height of 37.5 m.

6.8 Discussion

We cannot completely rule out the the existence of small amounts of displaced debris due to the differences between 3D seismic and multibeam echosounder bathymetry, but our results find no evidence for a large submarine landslide on the scale required to produce the M_s 5.3 signal (10 m thick and around 2.5×4 km in length and width.) We believe that any landslide capable of generating a M_s 5.3 earthquake should be spatially delineated in the multibeam, sub-bottom, and backscatter data. A thin veneer of failed sediment (< 1 m) or small patches of debris may very well exist, but the absence of a large scale feature suggests that the source mechanism for the Green Canyon earthquake was likely shallow faulting within the sedimentary cover.

The predominance of long-period, surface wave radiation is similar to other perplexing earthquakes, including a series of $\approx M$ 3 at the Wilmington Oil Field in California (Kovach, 1974) and a M_s 4.9 event at the Ekofisk field in the North Sea (Ottemöller et al., 2003, 2005; Selby et al., 2005). These earthquakes were attributed to subsidence from production withdrawal and water injection. At the Wilmington Field, subsidence produced large horizontal shear stresses that were subsequently released via horizontal movement along very shallow dipping planes. One key feature of these events was very low rupture velocities (0.1 to 0.3 km/sec). The M_s 4.9 event at the Ekofisk field also exhibited a similarly unusual m_b versus M_s relationship, with $m_b = 3.7$. Ottemöller et al. (2003) and Selby et al. (2005) both suggested a vertical dip slip source, but with a different polarity of slip, the difference due to the sensitivity of incorporating a thick surficial sediment layer with low seismic wave speeds. In a later study utilizing greater geophysical data, Ottemöller et al. (2005) revised their result and concluded a near-horizontal nodal plane was the most likely source.

Unlike those sources, there was no hydrocarbon production in the region of the earthquake. The common attribute among these events is the character of the waveforms and possible focal mechanisms. The sub-bottom data display near-vertical dip-slip offsets that breach the surface, just north of what appears to be cap-rock atop diapirs penetrating the surface (Figure 6.13). The depth

resolution and spatial density of this data are not adequate to fully map the fault and salt structures; analysis of 3D multi-channel seismic data is needed to map these features and to differentiate between a near-horizontal or near-vertical dip slip source. It is important to reiterate that salt tectonics dominate this region. Salt diapirs and withdrawal basins drive the morphology and we suggest that subsidence due to salt uplift or withdrawal and the associated generation of horizontal shear stresses should be considered as a possible factor in the observed seismicity.

Regional seismicity in the GoM is considered sparse; events in weak sediments are not well understood due to their scarcity and lack of adequate instrumentation. The USGS earthquake catalog does show several other events in the vicinity of the 10 February 2006 Green Canyon event, suggesting there may be some regional trend or mechanism. It is important to note, however, that those other events are arguably less well located than the initial USGS estimate of the Green Canyon event, which itself was significantly revised in location.

6.9 Conclusions

Earthquake relocation using ocean bottom industrial seismic data places the 10 February 2006 Green Canyon in a region consistent with surface wave estimates of the earthquake source. Comparing post-earthquake with pre-earthquake bathymetry, we observe no large regions of evacuation and deposition consistent with a model of a large landslide capable of generating seismic waves. The preferred earthquake solution is therefore likely to be sub-horizontal or vertical slip within the shallow sedimentary cover.

An interesting question is not just the mechanism and potential impacts of this event, but whether other unusual earthquakes of similar magnitude have occurred over the past three decades, but are not included in the USGS catalog as the result of their uncharacteristic seismic signatures not triggering initial P-wave arrival detection algorithms. As an example, we advocate the M_s 4.6 earthquake of 18 April, 2006 (Nettles, 2007). This event also has an unknown source mechanism and also produced anomalously weak P-wave arrivals and was not detected and

included in the USGS catalog. It was detected using long period surface waves.

Given the economic and environmental significance of this region, detecting, locating, and characterizing significant earthquakes is essential. The recent earthquakes suggest the need to revise our understanding and assumptions of earthquake frequency and magnitude in the Gulf of Mexico. These issues could potentially be resolved with the placement of several permanent, broadband seismometers or geophones located near the deepwater Gulf of Mexico.

6.10 Acknowledgments

The analysis and conclusions in this chapter represent the conclusions of the author and Scripps Institution of Oceanography, and no other entity. Nonetheless, we are indebted to Joe Dellinger at BP America, Inc. for his assistance in acquiring the industrial data used in this study. We also thank Meredith Nettles for providing the locations and source properties of various earthquakes. Thanks to CGGVeritas for permission to use the CGG Green Canyon Phase II and VIII multiclient seismic surveys (Courtesy CGGVeritas, Houston, Texas) for research purposes. Also thanks to BP and BHP Billiton for giving us permission to use and publish the Atlantis OBS data. We express additional gratitude to the Steve Constable and Karen Weitemeyer at SIO, along with the crew of the R/V Revelle, for accommodating our mission during their marine CSEM experiment. Hugh Banon, Herlinde Mannaerts-Drew, and Walter Guidroz at BP also contributed to making industrial data available for this analysis; Tony Heyn and Rich Weiland at BP provided the initial source mechanism illustration in Figure 6.3; and Nick Burke helped us obtain the BP-picked bathymetry from the CGG Green-Caynon Phase II data.

This chapter is being prepared for submission for publication. The article in preparation goes as: **Blum, J., 2010: The M_s 5.3 Green Canyon (northern Gulf of Mexico) earthquake of 10 February 2010: a landslide or fault source? In preparation for *Geophysics Journal International***. The author of this dissertation is responsible for writing the manuscript (and intended

publication.) Joe Dellinger at BP assisted in providing the relevant industrial data and processing the seismic signals to obtain P-wave arrival times. The author performed all geotechnical modeling and designed the geophysical survey, serving as chief scientist to acquire the data, and processed and interpreted the data products.

REFERENCES

Angell, M., and Hitchcock, C., 2007: A geohazard perspective of recent seismic activity in the northern Gulf of Mexico. In *Offshore Technology Conference*, 19035.

API, 2000a: *Recommended practice for planning, desiging, and constructing fixed offshore platforms - load and resistance factor design.* API-RP2A. American Petroleum Institute, Washington, D.C., 21 edition.

API, 2000b: *Recommended practice for planning, designing and constructing fixed offshore platforms - working stress design.* API-RP2A. American Petroleum Institute, Washington, D.C., 21 edition.

Beaudoin, G., and Ross, A., 2007: Field design and operation of a novel deepwater, wide-azimuth node seismic survey. *The Leading Edge*, 494–503.

Becker, J., and Bevis, M., 2004: Love's problem. *Geophysical Journal International*, **156**, 171–178.

Bird, D., Burke, K., Hall, S., and Casey, J., 2005: Gulf of Mexico tectonic history: hotspot tracks, crustal boundaries, and early salt distribution. *Am Assoc. Petrol. Geol. Bull.*, **89**, 311–328.

Boussinesq, J., 1885: *Application des potentiels à l'étude de l'égulibre et du mouvement des solides élastiques*, 508. Gauthier-Villars, Paris.

Brown, L., Bracci, J., Hueste, M., and Murff, J., 2003: Assessment of seismic risk for subsea production systems in the Gulf of Mexico. Technical Report 422, MMS/OTRC.

Caress, D., and Chayes, D., 1995: New software for processing sidescan data from sidescan-capable multibeam sonars. In *Proceedings of the IEEE Oceans 95 Conference*, 997–1000.

Dellinger, J., Blum, J., and Nettles, M., 2009: The 10 February 2006 "Green Canyon" earthquake: a case history of an unusual seismic event. *SEG Expanded Abstracts*, **28**(572), DOI:10.1190/1.3255822.

Dellinger, J., Dewey, J., Blum, J., and Nettles, M., 2007: Relocating and characterizing the 10 Feb 2006 "Green Canyon" Gulf of Mexico earthquake using oil-industry data. *EOS Trans. AGU*, **88**(52), S13F–01.

Dellinger, J., and Ehlers, J., 2007: Low frequencies with a "dense" OBS array: The Atlantis-Green Canyon earthquake data set. *SEG Technical Program Expanded Abstracts*, **26**(1), 36–40. doi:10.1190/1.2792377.

Dewey, J., and Dellinger, J., 2008: Location of the Green Canyon (offshore Southern Louisiana) seismic event of february 10, 2006. Open-File Report 1184, U.S. Geological Survey.

Dokka, R., 2006: Modern-day tectonic subsidence in coastal Lousiana. *Geology*, **34**, 281–284.

Dziewonski, A., Chou, T.-A., and Woodhouse, J., 1981: Determination of earthquake source parameters from waveform data for studies of global and regional seismicity. *Journal of Geophysical Research*, **86**, 2825–2852.

Eissler, H., and Kanamori, H., 1987: A single-force model for the 1975 Kalapana, Hawaii earthquake. *Journal of Geophysical Research*, **92**, 4827–4836.

Ekström, G., 2006a: Global detection and location of seismic sources using surface waves. *Bull. Seismol. Soc. Am.*, **96**, 1201–1212.

Ekström, G., 2006b: Gutenberg Lecture: the growing diversity of seismic sources. *EOS Trans. AGU*, **87**(52).

Ekström, G., Dziewonski, A., Maternovskaya, N., and Nettles, M., 2005: Global seismicity of 2003: centroid-moment tensor solutions for 1087 earthquakes. *Phys. Earth and Planet. Int.*, **148**, 327–351.

Frohlich, C., 1982: Seismicity in the central Gulf of Mexico. *Geology*, **10**, 103–106.

Gangopadhyay, A., and Sen, M., 2008: A possible mechanism for the spatial distribution of seismicity in northern Gulf of Mexico. *Geophysical Journal International*, **175**, 1141–1153.

Hasegawa, H., and Kanamori, H., 1987: Source mechanism of the magnitude 7.2 Grand Banks earthquake of November 1929: double couple or submarine landslide? *Bulletin of the Seismological Society of America*, **77**, 1984–2004.

Henkart, P., 2010: SIOSEIS, http://sioseis.ucsd.edu/.

Imran, J., Harff, P., and Parker, G., 2001a: A numerical model of submarine debris flow with graphical user interface. *Computers & Geosciences*, **27**, 717–729.

Imran, J., Parker, G., Locat, J., and Lee, H., 2001b: 1d numerical model of muddy subaqueous and subaerial debris flows. *Journal of Hydraulic Engineering*, **127**, 959–968.

Kanamori, H., and Given, J., 1982: Analysis of long-period seismic waves excited by the May 18, 1980, eruption of Mount St. Helens: a terrestrial monopole. *Journal of Geophysical Research*, **87**, 5422–5432.

Kanamori, H., Given, J., and Lay, T., 1984: Analysis of seismic body waves excited by the Mount St. Helens eruption of May 18, 1980. *Journal of Geophysical Research*, **89**, 1856–1866.

Kawakatsu, H., 1989: Centroid single force inversion of seismic waves generated by landslides. *Journal of Geophysical Research*, **94**, 12363–12374.

Kovach, R., 1974: Source mechanisms for Wilmington Oil Field, California, subsidence earthquakes. *Bulletin of the Seismological Society of America*, **64**, 699–711.

Love, A., 1929: The stress produced in a semi-infinite solid by pressure on part of the boundary. *Philosophical Transactions of the Royal Society A*, **667**, 377–420.

MB-System, 2010: http://www.mbari.org/data/mbsystem/.

Mosher, D., Bigg, S., and LaPierre, A., 2006: 3D seismic versus multibeam sonar seafloor surface renderings for geohazard assessment: case examples from the Scotian slope. *The Leading Edge*, 1484–1494.

Nettles, M., 2007: Analysis of the 10 February 2006: Gulf of Mexico earthquake from global and regional seismic data. In *Offshore Technology Conference*, 19099.

Nunn, J., 1985: State of stress in the northern Gulf Coast. *Geology*, **13**, 429–432.

Okada, Y., 1985: Surface deformation due to shear and tensile faults in a half space. *Bulletin of the Seismological Society of America*, **75**(4), 1135–1154.

Okada, Y., 1992: Internal deformation due to shear and tensile faults in a half-space. *Bull. Seismol. Soc. Am.*, **82**, 1018–1040.

Ottemöller, L., Nielsen, H., Atakan, K., Braunmiller, J., and Havskov, J., 2005: The 7 May 2001 induced seismic event in the Ekofisk oil field, North Sea. *Journal of Geophysical Research*, **110**.

Ottemöller, L., Nielsen, H., Atakan, K., Braunmiller, J., and Kavskov, J., 2003: Ekofisk seismic event of May 7, 2001. In *Proceedings of the 23rd IUGG General Assembly*. Int. Union of Geod. and Geophys., Sapporo, Japan.

Peel, F., 2007: The setting and possible mechanism of the 2006 Green Canyon seismic event. In *Offshore Technology Conference*, 19032.

Richter, C., 1958: *Elementary seismology*, 155–156. W.H. Freeman, San Francisco.

Rijken, O., and Leverette, S., 2007: Tension leg platform response to earthquake in Gulf of Mexico. In *Proceedings of the Seventeenth (2007) International Offshore and Polar Engineering Conference*. The International Society of Offshore and Polar Engineers.

Salvador, A., 1991: Origin and development of the Gulf of Mexico basin. In *The Gulf of Mexico Basin*, editor A. Salvador, The Geol. North Am., J, 389–444. Geological Society of America.

Sarwar, G., 2002: Northern Gulf of Mexico: a passive or active margin? In *Proceedings of the AAPG Annual Meeting*. American Association of Petroleum Geologists.

Schlee, J., and Robb, J., 1991: Submarine processes of the middle Atlantic continental rise based on GLORIA imagery. *Geological Society of America Bulletin*, **103**, 1090–1103.

Selby, N., Eshun, E., Patton, H., and Douglas, A., 2005: Unusual long-period Rayleigh wave radiation from a vertical dip-slip source: the 7 May 2001 North Sea earthquake. *Journal of Geophysical Research*, **110**.

Stevens, J., and Day, S., 1985: The physical basis of $m_b : m_s$ and variable magnitude methods for earthquake/ explosion discrimination. *Journal of Geophysical Research*, **90**, 3009–3020.

Talwani, P., and Rajendran, K., 1991: Some seismological and geometric features of intraplate earthqaukes. *Tectonophysics*, **186**, 19–41.

VanShaar, S., Gilbert, R., and Wright, S., 2002: Bp deep-water geotechnical data representation and analysis. Geotechnical Engineering Report GR02-1, Civil Engineering Department, The University of Texas at Austin.

Walsh, J., Corbett, R., Mallinson, D., Goni, M., Dail, M., Lowey, C., Marciniak, K., Ryan, K., Smith, C., Stevens, A., Sumners, B., and Tesi, T., 2006: Mississippi delta mudflow activity and 2005 Gulf of Mexico Hurricanes. *EOS Trans. AGU*, **85**, 477–478.

Wang, R., Martinez, F., and Roth, F., 2003: Computation of deformation induced by earthquakes in multi-layered elastic crust – FORTRAN programs EDGRN/EDCMP. *Computers & Geosciences*, **29**, 195–207.

Wells, D., and Coppersmith, K., 1994: New empirical relationships among magnitude, rupture length, rupture width, rupture area, and surface displacement. *Bull. Seismol. Soc. Am.*, **84**, 974–1002.